THE STRUCTURE AND GROWTH OF ErSi_{2-x} NANOWIRES ON SI(001)

Jeremy Mitchell

Thesis submitted for the degree of DOCTOR OF PHILOSOPHY

Department of Physics,
University of York

Sep 2012

Abstract

In this work the structure and interface structure of ErSi_{2-x} nanostructures grown on $\mathrm{Si}(001)$ are investigated by aberration corrected high angle annular dark field scanning transmission electron microscopy. The initial nucleation and growth mechanism are investigated by direct observation of the structure of ultra-small nanowires and it was found that the preferred structure does not fit with the currently accepted growth model. The nanowires nucleate in the hexagonal phase with an orientation relationship with the silicon substrate of $(001)_{Si}/(01\bar{1}0)_{ErSi_{2-x}}$, $[110]_{Si}/[0001]_{ErSi_{2-x}}$ which is the exact opposite of the currently accepted strained growth model. As the nanowires increase in size it was observed that the nanostructures transform their orientation relationships to reduce their strain resulting in the structure that is expected from the strained growth model. A new growth model is suggested in that the observed orientation relationship has been found by previous calculations to be lower in energy than the strained growth equivalent for ultra-small nanowires.

The interfaces of the ErSi_{2-x} nanostructures with $\mathrm{Si}(001)$ are found to be highly varied and complex, containing many defects which contribute to a lowering of the intensity of the Er columns directly at the interface. A new strain reduction mechanism is observed where the silicide nanostructure drops down a single Si step on the substrate surface. A structure model of this mechanism is proposed. The nanostructures have shown a preference for the triangular projection of Er columns at the interface which is not thought to be a remnant of the new orientation relationship, but a strain reduction mechanism that competes with the double stepped interface. Some interfaces have been found to have Er columns shifted from their expected positions up into the silicide. This was attributed to an ordering of the vacancies within the ErSi_{2-x} silicon lattice at the interface.

Contents

List of Tables

List of Figures

Acknowledgements

A short word of thanks to those people who made this work possible

Jun Yuan & Steven Tear for providing the guidance

Andrew Vick for fixing the broken things

Leonardo Lari for supplying supplementary information and images

Mum for the last minute proof reading

Rob Armstrong for explaining the differential and making the gearbox understandable

Rene van de Locht for keeping me sane... ish

Declaration

The work presented in this thesis is based on my own research except where it is explicitly stated in the text. No part of this work has previously been submitted for any other qualification.

Jeremy Mitchell

To Mum and Dad

It turns out that it is possible to finish a post graduate degree...

Chapter 1

Introduction

This work focuses on the rare earth silicides and the low dimensional structures that they produce when grown on silicon surfaces, more specifically erbium disilicide (ErSi_{2-x}) nanowires on the silicon (001) face. This introductory chapter aims to give the reader an understanding of the basic concepts while providing some insight into the wider field of research. The importance of this work will be discussed in context of the wider field, highlighting the motivations for the research and the choice of system.

1.1 Basic Concepts

What Are The Rare Earths

The rare earth series includes the lanthanide series, yttrium and scandium [3, 30]. Yttrium and scandium are included as they have very similar chemical properties to the lanthanides. The lanthanide series is unique in the fact that their outer electronic shell, the 6s level, fills before the 4f [5]. This means that all the elements in the lanthanide series have very similar chemical and physical behaviours as their outer electronic configuration is identical [31]. The filling of the outer 6s shell before the inner 4f shell also leads to the lanthanide contraction effect [5, 32], where as the atomic number of the element increases, the atomic radius contracts. This is attributed to poor shielding of the nuclear charge which pulls the 6s shell closer to the nucleus [32]. The lanthanide contraction effect has been successfully used to tune desired properties of materials by careful selection of the lanthanide metal [33].

Element	Symbol	Z	Atomic Radius (pm)
Scandium	Sc	21	162
Yttrium	Y	39	180
Lanthanum	La	57	187
Cerium	Ce	58	182
Praseodymium	Pr	59	182
Neodymium	Nd	60	181
Promethium	Pm	61	183
Samarium	Sm	62	180
Europium	Eu	63	180
Gadolinium	Gd	64	180
Terbium	Tb	65	177
Dysprosium	Dy	66	178
Holmium	Ho	67	176
Erbium	Er	68	179
Thulium	Tm	69	179
Ytterbium	Yb	70	176
Luthetium	Lu	71	174

Table 1.1: A table showing various parameters of the rare earth series

1.1.1 What is a Silicide?

A silicide is a crystal that has silicon and ‘something else’ in its structure [34]. In microelectronics the properties of metal silicides on silicon surfaces have been very attractive and they have found uses as, Ohmic contacts [35], Schottky barrier contacts [35], gate electrodes [36], local interconnects [37], diffusion barriers [38] and transistors [39]. The attractive properties of the transition metal silicides, including near-noble and refractory metal silicides for microelectronics when a metallic area is required are, in general; metallic behavior, i.e. low resistivity, a good adhesion to silicon to avoid delamination of the silicide, thermal stability to avoid altering the properties during use of the device, appropriate Schottky barrier height, high resistance to corrosion and oxidation, low interface stress and compatiblity with other processing steps [38]. These stringent conditions mean that at present only three silicides are commonly used, $TiSi_2$, $CoSi_2$ and NiSi [38].

Rare Earth Silicides

The rare earth silicides grown on silicon have some extremely attractive physical and electronic properties. They grow on silicon (001), which is the technologically more important face of silicon as the current generation of electronic devices are grown on this face [40].

They are metallic [41], and have low resistivities [1]. They have no reported history of delamination from the silicon surface, are thermally stable [42] and have an extremely low Schottky barrier height on n-type silicon [43]. Research has been carried out over the last 30 years in order to harness these very attractive properties for uses in electronic devices [39]. In recent years the rare earth silicide on silicon systems have exhibited interesting quantum and fundamental physical phenomena, that has maintained the research interest [13, 44, 45].

1.1.2 What Are Low Dimensional Structures?

A low dimensional structure is one that is constrained in one or more dimensions. A thin film is confined in one dimension where a nanowire is confined in two and a quantum dot is confined in three. There are many different methods that are used to produce these low dimensional structures that can be roughly grouped into 'top down' methods and 'bottom up' methods [30, 46]. The differences between the two types will be discussed later with examples. These low dimensional structures have many properties that make them extremely attractive for industrial applications [47] as well as making interesting study cases for novel quantum effects [46, 48]. Which means that a huge amount of scientific research has been conducted into both the obtaining of desired properties and the production of nanostructures [49–51].

1.1.3 Why Do We Want Low Dimensional Structures?

As the dimensions of a material are reduced to the scale of nanometres, often its mechanical, electrical and chemical properties drastically change. An example of this is the quantum laser [52, 53]. This device is similar in design to a laser diode, however the active region of the quantum laser is narrow enough for quantum confinement of the electrons to occur. In this regime the wavelength of the light emitted from the quantum laser is not determined by the band gap of the semiconductor as it would be in a conventional device, but is determined by the width of the active region. This allows much shorter wavelength lasers to be produced than conventional methods as the wavelength of the laser can be tuned during production by varying the dimensions of the active region [54]. These devices also have greater efficiencies than conventional laser diodes due to the modified shape of the density of states due to the device's small size [55].

The properties of nano-sized systems are not only altered by the confinement of electrons. In catalytic materials, when the size is reduced to the nanoscale, a considerable portion of the atoms within a system can be at edges, surfaces or corners. As these atoms are responsible for the catalytic properties the reactivity of the same volume of material drastically increases as the individual particle size decreases [56].

1.1.4 Why Do We Want Nanowires

In a system that is confined in two dimensions i.e. a nanowire, the confinement of electrons leads to phenomena such as charge ordering [13], non-classical electron transport properties such as ballistic transport [57], one dimensional Schottky characteristics [58] as well as one dimensional plasmons [45] etc. These new electronic behaviors open new avenues for research and industrial applications.

Nanowires have been highly sought after by the electronics industry, as in recent years the method to increase the power of electronics has been to decrease the size of the components and fit more of them into a given area. This requires ever smaller fundamental building blocks to produce these components and more compact ways to connect them.

A particular example of the use of nanowires in industry is the incorporation of silicon nanowires into lithium battery anodes. This particular application does not make use of the quantum confinement of electrons, but makes use of the high surface area of this geometry and the improved mechanical properties of the material at low dimensions [59]. Previous anodes have been made from graphite although this has a 10x lower theoretical lithium capacity than silicon, because silicon suffers from pulverization during charging and discharging as the silicon volume changes by 400% [60]. However by using silicon nanowires the large volume changes can be accomodated by the nanowires without fracturing allowing the use of this more attractive material.

1.1.5 How Are Low Dimensional Structures Produced

As previously stated the two classes of methods to produce low dimensional structures are top down and bottom up. Top down methods involve making larger materials smaller until they are the size that is required, which is predominantly achieved by lithographic processes. Bottom up methods involve assembling nanostructures out of smaller units

[46]. Most methods of nanowire production are bottom up methods as top down methods become limited and unreliable at the smallest length scales. Of these methods we shall discuss Photolithography, Vapor-Liquid-Solid (VLS) growth and Epitaxy and self-assembly.

In industry top down methods are the preferred methods to produce nanowires as these are well understood, fast and easy to control over large areas, allowing precise placement of the nanostructures required to build devices. However these techniques are nearing the limit of their capabilities to produce ever smaller structures in the current architecture designs. Either new architectures taking advantage of these well established technologies or new methods of production are required.

Photolithography

The most common top down method is photolithography which is used extensively in microelectronics. The technique allows a structure to be produced on a surface with a pre-prepared geometric pattern. A substrate is covered with a light sensitive ‘photoresist’ which is then selectively exposed to light, using the pre-patterned mask. The areas of the photosensitive resist that are exposed to light are removed uncovering the underlying substrate. This is then chemically or plasma etched, patterning the substrate. The remaining photoresist is then removed leaving the patterned substrate. This procedure can be repeated many times with stages of ion implantation to produce the complex structures used in microelectronics. The features that are produced using the photolithography can be as small as $\sim$30nm [61]. However advances in lithographic techniques have been continually improving the smallest feature size of this technique for many years.

Vapor-Liquid-Solid growth

VLS growth was first reported in 1974 by Wagner et. al. [62], however it has received a lot of attention in recent years as it is able to produce nanowires that stand upright on the substrate surface [63–65]. It is a specialized case of Chemical Vapor Deposition (CVD) which is frequently used by the semiconductor industry to produce thin films. Typically the substrate is exposed to a precursor gas (chemical vapor) containing the material that is to be deposited, at high temperatures. The precursor gas then reacts with the substrate and the desired material is deposited onto the surface. Any by-products are then pumped away. In VLS growth a liquid metallic particle on the substrate surface catalyzes a reaction between two precursor gases and absorbs a product. When the particle reaches its saturation point any further absorption forces some of the dissolved material to precipitate out as a solid. This occurs at the interface of the liquid metallic droplet and the substrate. As this process continues a column of deposited material appears underneath the metallic droplet. This method is characterized by producing long ‘whiskers’ of material with a metallic bead at the end. It is this method that was used to produce the silicon nanowires for the lithium battery anode mentioned above.

Epitaxy and Self Assembly

Epitaxy is ‘the natural or artificial growth of crystals on a crystalline substrate that determines their orientation’ [34]. In practice epitaxy involves depositing a small amount of material onto an exceptionally clean surface, usually at elevated temperature, in Ultra High Vacuum (UHV). Using this technique it is possible to grow crystals one atomic layer at a time, and even deposit sub-monolayer amounts of material, i.e. less than the number of atoms that it would take to cover the surface. With this extreme control over the growth rate and amount of deposited material it is possible to choose a substrate and over-layer that will self assemble into desirable structures. When the over-layer crystal has lattice parameters that are extremely close to that of the underlying substrate, within $\sim 2\%$, continuous defect free film growth is achieved; however by choosing over-layers with lattice parameters that are outside of the $\sim 2\%$ defect free growth regime, quantum dots or wires can be produced.

1.2 Nanowires in Future Electronics

As previously stated new methods of producing smaller features or new architectures are being explored in order to find new areas for device improvement. One such technique that has been proposed is self assembled circuits. However this method has proved technologically challenging, and improving architecture can be done with traditional techniques, so self-assembled circuitry is unlikely to become the mainstay of future electronics in the short term, however these self-assembled structures may find more specialized functions.

1.2.1 Silicon Nanowires in Future Electronics

Silicon nanowires have been suggested for use in the next generation of solar cells. By coating or doping the nanowires, p-n junctions can be made with novel morphologies. The intrinsic shape of the structures has been shown theoretically to improve the conversion efficiency of the devices as much higher surface areas can be achieved. Fig. 1.1 shows a structure that was published by Cheng et. al. [6], where silicon nanowires were coated in transparent indium tin oxide (ITO). This solar cell structure was shown to have an efficiency of 10%, as compared to the nanowires without the ITO with an efficiency of just 2.4%. These efficiency figures are still much lower than more established technologies which can be up to 40% [66], but the low cost of production of the silicon nanowire based devices, offers considerable benefit [6], and further research offers the possibility of improving the efficiency further.

1.2.2 Parallel Wire Arrays in Future Electronics

It is currently impossible to direct the growth of self assembled epitaxial nanowires in a scalable way; however it is possible to easily and cheaply encourage nanowires to grow into parallel arrays over large areas. Different architectures are being considered [67] to exploit these potentially useful structures that can be grown to have dimensions that are much smaller than current lithographically produced wires.

The ‘crossbar’ architecture, which is based on two orthogonal parallel wire arrays, is well suited to take advantage of the parallel nanowire arrays, while utilizing active molecules at the junctions of these nanowires [7, 30, 68]. Fig. 1.2 shows a schematic of the architecture showing the main features.

Another potential use for massively parallel nanowire structures are polarizers [45]. By exploiting the one dimensional nature of metallic nanowires, their plasmon resonances can be used to polarize light.

Rare earth silicides on silicon, at low coverages, have been shown to self assemble into conducting nanowire arrays. These arrays can be encouraged to grow either in two perpendicular directions or as a massively parallel array [28]. Due to their unique Schottky barrier characteristics and metallic behavior they are a strong contender for applications where parallel arrays of nanowires are attractive.

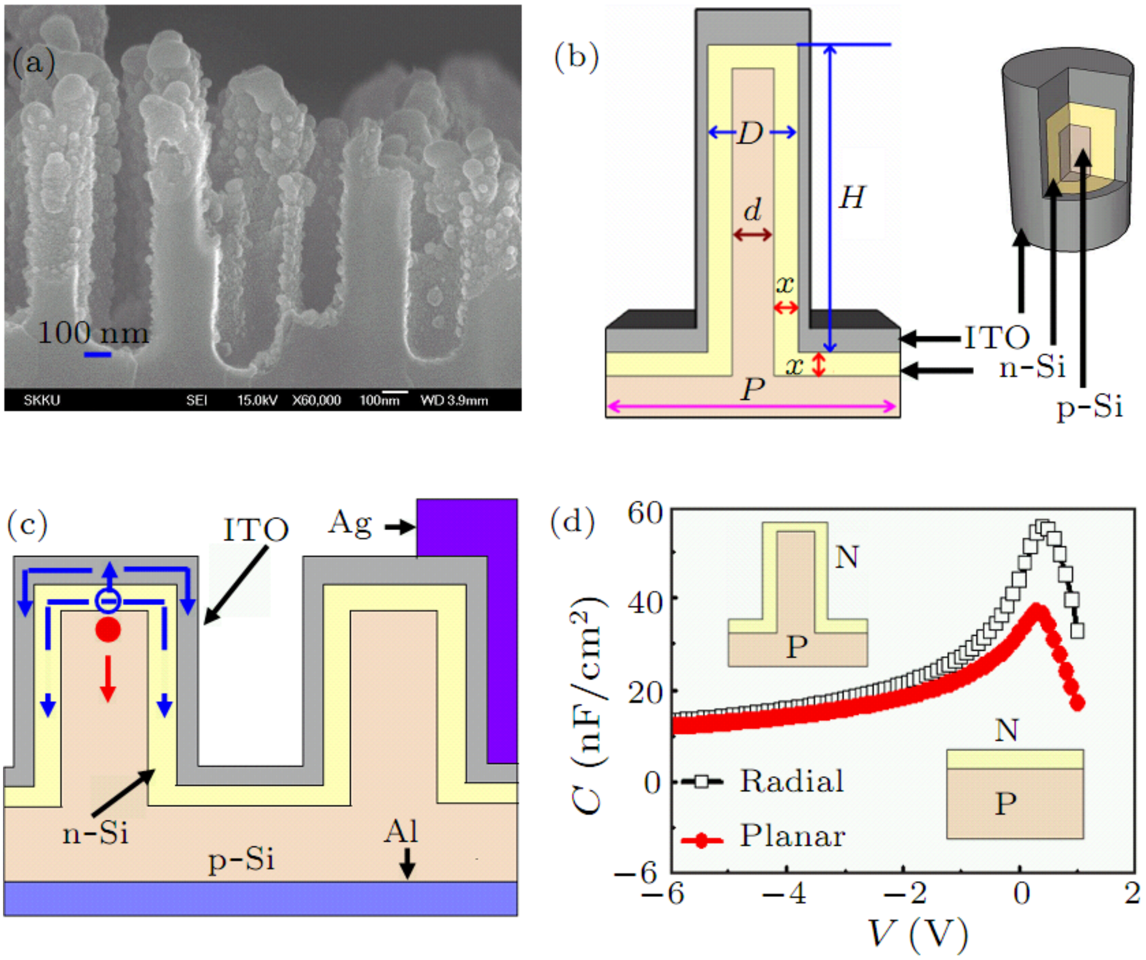

Figure 1.1: A figure from Cheng et. al.'s paper [6] showing the structure of silicon wire based solar cell. (a) as imaged in SEM (b)&(c) schematics (d) the increase in capacitance associated with the nanowire morphology.

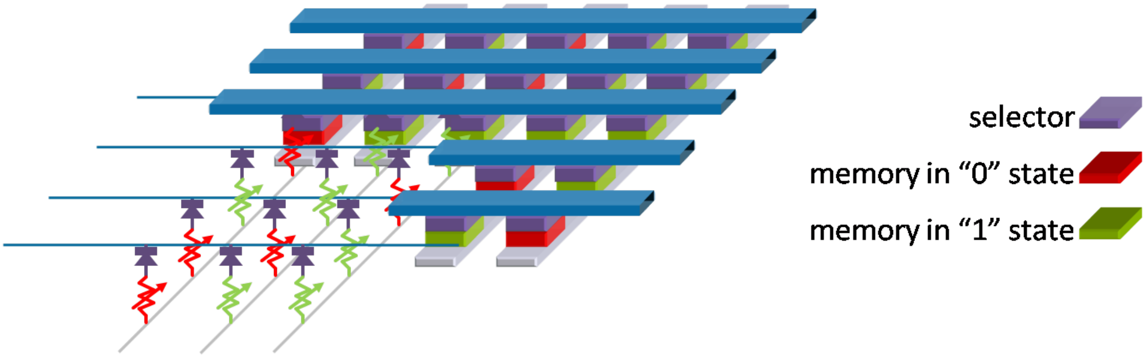

Figure 1.2: An image from [7] showing the main features of the crossbar architecture

1.3 This Work

Here we will investigate ErSi_{2-x} nanowires and their interfaces. Erbium silicide was chosen as it has been shown to have the highest conductivity of all the rare earth silicides, and is therefore an attractive candidate for any applications [1]. We shall investigate, but not exclusively, nanowires of less than 5nm in width in order to better understand the structure of this interesting system in this critical region.

We shall be using aberration corrected Scanning Transmission Electron Microscopy (STEM) as the high chemical contrast of the imaging technique will allow us to easily identify the Er and Si columns while the incoherent imaging will give accurate structural data. We will utilize capping techniques so that the smallest features survive, while showing that this procedure does not affect the structure of the nanowires. The evolution of the nanowires as a function of width is also discussed along with the implications that the results have for the accepted growth model.

Chapter 2

Erbium Silicide on Silicon

This chapter describes the erbium silicide system on silicon, focusing on the Si(001) surface. The crystal structure of erbium silicide will be discussed and the structural considerations relevant to this work highlighted.

A short literary review of the work performed to date, highlights the important findings and current gaps in the knowledge base. The growth mechanism and structure of the rare earth silicides nanowire system receives particular attention as our results directly impact this area, and many of the calculations and simulations performed on the rare earth silicide nanowire system to date use assumptions based on the accepted growth model.

2.1 Erbium Silicide Crystal Structure

2.1.1 Phases of the Erbium Silicide System

The erbium silicide system has been shown by Luzan et. al. [1] to exhibit many different phases depending on the stoichiometry. The phase diagram for the binary erbium silicon system and the structure models of the various phases are shown in Fig. 2.1 [3, 8–11].

The most stable phase on silicon (111) and (001) was found to be the ErSi_{2-x}. It is so highly favoured that the silicide will form silicon islands if there is an excess of silicon in order to correct the stoichiometry [69]. This stoichiometry has been shown to exhibit two polymorphs, a hexagonal phase, which is observed in bulk, and a tetragonal phase, which is thought to be induced by the interaction of the silicide with the Si(001) surface [70].

Silicide	Symmetry	Structure type	Lattice Parameters (Å) a	b	c
Er_5Si_3	$P6_3$/mcm	Mn_5Si_3	8.309±0.003	-	6.234±0.002
Er_5Si_4	Pnma	Sm_5Ge_3	7.28±0.05	14.37±0.16	7.595±0.016
Er_1Si_{1-x}	Cmcm	CrB	4.196±0.003	10.382±0.003	3.787±0.004
ErSi	Pmna	FeB	7.77±0.007	3.784±0.001	5.607±0.003
$ErSi_{2-x}$	P6/mmm	AlB_2	3.8006±0.0024	-	4.0856±0.0008
$ErSi_{2-x}$*	I41/AMD	ThSi	3.96±0.02	-	13.26±0.02

Table 2.1: The symmetry and lattice parameters for the various structures of the binary erbium silicon system found by Luzan et. al.[1] in the erbium phase diagram shown in Fig. 2.1.*With the exception of the tetragonal phase where the lattice parameters were obtained separately [2].

	Hexagonal	Tetragonal
Space Group	P6/mmm	I41/AMD
Structure Type	AlB_2	$ThSi_2$
RE position	000	$\frac{1}{2}\frac{1}{2}\frac{1}{2}$
Si position	$\frac{2}{3}\frac{1}{3}\frac{1}{2}$	$1\frac{1}{2}\frac{2}{3}$

Table 2.2: The symmetry and atomic positions of the rare earth and silicon for the hexagonal and tetragonal unit cell [3]

The symmetry and lattice constants of the various phases found by Luzan et. al., that were shown in Fig. 2.1 are shown in Table 2.1, together with the tetragonal phase which was reported elsewhere [2].

2.1.2 $ErSi_{2-x}$ Crystal Structure

$ErSi_{2-x}$ is the only stable stoichiometry on silicon surface therefore we shall only consider this stoichiometry from this point.

The unit cells of the hexagonal and tetragonal $ErSi_{2-x}$ (in this case x=0) systems are fully described by the information in Tables 2.1 and 2.2. Table 2.1 gives the unit cell parameters, where Table 2.2 gives the atomic positions.

The two orthogonal projections of the phases of $ErSi_{2-x}$ produced using this information are shown in Fig. 2.2. In reality there is a vacancy structure within the silicon network that reduces the stoichiometry to $ErSi_{2-x}$ [71, 72], where $x \sim 0.3$.

The hexagonal and tetragonal phases are both comprised of a triangular subunit of Er

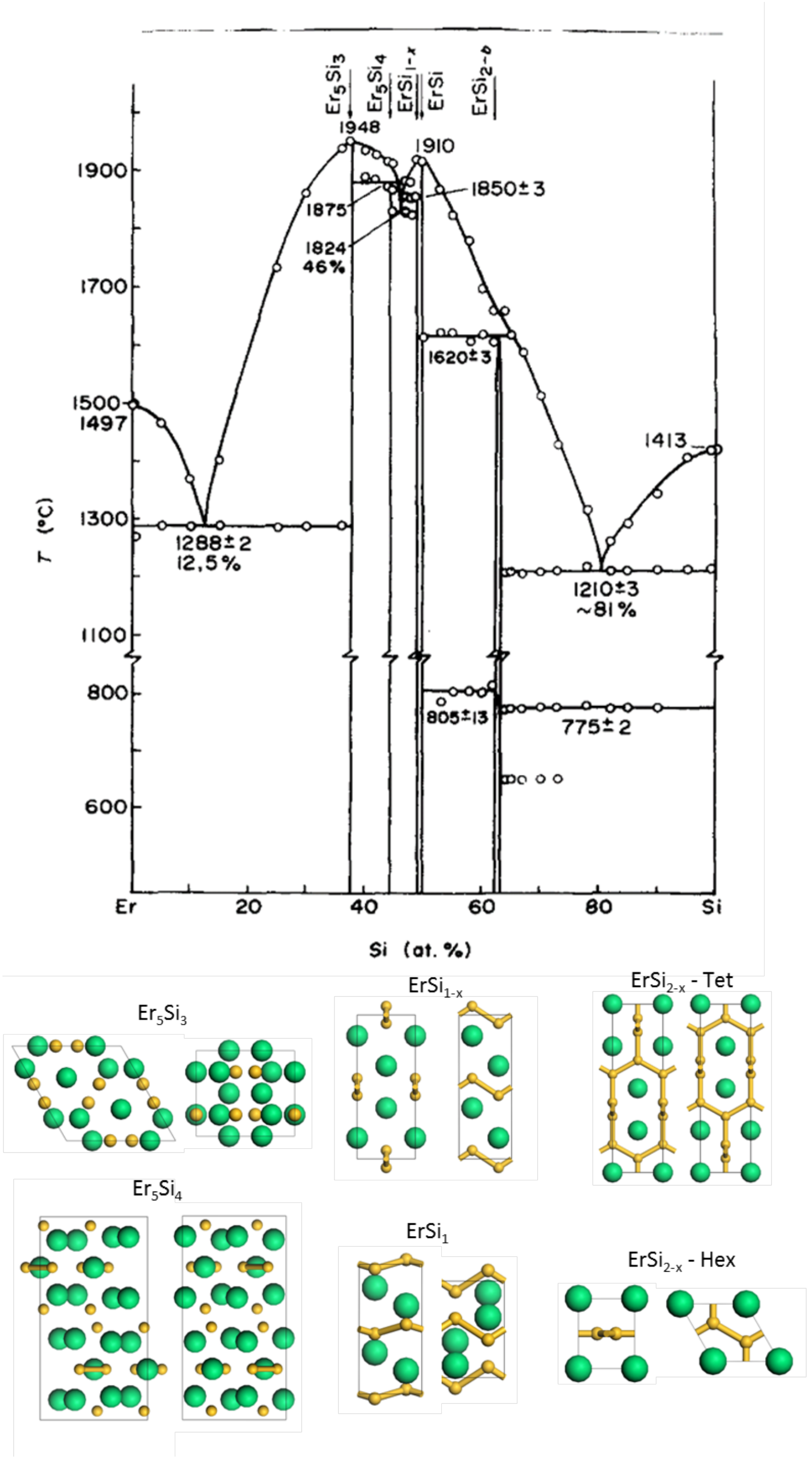

Figure 2.1: The phase diagram for the binary erbium silicon system as reported by Luzan et. al. [1] with two orthogonal projections for each of the possible Er_xSi_y stoichiometric phases (not to relative scale)[3, 8–11]

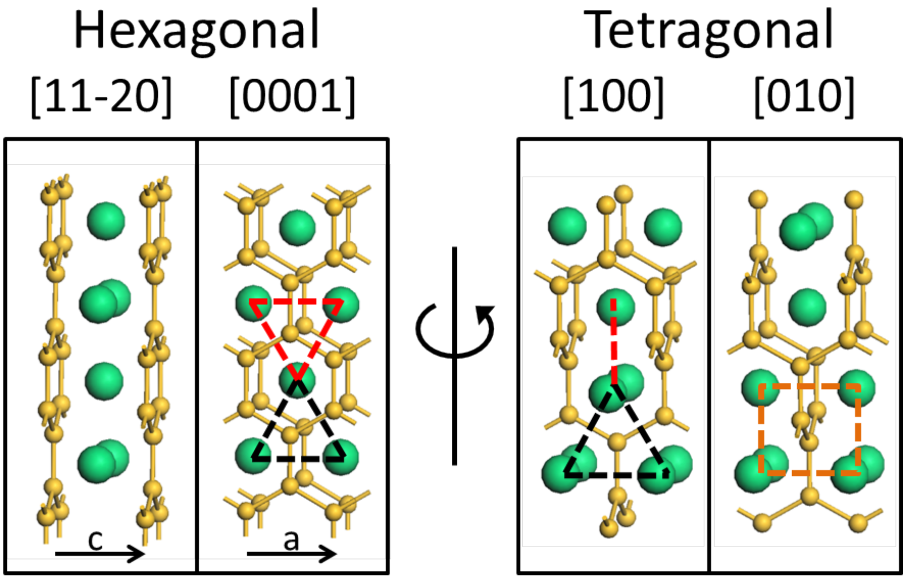

Figure 2.2: Two orthogonal projections of the two phases of ErSi_{2-x}, the large green circles represent erbium and the smaller yellow circles represent silicon. The black dashed lines indicate the triangular subunit that is common between the two phases. In the tetragonal phase the subunit rotates through 90°, where in the hexagonal phase all the units are in plane as indicated by the red dashed lines. The orange dashed square indicates the square projection that is obtained with a 90° rotation of the triangular projection. The direction of rotation is indicated by the central black arrow.

atoms as highlighted in Fig. 2.2 by the dashed red and black triangles. In the hexagonal phase the triangular subunits are all in plane separated by a graphene-like layer of sp^2 bonded Si atoms, which contains the vacancy structure [73]. In the tetragonal phase, the triangular sub unit rotates through 90° as the crystal increases in thickness, by rotating a silicon sp^2 bond through 90°. This results in a shift of the Er position every two atomic layers. It is worth highlighting at this point that the structure of the hexagonal and tetragonal phases, with respect to the Er positions, at thicknesses of less than 2 atomic layers, are identical and can be transformed by a 90° rotation of the whole crystal. The dashed black triangle and dashed orange square indicated in Fig. 2.2 shall be used to classify interface structures in later chapters.

2.2 Growth of Rare Earth Silicide thin films on Silicon

The growth of rare earth silicides on silicon faces was demonstrated in 1980 by Baglin et. al. [74] on the Si(111) and Si(001) surfaces. Subsequent research found that on Si(111) the silicide formed high quality layers as the silicides have a good lattice match with the

Si(111) [43, 73], where the poor match for Si(001) led to highly defected films [75, 76].

Good quality epitaxial layers on Si(111) were first achieved by Knapp et. al. [73] in 1986 when a contamination layer at the interface between the Si and RE was identified and removed by rapid e-beam heating to high temperature. This highlighted the sensitivity of the silicide formation to contamination; however this process has not been necessary in recent years due to the improvement of vacuum technology and the surface cleaning process.

Arnaud d'Avitaya et. al. found that co-depositing Si and Er together on the Si surface with a ratio of $\sim$ 2:1 produced high quality films [77]. Co-deposition is technically challenging so Sieagal et. al [78] produce high quality rare earth silicide thick films by borrowing a technique shown to work in other silicide systems by Tung et. al. [79, 80].

It has been found that a thin layer of $NiSi_2$ acts as a template for the further growth of a thicker $NiSi_2$ film, hence improving the quality of the thicker layer.

In 1992 Paki et. al. [81] succeeded in producing a 2D $ErSi_{2-x}$ layer on Si(111). The structure was determined through a combination of Low Energy Electron Diffraction (LEED), angle resolved ultraviolet photoemission spectroscopy and x-ray forward scattering techniques. They reported that the structure was hexagonal with a reconstructed Si top layer.

In order to better understand the growth mechanisms of the rare earth silicides Baglin et. al. [82] performed High Resolution Transmission Electron Microscopy (HRTEM) marker experiments to determine the mobile species. The diffusing species was determined by using a bilayer of two rare earth metals, grown on a silicon substrate, that were shown not to intermix upon heating. It was determined that the Si was mobile and the rare earth atoms almost immobile.

2.2.1 Structure of Erbium Silicide on Silicon

Orientation Relationship of $ErSi_{2-x}$ on Si(111) or Si(001)

By examining the bulk structures of the hexagonal rare earth silicide and the Si (111) and (001) faces it is possible to postulate the orientations in which we would expect the hexagonal silicide to grow on the silicon substrate. The Si(111) face has a hexagonal symmetry and the Si(001) has a square symmetry, so we would expect the silicide to form with its c-axis perpendicular to the Si(111) face and parallel to the Si(001) face. This was confirmed experimentally from multiple Transmission Electron Microscopy (TEM) diffraction studies [70, 83]. The orientation relationships can be expressed as:

On Si(111)

$$Hex : (111)_{Si}/(0001)_{RESi_{2-x}}, [1\bar{1}0]_{Si}/[11\bar{2}0]_{RESi_{2-x}} \tag{2.1}$$

On Si(001)

$$Hex : (001)_{Si}/(01\bar{1}0)_{RESi_{2-x}}, [110]_{Si}/[11\bar{2}0]_{RESi_{2-x}} \tag{2.2}$$

$$Tet : (001)_{Si}/(001)_{RESi_{2-x}}, [110]_{Si}/[100]_{RESi_{2-x}} \tag{2.3}$$

Misfit and Strain

It has been found through experiment that in general a misfit of $\sim< 2\%$ is required for high quality epitaxial growth of an overlayer on a substrate [84]. If the misfit is greater than this, in general the system will form defects to reduce the strain energy [85]. The rare earth silicides do not match to the silicon (001) or (111) surfaces exactly, so strain is introduced when a rare earth silicide is grown on these faces. As an example the misfit for the erbium silicide on silicon (001) and (111) are given below, assuming the orientation relationships given in the equations Equ:(2.1), (2.2) & (2.3) the lattice constants given in table 2.1:

ErSi$_{2-x}$ on Si(111):

$$\begin{aligned} Hex : [01\bar{1}]_{Si}/[2\bar{1}\bar{1}0]_{ErSi_{2-x}} &= -1.6\% \\ [10\bar{1}]_{Si}/[1\bar{2}10]_{ErSi_{2-x}} &= -1.6\% \end{aligned} \tag{2.4}$$

ErSi$_{2-x}$ on Si(001):

$$\begin{aligned} Hex : [110]_{Si}/[11\bar{2}0]_{ErSi_{2-x}} &= -1.6\% \\ [1\bar{1}0]_{Si}/[0001]_{ErSi_{2-x}} &= +6.3\% \end{aligned} \tag{2.5}$$

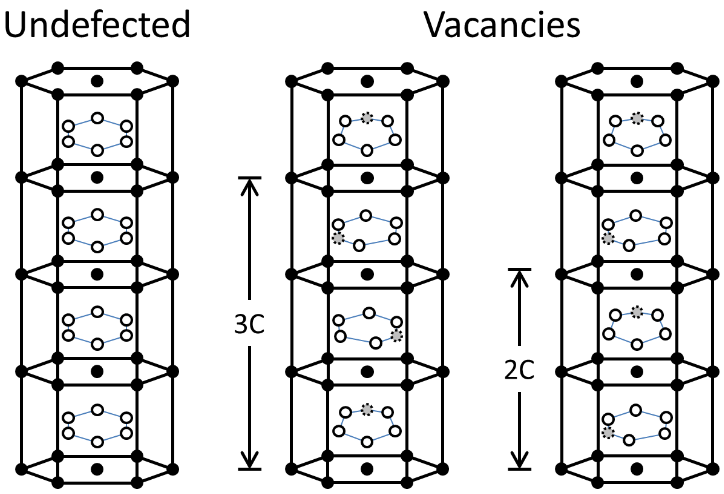

Figure 2.3: A representation of the 2C and 3C observed vacancy structures for hexagonal rare earth silicide alongside the undefected structure. The 2C and 3C ordered vacancy structures have a shift of the silicon positions associated with the vacancy. Black circles represent the rare earth positions, the white circles the silicon positions and the dashed gray circles the vacancy positions.

$$\begin{aligned} Tet: [100]_{ErSi_{2-x}}/[110]Si &= +3.1\% \\ [010]_{ErSi_{2-x}}/[1\bar{1}0]Si &= +3.1\% \end{aligned} \tag{2.6}$$

Vacancy Structure

Baptist et.al [86] showed through x-ray photoelectron diffraction that the aforementioned vacancies that were known to exist within the silicon lattice in the RESi were ordered and form a $\sqrt{3} \times \sqrt{3}R30^\circ$ superlattice within each Si plane. Lohmeier et. al. [71] using surface x-ray diffraction showed that the ordering of the Si vacancies was strongest at the interface. Fig. 2.3 shows the ordering of vacancies within the hexagonal rare earth silicide. In films the vacancies have been shown to order with a variety of periodicities from 2C to 4C, where C refers to the hexagonal c-axis [69, 72, 87]. The ordered vacancies have been shown, by calculations published by Stauffer et. al. [88], to alter the electrical structure of the silicide.

Further calculations on the ErSi$_2 - x$ crystal including the vacancy structure have shown that the diffusion of silicon within the silicon planes is $\sim 10^{14}$ more likely at 500° C than across plane [89].

2.2.2 Discovery of Nanowires

Work on growth of rare earth silicides on the Si(001) crystal face also began in 1980 [74], however it was not until 1998 that Preinesberger et. al. [31] noticed that sub monolayer amounts of RE deposited onto a hot Si(001) crystal self assembled into nanowires that grew flat along the Si(001) surface.

This discovery lead to an increased interest for RE on Si(001) as the nanowires have been shown to exhibit some extremely interesting one dimensional phenomena [13, 44, 45], as well as being shown to be metallic [90, 91] and robust [92, 93] giving them potential applications in industry for microelectronics. Erbium silicide nanowires grown on the Si(001) surface will be the main focus of this thesis.

2.3 Structure of Rare Earth Silicide Nanowires on Si(001)

The accepted structure for the nanowires was proposed by Chen et. al.[12] and is shown in Fig. 2.4. The figure shows the interface between the bulk silicon and the hexagonal $\mathrm{RESi}_2 - x$ overlayer as viewed along the direction of extended growth. This structure is analogous to the thin film orientation relationship given in Equ (2.2), with the direction of extended growth of the nanowire perpendicular to the c-axis in the hexagonal silicide, and in this case, into the page.

The nanowires have been observed to coexist with larger rectangular or square nanostructures [28, 94, 95]. These rare earth silicide nanostructures were categorized according to their aspect ratio by Ding et. al.[4] into three groups, nanowires, rectangular islands and square islands. The average parameters for the three categories that were used are shown in Table 2.3. We shall be using a system where the nanostructures will be characterized by their width as our cross sectional experimental methods do not reveal information about the length of the nanostructures.

Our classifications shall be similar to Ding's in that anything wider than 10nm shall be referred to as an 'island'. We shall not split this into rectangular and square as we are unable to determine if the nanowire was rectangular or square but we are able to directly observe the polymorph of the ErSi_{2-x} island by examining the atomic structure from our images. We categorise 'nanowires' into 'ultra-small nanowires' with widths $\leq$5nm and

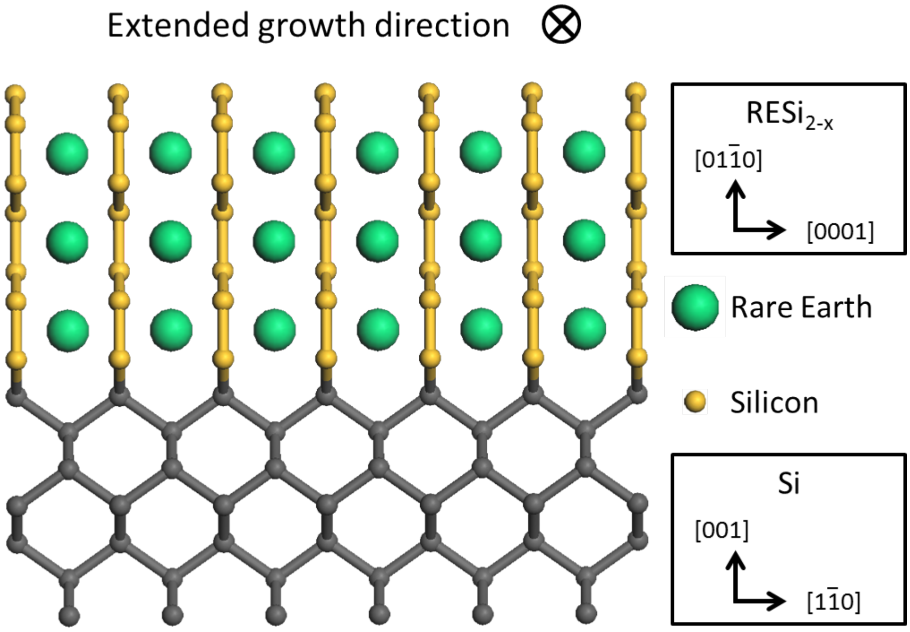

Figure 2.4: The structure proposed by Chen et. al.[12] to describe the nanowires, viewed along the direction of extended growth. The large green circles represent rare earth atoms and the small yellow / gray circles represent silicon.

	Length (nm)	Width (nm)	Height (nm)	Aspect Ratio (length/width)	Structure
Nanowires	20 ∼ 1000	0.8 ∼ 10	0.3 ∼ 2.0	5.0 ∼ 100	AlB_2
Rectangular Islands	10 ∼ 100	10 ∼ 25	1.5 ∼ 3.5	2.0 ∼ 5.0	AlB_2
Square Islands	10 ∼ 50	10 ∼ 60	3.0 ∼ 8.5	0.5 ∼ 2.0	$ThSi_2$

Table 2.3: Results published by Ding et. al.[4] and their classification of the rare earth silicide nanostructures according to their aspect ratio.

'nanowires' with widths 5-10nm as these two regimes have been found to behave differently.

2.3.1 DFT and STM Modeling

The smallest nanowires have been modeled using density functional theory (DFT) to find structures that match with STM data [13, 15], and find the lowest energy structures [14, 16]. All structures reported are modeled using yttrium as the rare earth metal, as it has fewer electrons than any of the lanthanides. This makes the calculations quicker, and in some cases makes the calculation achievable rather than impossible with the available computing power. There have been questions about the comparability of results obtained using simplified models of the lanthanide metals [96], however due to the comparable physical and chemical properties of yttrium with the lanthanides in general the simplification appears valid [13–16].

Eames et. al. [16] calculated the energy of different nanowire structures (Hexagonal or Tetragonal) with different local silicon surface reconstructions and found that their model predicted that for a given orientation with respect to the surface reconstruction the tetragonal silicide was lower in energy. The lowest energy configuration was found to be a 'tetragonal' nanowire parallel to the dimer rows. Two of the four structures that were used are shown in Fig. 2.5(D)&(E). The two different silicide phases used in this study are distinguished by a different surface reconstruction of the uppermost silicon layer in the nanowire, this is shown in Fig. 2.6.

Due to the fact that the tetragonal and hexagonal phases of erbium silicide can be transformed at this level by a 90° rotation, we can model this 'tetragonal' nanowire as 'hexagonal' with its c-axis parallel to the growth direction. As this structure is lower in energy regardless of the local Si reconstruction we would expect this structure to be favoured - which is in direct contradiction with the accepted growth model. This contradiction will be discussed in greater detail later.

2.3.2 Vacancy Ordering in Nanowires

Tasi et. al. [72] studied the rare earth silicide nanostructures through plan view and cross sectional TEM and diffraction. They showed that extra spots that appeared in the diffrac-

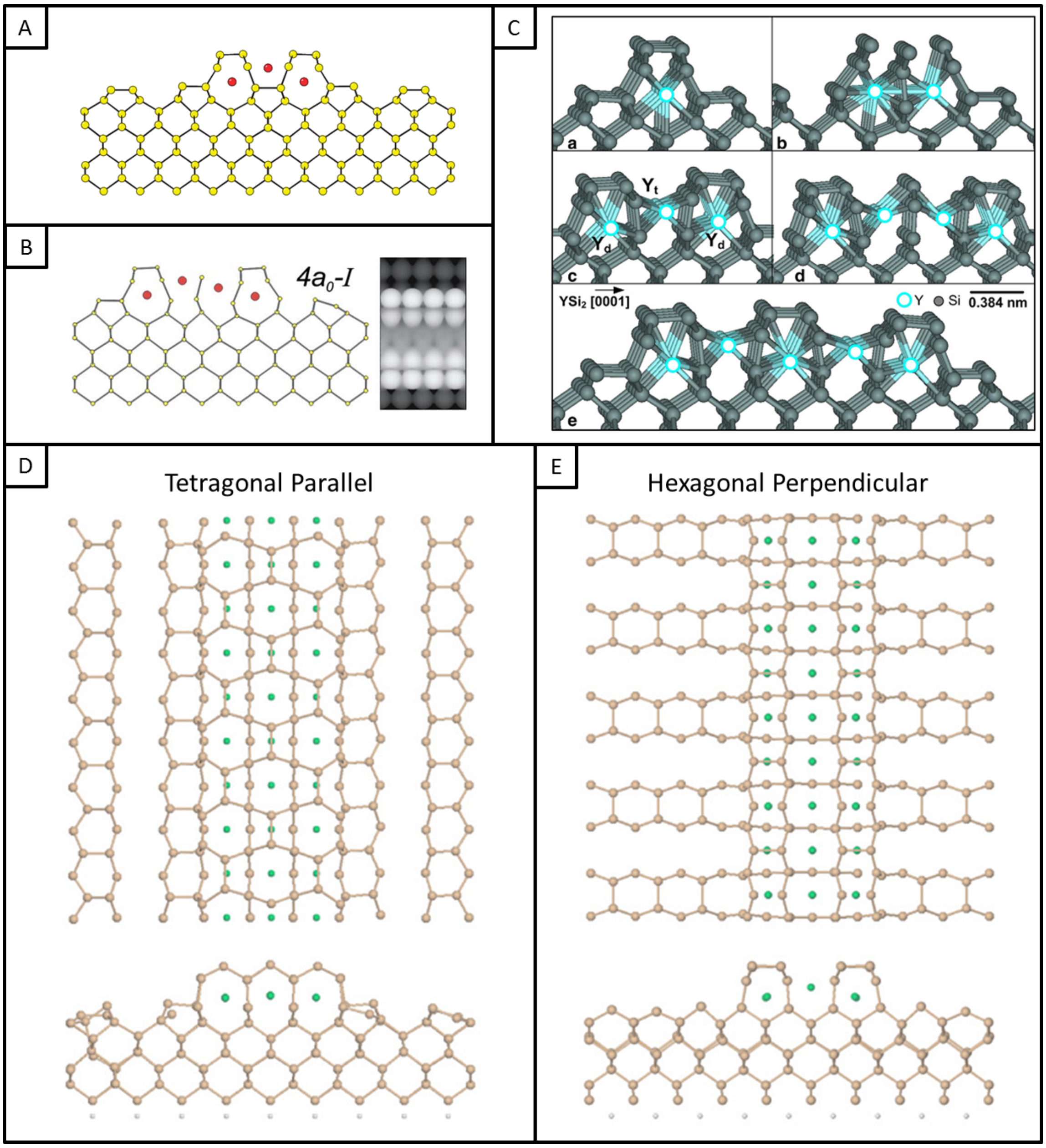

Figure 2.5: Some of the structures that have been used in DFT modelling. (A) The structure used by Zeng et al. in their paper[13] where, yellow represents silicon and Red represents yttrium. (B) The structure used by Iancu et al in their paper[14], where yellow represents silicon and red represents yttrium. (C) The structures proposed by Shinde et. al. [15] for 5 different widths of nanowire from $1a_0$ to $5a_0$ where grey represents silicon and the open blue represents yttrium. (D)&(E) show the structures from Eames et. al.'s paper [16] for two different nanowire structures grown on two different local Si(001) surface reconstructions, where brown represents silicon and green represents yttrium.

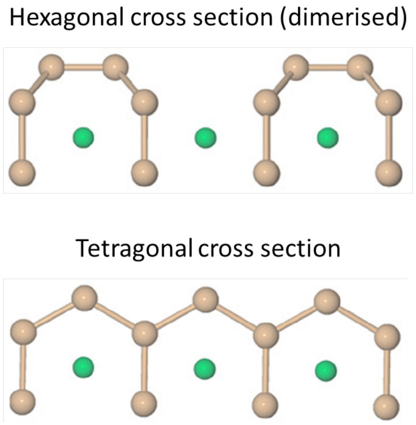

Figure 2.6: The cross sectional views from the tetragonal and hexagonal nanowires that were used in Eames et. al.'s publication [16]. The difference between the two structures is the termination of the silicon surface. These two structures can be transformed from one to the other by a 90° rotation of the silicide crystal, allowing the 'tetragonal' silicide to be modeled as a hexagonal with its c-axis parallel to the growth direction.

tion pattern are well described by an ordered vacancy structure within the nanowire systems [72]. They also conclude from the periodicity of the diffraction spots associated with the ordered vacancies, that the vacancies within the nanowire exist in the 2C ordered state rather than in the 3C thin film case, see Fig. 2.3. They argue that the strain relaxation at the surface affects the vacancy ordering within the nanowire and encourages a more ordered state. As of yet there have been no direct observations of the vacancy structure within the nanowires.

In theory, if the vacancies are ordered within the nanowire it should be possible to image them. If the vacancies are 1C ordered the vacancy will appear as a missing atom in an image, however if the ordering is 2C or greater the vacancies will only be detectable as a decrease in contrast for the affected columns. In practice this will require an extremely stable and high resolution microscope and many detailed simulations will be required for reference and comparison to the experimentally obtained images.

2.3.3 Strain Relief

Dislocations and Burgers Vectors

Dislocations occur at strained interfaces to relieve the strain energy within the crystal. As the strain energy increases either due to increasing lattice mismatch or increasing layer thickness, at some point the strain energy will be equal, or larger than the amount of energy required to introduce a defect to relieve that strain. A defect is characterized by an associated 'Burgers vector's' direction and magnitude.

Fig. 2.7 shows a simplified example of a misfit dislocation, where a crystal with a large unit cell has grown on top of a bulk crystal with a smaller unit cell. On the left the overlayer crystal is elastically strained to fit the substrate, where on the right the overlayer has incorporated a defect into its interface and the overlayer has relaxed slightly. The green line draws a circuit over the interface and in the right hand crystal, around the dislocation. In a non defected crystal, i.e. the 'Elastically strained' case, this circuit starts and ends at the same point. Whereas in the case where the circuit encloses a defect there is an extra vector required to close the loop. This is the Burgers vector that describes the defect and in this case is equal to 1 unit cell.

Dislocations at the RESi$_{2-x}$ nanostructure on Si(001) Interface

As the nanostructures get thicker and wider the strain in the system gets larger. At some point it becomes necessary to relieve that strain via defects. These interfacial defects have been studied in great detail using HRTEM [17, 97–100] and CLS Modeling [18].

Ye et. al. found that they observed a relative rotation of larger islands with respect to the silicon in the $[1\bar{1}0]$ direction [17]. This was found by looking at the Fourier transforms of the images of the islands, an image showing the tilting from their paper [17] is shown in Fig. 2.8(A).

This was later explained by Qiu et. al. when they applied a coincidence site lattice (CSL) model to the RESi system and found that the rotation allowed a lower energy stepped interface to be achieved [18]. Qiu et. al. found that for DySi$_{2-x}$ nanostructures, the lowest energy interface had steps of 7 atoms in width with a rotation of the whole nanostructure of $\pm 1.26^\circ$ in the $[1\bar{1}0]$ direction. The stepped interface and associated dislocation cores that they reported is shown in Fig. 2.8(B).

A representation of the interface step defects discussed by Qiu and Ye is shown in Fig. 2.8(C). The incorporation of a step allows the rare earth crystal to relax closer to its 'bulk' lattice constant. The green circuit around the dislocation shown in Fig. 2.8(C) highlights the Burgers vector of this dislocation shown in yellow, the green circuit shown on Fig. 2.8(B) is a similar circuit to the one shown in Fig. 2.8(C). In this example the Burgers

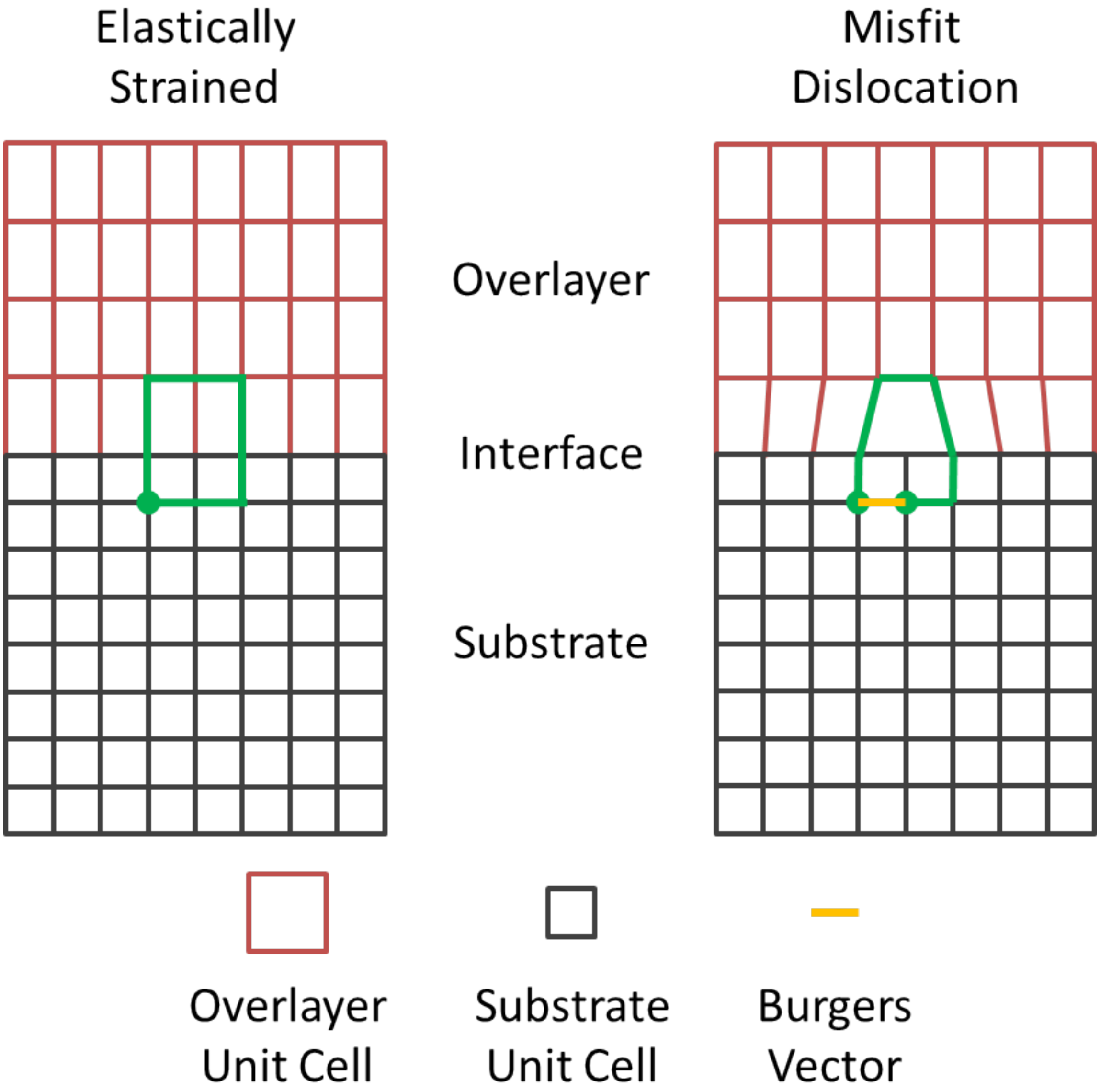

Figure 2.7: An example of a misfit dislocation. On the left the overlayer in red has been strained to epitaxially match the substrate. On the right the overlayer has slightly relaxed and incorporated a dislocation at the interface. The green line describes how to find the Burgers vector (highlighted in yellow) associated with the defect.

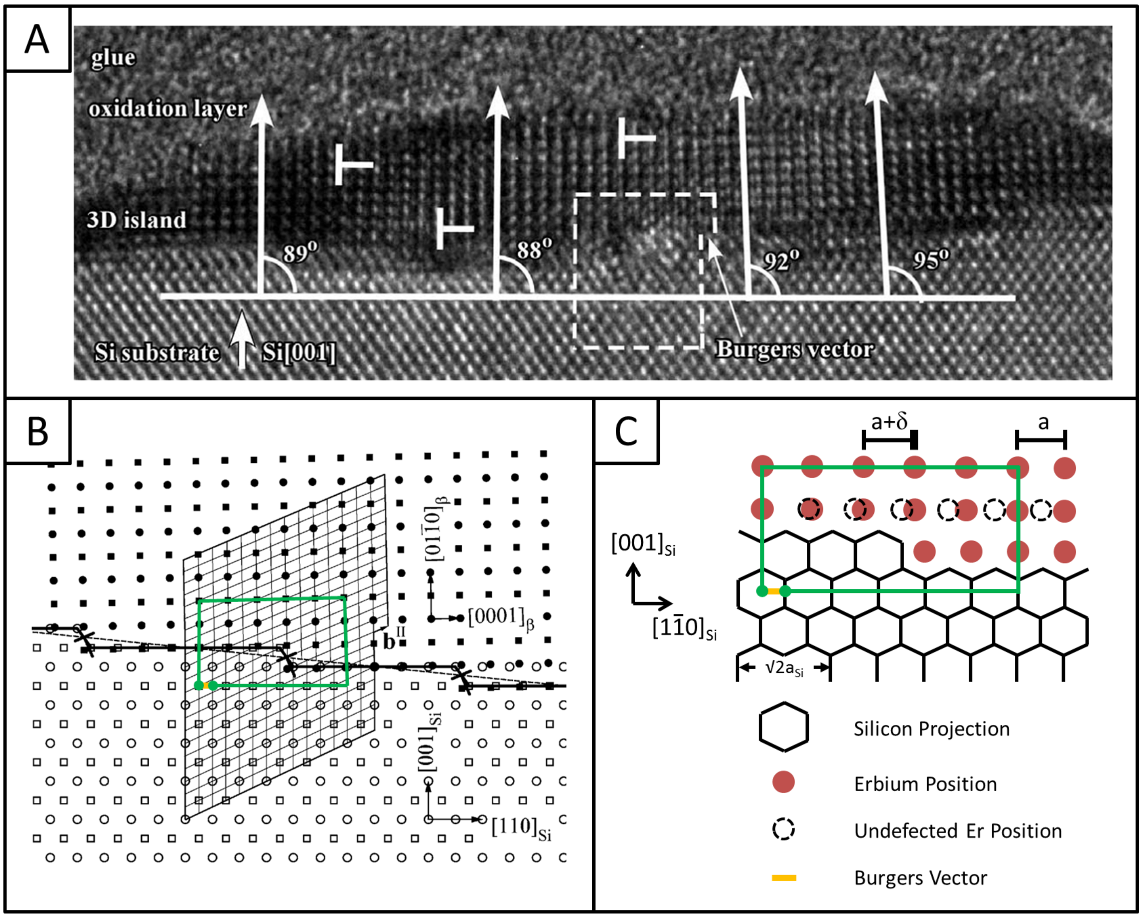

Figure 2.8: (A) An image from a paper by Ye et. al. [17] showing the rotation of a rare earth silicide island with respect to the silicon substrate. (B) A representation of the CSL model from Qiu's paper [18] showing their proposed lowest energy interface with associated dislocations and Burgers vector analysis. The upper black crystal representing the $DySi_2$ silicide is rotated 1.26° anticlockwise with respect to the lower white crystal representing Si. (C) A representation of the type of defected interface proposed by Ye[17] and Qiu[18]. The dashed black lines show where the erbium atoms would sit in an unrelaxed structure. The green lines indicate the circuit used to define the Burgers vector shown in yellow. In this example the Burgers vector is $\frac{\sqrt{2}}{4}a_{Si}$ in the $[1\bar{1}0]_{Si}$ direction.

vector is $\frac{\sqrt{2}}{4}\mathrm{a}_{Si}$ in the $[1\bar{1}0]_{Si}$ direction.

2.3.4 Rare Earth Silicide Nanowire Surface Reconstructions

The surface of the rare earth silicide nanostructures have been investigated by STM [19, 95] and there are many different surface reconstructions that are observed, which seem to have some dependence on the nanowire width. Liu et. al. detailed many of the different surface reconstructions [19] and an image from their paper is shown in Fig. 2.9. The smallest nanowires tend to have a $2\mathrm{a}_{Si}$ periodic surface where the larger nanowires tend to have a c(2×2) reconstruction. The surface reconstruction of the nanowire itself can provide some clues to the underlying bulk structure of the nanowire and help to provide some boundary conditions on possible nanowire structures and structure calculations.

Eames et. al. in their paper [16] note that the structures that are shown in Fig. 2.5(D)&(E) produce both of the most common observed surface reconstructions for the rare earth silicide nanowire system. Their 'tetragonal' nanowire adopts the c(2×2) reconstruction and the hexagonal nanowire adopts the much rarer (2×1) surface reconstruction. Eames et. al. conclude that most nanowires observed in STM are 'tetragonally terminated nanowires'. This implies that the vast majority of nanowires observed in STM can be modeled as hexagonal with the x-axis parallel to the growth direction.

2.4 Growth Mechanisms

After the discovery of the rare earth silicide nanowire system, questions about the growth mechanics became immediately important. As better knowledge of the growth mechanics would allow the growth method to be better tuned to produce the nanostructures that are of particular interest.

There are three main modes of thin film epitaxial growth. These will be discussed together with 'Ostwald Ripening' which describes the behavior of the rare earth silicide nanostructures during annealing.

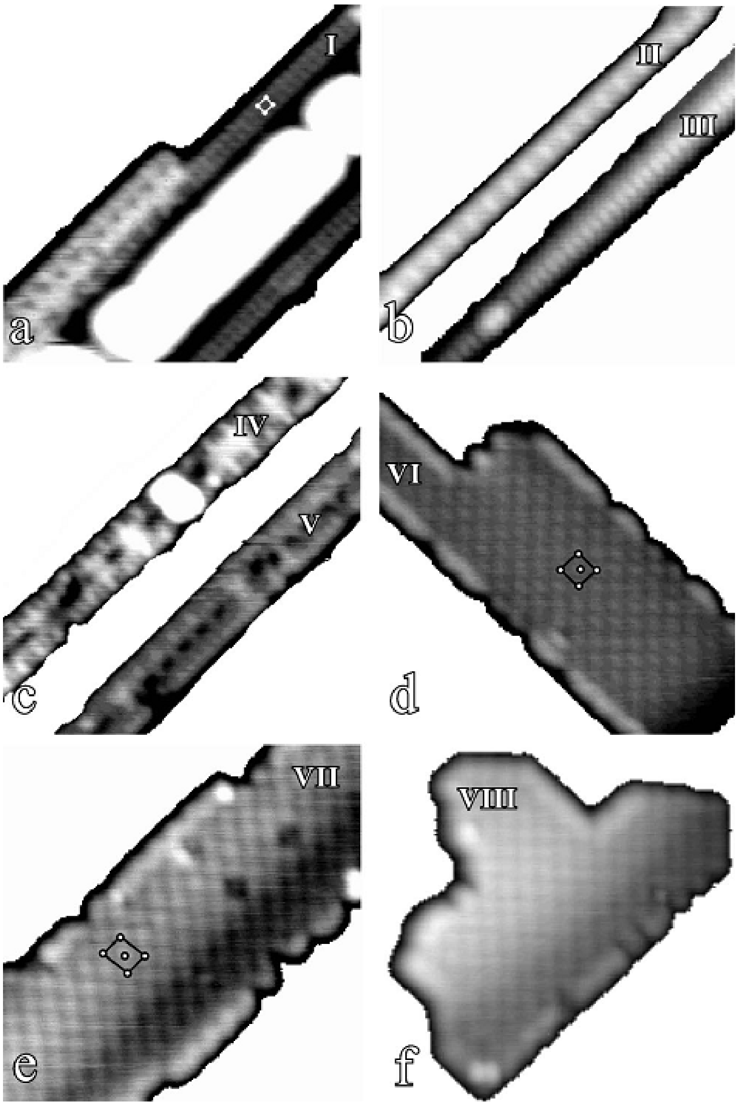

Figure 2.9: A figure from Liu et. al.'s [19] paper showing the surface reconstructions of various rare earth silicide nanostructures, all images have dimensions 10×10nm. (a) A p(1×1) reconstruction shown by the highlighted box which changes as the nanowire widens. (b-II) a nanowire with a surface periodicity of $2a_{Si}$, (b-III) surface periodicities of $1a_{Si}$ are possible but less common. (c) two nanowires with complicated surface reconstructions with periodicity $2a_{Si}$ for c-V but larger for c-IV. (d),(e) and (f) show larger structures with the common c(2×2) reconstructions, however in (e) and (f) the reconstruction is not square but rectangular.

Volmer-Weber (VM) growth

Volmer-Weber growth occurs when the deposited material does not form into a complete covering layer. Instead the material clumps together and forms islands. As more material is deposited these islands will increase in size and eventually encounter one another. This growth mode occurs when the adatom-adatom interaction is stronger than the adatom-substrate interaction. An example of this is gold on molybdenite [101] or germanium on silicon [102].

Frank-van der Merwe (FvdM) growth

This is the opposite of Volmer-Weber growth and is also known as ‘layer-by-layer growth’. In Frank-van de Merwe growth the deposited material forms a continuous film that completely covers the surface. As more material is deposited the film gets thicker without forming islands. This growth mode occurs when the adatoms preferentially bind to surface sites an example of this growth mode is gold on silver [103] .

Stranski-Krastanov (SK) growth

Stranski-Krastanov growth is neither Volmer-Weber or Frank-van der Merwe growth, it is a mix of the two. In Stranski-Krastanov growth the overlayer initially forms a complete covering film as in Frank-van der Merwe growth. However as more material is deposited this film becomes unstable and island growth occurs at some critical thickness. The critical thickness is highly dependent on the properties of the substrate and overlayer. An example of this growth mode is InAs on GaAs [104].

Ostwald Ripening

Ostwald Ripening is observed in many systems [105–107]. During annealing the smallest particles become unstable and lose surface atoms to the substrate which are then collected by the more stable larger particles. So during annealing the particle size distribution shifts, where the larger particles grow at the expense of the smallest.

2.4.1 Growth of Rare Earth Silicide Nanowires on Si(001)

Adatom Induced Surface Reconstructions on Si(001)

When rare earth metals are deposited onto the reconstructed Si(001) surface it has been found that the rare earth metal forms a ‘wetting layer’ in the form of new surface reconstructions prior to the formation of nanowires . Yang et. al. reported a surface reconstruction due to Er adatoms showing periodicities of c(4×2) and (2×3) where erbium atoms were replacing silicon atoms in dimers on the surface [108]. They argue that the c(4×2) is a precursor state to the more densely packed (2×3) and that the reconstructions can be considered precursors to nanowire formation, however the growth temperatures and times were not reported. Zhu et. al. also report the c(4×2) and (2×3) reconstructions along with the growth conditions. Their samples were grown by post deposition annealing of 0.5ML for 10min at 600° C, and their structure model for the (2×3) reconstruction is shown in Fig. 2.10(A)[20]. Other surface reconstructions have been observed for the RE/Si(001) system, Harrison et. al. reported an in depth study of the (2×7) and (2×8) [21] reconstructions observed for Gd on Si(001). An image from their paper [21] is shown in Fig. 2.10(B) showing a representation of the (2×7) and (2×8) surface reconstructions. However there is some uncertainty about the Er induced surface reconstructions as Chen et. al. [27] reported that they did not observe Er forming a wetting layer but found the Er forming a 1D chain on the surface at very low coverages. However the reconstructions reported by Yang et. al. [108] and Zhu et. al.[20] seem to dispute this. This implies that the system is described either by VM growth or SK growth with a very small critical thickness. However there is more evidence for the SK growth mode.

Strain Induced Growth

Chen et. al.[12] argued that the elongated shape of the DySi$_{2-x}$ nanostructures observed by Preinesberger et. al. [31] was induced by strain. Chen et. al. proposed that the uniaxial strain associated with the orientation relationship for hexagonal rare earth silicide given in Equ (2.5) was promoting growth along the direction of good lattice match and constraining growth along the direction of poor match, leading to highly anisotropic shapes. He supported his argument by reporting nanowire growth for four other rare earth silicides[109]. The argument that strain could direct the morphology of nanostructures grown via epitaxy was not new and we shall discuss an example of this later.

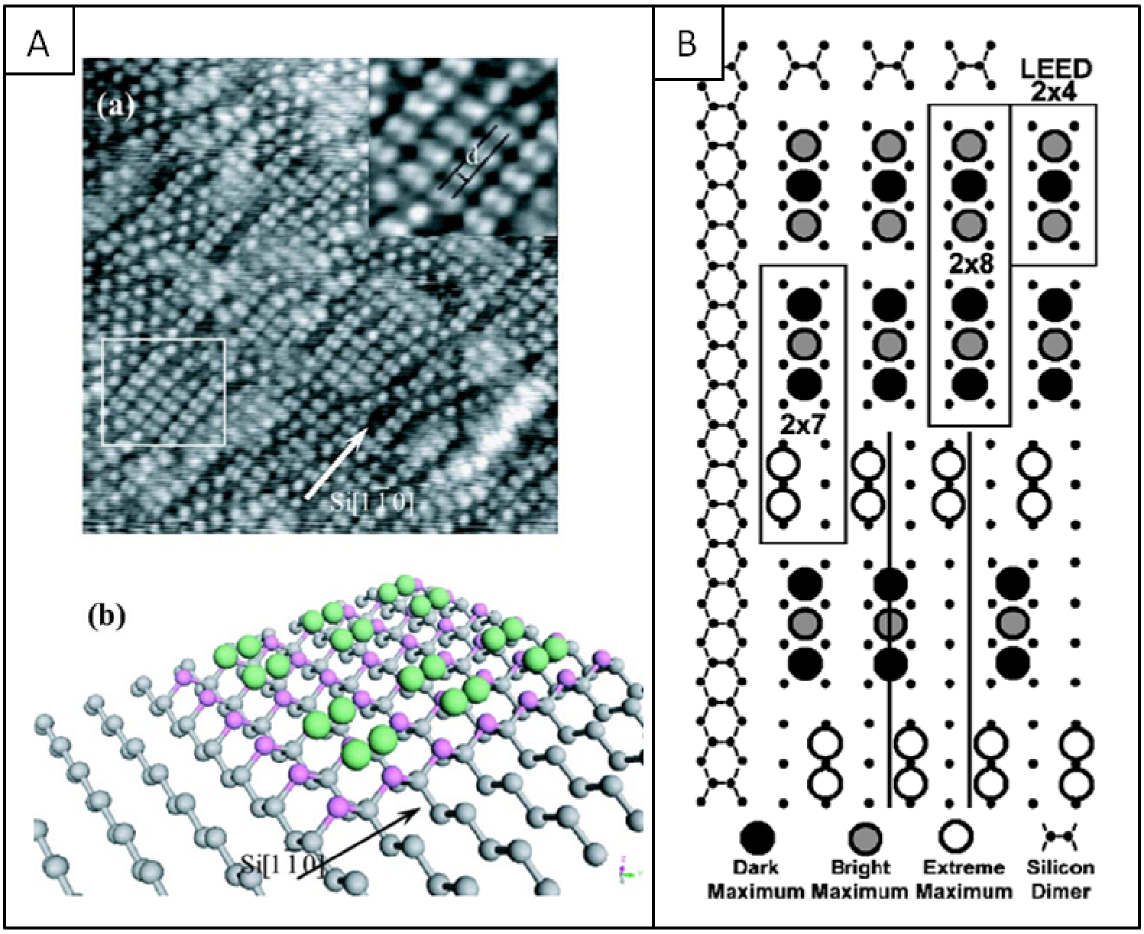

Figure 2.10: (A(a)) An STM scan showing erbium induced surface reconstructions on Si(001) (A(b)) The structure model proposed by Zhu et. al. for the Er induced surface reconstruction on Si(001) [20]. (B) Harrison et. al.'s [21] representation of the (2×7) and (2×8) surface reconstructions for Gd on Si(001).

The rare earth silicides do have alternate phases as previously mentioned. The alternate tetragonal phase for the rare earth silicides have a lattice mismatch that is identical in both directions, as shown in Equ (2.6). According to the strained growth model the tetragonal phase cannot be producing nanowire structures as we would expect equal growth in both directions. However this argument can only hold for structures that are 4 or more RE atoms high as the tetragonal unit cell is 4 RE atoms high, as it is unlikely that an incomplete unit cell would have 'bulk' lattice parameters, and at the 2 RE atom level the tetragonal structure is identical to hexagonal.

The strain values used for the strained growth model were taken from room temperature silicides. Yang et. al. argued that as the rare earth silicide is formed at high temperature the effect of thermal expansion on the lattice parameters must be taken into account, as the strain mismatch for room temperature silicides was unable to explain the aspect ratio differences between different rare earth nanostructures observed in STM. They measured the linear coefficient of thermal expansion for the rare earth silicides [22] and conclude that thermal expansion of the rare earth unit cell accounts for the difference in observed nanowire morphologies for different rare earth metals. The various strains associated with each of the hexagonal rare earth silicides at high and low temperature on Si(001) are displayed in Fig. 2.11.

Using the uniaxial strain theory we can postulate that all rare earth silicides that have a hexagonal phase will produce nanowires on Si(001) as they are chemically and physically similar. However there have been no nanowires observed for Tb and Lu silicides on Si(001) surfaces. The lack of nanowires for the Tb and Lu silicides on Si(001)combined with the published results of Eames et. al. [16], showing that the lowest energy structure on the reconstructed Si(001) surface does not conform to the stained growth model, presents a case that the strained growth model is incomplete.

There have been many studies into the growth of the rare earth silicide nanostructures on Si(001), and it has been found that the morphology of the grown nanostructures depends heavily on the growth conditions [20, 93, 109, 110]. The effect of the changes in the growth conditions on the nanowires has been investigated via scanning tunneling microscopy (STM)[20, 93, 109, 110] and high resolution transmission electron microscopy (HRTEM)[17, 26, 97], and it was found that in general, post deposition annealing or depositing more material leads to larger, wider features[20]. This behavior was described in terms of Ostwald ripening of the nanowires [20]. The final state of the system for long

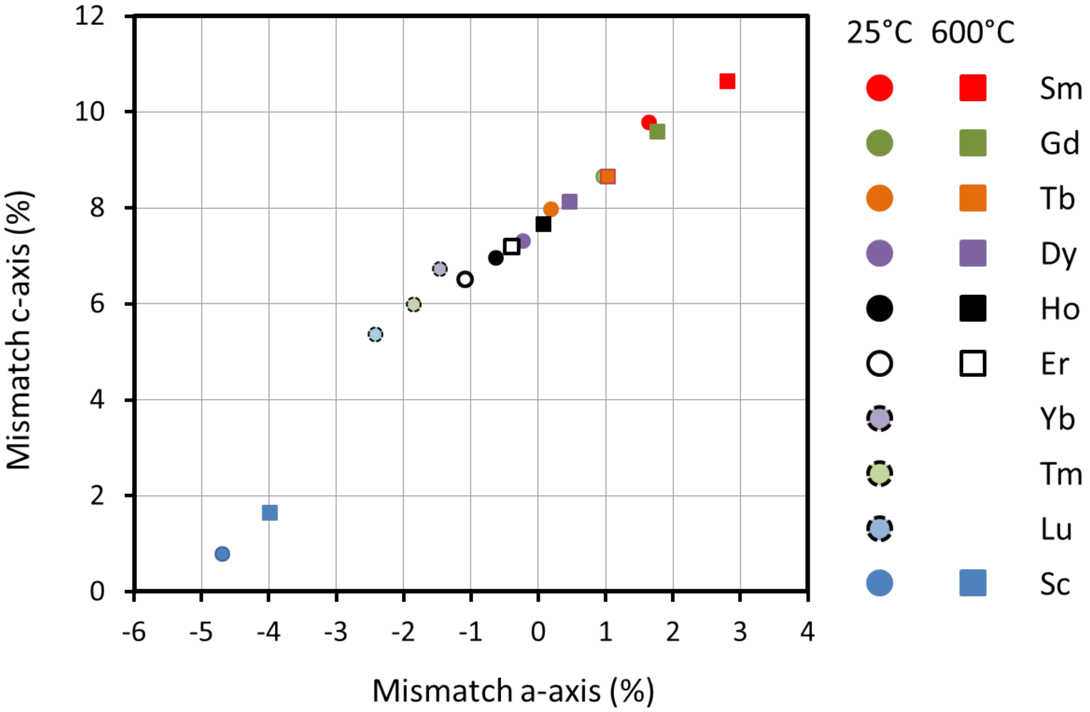

Figure 2.11: The lattice mismatches for the hexagonal rare earth silicides. The circular points show the lattice mismatches as reported my Maex et. al. for bulk silicides at room temperature (25°C) [3] (with the exception of Sm which was reported elsewhere [22]), where the square points indicate the lattice mismatches at high temperature (600° C)[22].

hot annealing was found to be large square islands of tetragonal silicide, implying that the hexagonal nanowires are metastable [110].

2.4.2 Similar Systems

The rare earth silicides are by no means the only example of strained growth of nanowires on the Si(001) surface. Bismuth nanolines have been investigated as a nanowire system on the Si(001) surface [30, 40, 111], and InAs/GaAs quantum dots have been well characterized as a strained growth system [112, 113].

Bi nanoline

Bismuth nanolines were first observed by Naitoh et. al. [111] in 1997 when bismuth was deposited onto silicon (001) at elevated temperature and imaged in STM. They appear to be similar to the rare earth nanowires in the fact that that they grow along the Si[110] and Si[$1\bar{1}0$] directions on the Si(001) crystal face. The Bi nanolines have been shown to originate from a surface reconstruction to form long one dimensional chains on the surface and are not formed via a uniaxial strain mechanism. These nanolines are resilient to annealing, maintaining their aspect ratio even for long anneal times, unlike the rare earth silicide nanowires; however the nanolines are semiconducting and not metallic.

InAs/GaAs

The concept of strain induced growth is not new. It had been known for a long time that strain could form nanostructures. In the InAs/GaAs system the InAs overlayer matches poorly to the substrate in both orthogonal directions and therefore forms nanodots due to the strain. The strain relief mechanisms have been well investigated and have been found to greatly reduce the performance of the nanostructures in devices. Threading dislocations within the GaAs substrate and lattice misfit dislocations in the InAs overlayer were thought to be the main strain relief mechanism however recent studies have found that as threading dislocations begin to appear for the largest nanodots the dislocations affect the migration of In atoms [112], allowing the remaining quantum dots to relieve strain by intermixing at the interface rather than by forming dislocations.

2.4.3 The Effect of Si(001) Surface Reconstructions

It has long been thought that the (2×1) surface reconstruction of the Si(001) plays a critical role in the formation of the rare earth silicide nanowires [28, 31, 114]. This is because the growth direction of the nanowires has been shown to rotate by 90° depending on which terrace the nanowire forms on. The surface reconstruction on the Si(001) which is shown in Fig. 2.12 face rotates by 90° on each adjacent terrace, implying that the dimer row direction has some effect on the nucleation and growth direction of the nanowires. The exact nature of the effect that the dimer reconstruction has on the nanowire formation and growth is not known.

Ramirez et. al.[115] showed that on the dimerized Si(001) surface, diffusion of rare earth metal atoms is much faster through the valleys created by the dimer rows, and Eames et. al's work shows that the energy of the nanowire is dependent on its relative orientation with the dimer rows. However it is not known if the (2×1) reconstruction survives during the growth process as RE induced surface reconstructions have been observed [20, 21] and could play a crucial role in the nucleation of these structures.

If the dimer row reconstruction does not survive during the growth of the nanowires the growth direction of the nanowires could be being influenced by the covalent bonding direction of the underlying silicon atoms.

Vicinal Si(001)

Early publications used flat Si(001) surfaces when growing nanowires, however it was shown by Regan et. al. [116] in 2003 that it was possible to encourage the nanowires to grow in one direction by using vicinal Si that an intentional misscut towards the $[1\bar{1}0]$ direction. It had been shown by Swartzentruber et. al. [117] in 1993 that this intentional miscut encourages the silicon surface to form double steps at the terrace edges rather than single steps. At a miscut angle of $\sim 4°$ towards the $[1\bar{1}0]$ direction almost all the steps are double steps. This removes one of the two equivalent $< 110 >$ directions formed from the dimer reconstruction on the silicon surface as each step will be between two areas of similar dimer row orientation, hence encouraging all the nanowires to grow in one direction. This means that we are able to perform TEM analysis with a known direction of extended growth allowing the association of the growth direction with an observed atomic

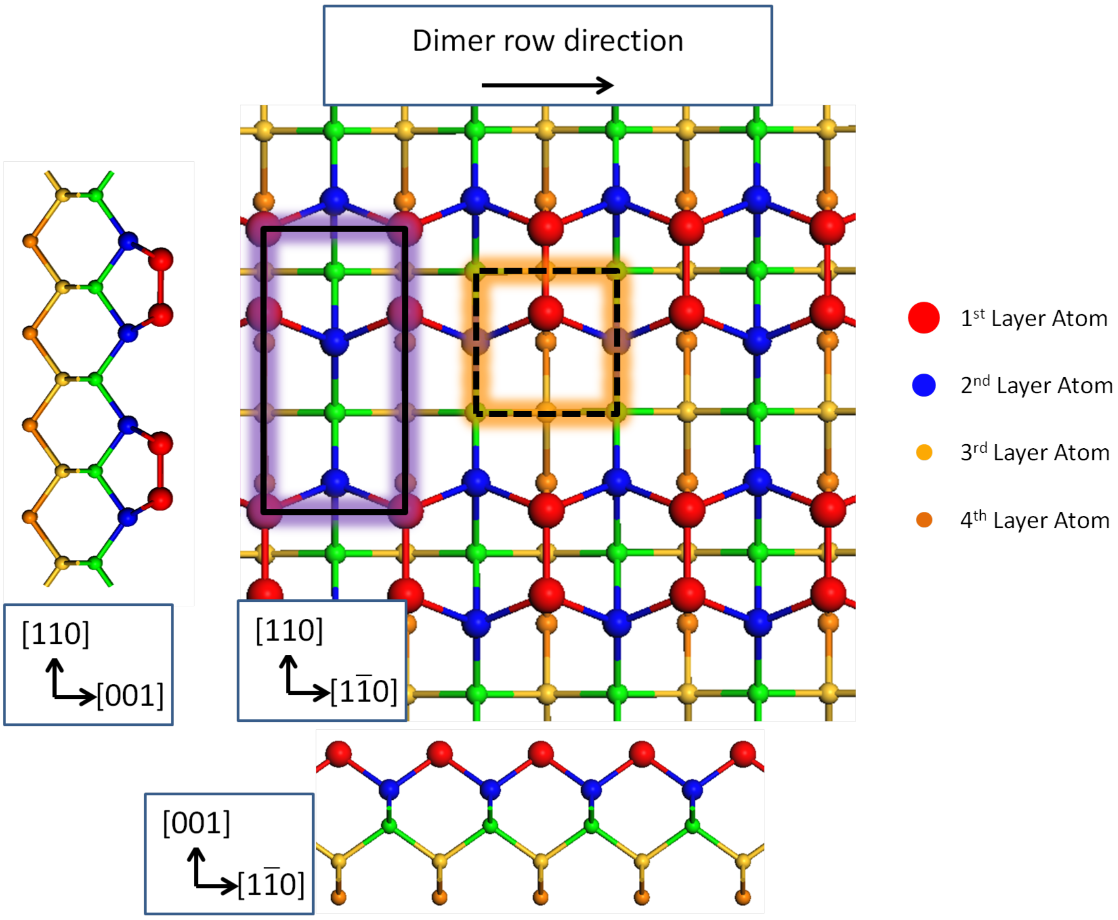

Figure 2.12: Three orthogonal projections of a generalized Si(001) surface, showing the dimerisation of the interfacial atoms. The red atoms are at the interface and have formed the ‘dimer’ reconstruction. In a bulk crystal the red atoms would occupy equivalent sites to the orange atoms (4^{th} Layer), however due to the dangling bonds the atoms have moved closer together and formed a bond. The pairs of atoms then tend to form into lines or dimer rows, as the formation of the dimer distorts the position of the substrate directly beneath it making dimerisation of the next pair easier. The larger purple highlighted box (solid line) indicates the periodicity of the surface reconstruction and the smaller orange highlighted box (dashed line) indicates the periodicity of the underlying substrate.

structure.

2.4.4 Other Silicon Surfaces

The main focus of the nanowire work has been on the Si(001) surface, however there have been studies where nanowires have been grown on other Si faces and these shall be discussed briefly.

Si(110)

It was shown that it was possible to grow $DySi_{2-x}$ nanowires on Si(110) by He et. al. [118]. These nanowires do not form due to uniaxial strain but due to the twofold symmetry of the surface. Katayama reported similar nanowires for the $ErSi_{2-x}$ system [119]. This technique was employed by Hong et. al. to produce highly ordered arrays of similarly sized Gd nanostructures in a massively parallel structure over mesoscopic areas [120].

Vicinal Si(111) or Si(557)/Si(5 5 12)

Growth of nanowires on the vicinal Si(111) surface was first demonstrated by McChesney et. al.[121] in 2002. The method of producing nanowires along step edges had been proven before with Au in 1997 [122]. Wanke et. al.[123] showed that it was possible to produce a variety of structurally and electronically different types of nanowire using this method by varying the amount of material deposited onto the surface, and therefore controlling the size of the nanowires.

2.5 Properties of Rare Earth Silicides on Silicon

2.5.1 Electronic Properties

Studies of the electronic structure of the erbium silicide system by Duboz et. al. [43] have shown the silicide to be metallic with a room temperature resistivity of $34\mu\Omega$cm ($3.4\times10^{-5}\Omega$cm). As low resistivities are desirable in electronics, this opened up many different possible applications of this structure. Ma et. al.[96] calculated the total density of states for the erbium silicide system while treating the 4f electrons as valence. They found that it is necessary to include the 4f electrons in their calculations in order to obtain a good fit with experiment, implying that substituting yttrium which has no 4f electrons for lanthanide metals may not be valid.

Tu et. al. [124] showed that the rare earth silicides have extremely low Schottky barriers of ∼0.4eV on n-type silicon for the as deposited silicide. This value can be made even lower, Duboz et. al. [43] showed by thermal annealing of the sample the barrier height is brought down to 0.28eV. More recent measurements put the lower bound on the Schottky barrier at ∼0.3eV [125]. The fact that annealing can alter the Schottky barrier so drastically implies that the anneal is having some effect on the interface structure, as the interface can have a strong effect on the Schottky barrier in similar metal silicide systems[126].

2.5.2 Low Dimensional Effects

The smallest nanowires have been shown to exhibit some unusual 1D phenomena, making the smallest nanowires interesting to study from a fundamental physics point of view. As an example Zeng et. al.[13] observed a variation in brightness along an ultra-small nanowire in an STM scan, and were able to show through modeling that this could be attributed to charge ordering within the nanowire, highlighting the 1D nature of the smallest structures. Another phenomena was observed by Rugeramigabo et. al.[45]. They took LEED and EELS measurements of the nanowires and observed that the smallest nanowires are likely to be semiconducting rather than metallic. This in itself presents an interesting possibility of altering the metallicity of the nanowires through controlling the width, or even forming metal/semiconductor interfaces within one nanowire. The main result of their paper was that the plasmon resonances that they observed in their EELS data for the small but metallic nanowires were found to be dispersing only along the wires. The energy of the plasmons is in the IR region, so this result opens the possibility of using this system in IR polarizers.

2.5.3 Reactivity

The rare earth silicide nanowires have been a very challenging system for TEM analysis as the nanowires are extremely reactive with oxygen. So when the nanowires are removed from UHV for analysis the smallest nanowires are quickly consumed by an oxide layer making analysis impossible. Attempts have been made to cap the samples with titanium [26, 35], CaF_2 [97], amorphous silicon [127], gold [98] and tungsten [128], with varying degrees of success, however the majority of TEM data is from larger islands, with the exception of He's paper [26]. He et. al. successfully capped nanowires in Ti and were able to analyse smaller nanowires in TEM. They reported that the nanowires they observed were growing with 'faulted surface layers', so that the nanowires were growing coherently in the expected hexagonal orientation and formed a tetragonal like defect at the surface to relieve strain.

2.6 Summary

The growth of rare earth silicide nanowires has been attributed to uniaxial strain within the rare earth silicide overlayer. The structure of larger nanowires and islands has been obtained experimentally and found to be consistent with the strained growth model, with the nanostructures being hexagonal with their c-axis perpendicular to the direction of extended growth. However no experimental measurements of the smallest nanowires have been achieved, so all models and DFT calculations begin with the assumed structure from the strained growth model. The strained growth model uses lattice parameters from bulk samples and it is not known if this assumption that the lattice parameters are similar is valid for features that are smaller than, or of the order of, the unit cells of the bulk materials.

The strained growth model is unable to explain why the growth direction of the nanowires seems to be dependent on the direction of the dimer row surface reconstruction on the Si(001) surface. Calculations by Eames et. al. suggest that on the clean dimerised silicon surface the tetragonal structure is lower in energy than the hexagonal regardless of the local direction of the dimer rows. The tetragonal model that was used in the calculations, can be modeled as a hexagonal silicide with its c-axis parallel to the extended growth direction. This result directly contradicts the accepted strained growth model and is supported by the observation that the preferred surface reconstruction of the nanostructures observed in STM agrees with Eames' model.

Chapter 3

Experimental Techniques

This chapter introduces the equipment and techniques that will be used in this study, from the growth of the samples through to characterisation and data analysis. The chapter aims to give enough information for the reader to understand the choice of techniques used in this study, the benefits and issues associated with the techniques and to be able to understand and interpret the results presented from each technique.

Aberration Corrected Scanning Transmission Electron Microscopy (AC-STEM) shall be discussed in great detail as STEM is the main technique used in this work and the vast majority of the results were obtained using this method. Scanning Tunneling Microscopy shall also be discussed even though only very limited data shall be presented from this work using this technique, as a working understanding of the technique will be necessary to interpret referenced data.

3.1 Sample Growth and TEM Preparation

During this study the samples were grown ‘in-house’ which gave us great control over the samples that we were able to produce and the procedures used for the growth. Having control over the growth allows the improvement of the procedure through an iterative process of growth and examination. Here we shall detail the methods used for growth and the steps taken to ensure that the growth was as reproducible as possible.

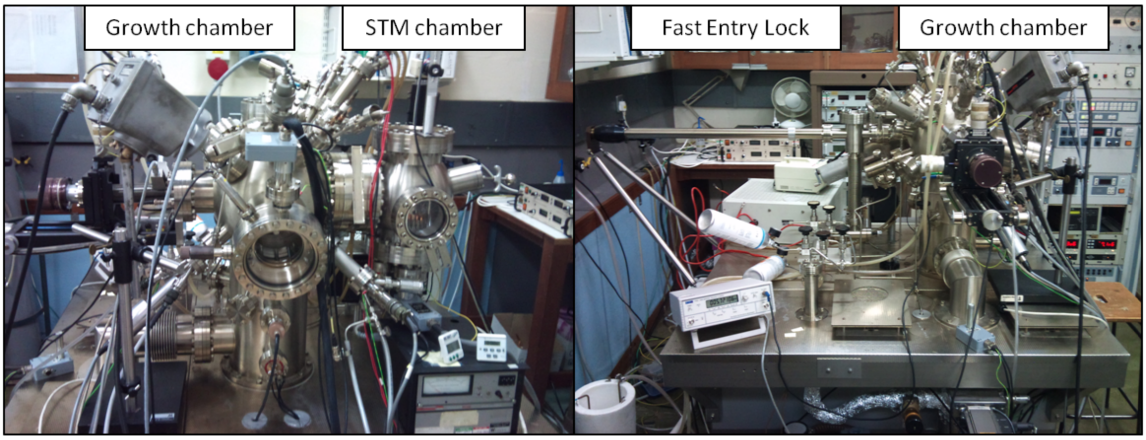

Figure 3.1: The growth chamber used for these experiments. The left shows the growth chamber and the STM chamber, where the right picture shows the growth chamber and fast entry lock.

3.1.1 The Growth Chamber

The UHV growth chamber that was used in this study was built by Omicron, it has two chambers, a growth chamber, originally designed as an analysis chamber with a Low Energy Electron Diffraction (LEED) system and an attached STM chamber that can be isolated from the growth chamber for 'in-situ' analysis. The system is shown from two angles in Fig. 3.1. The system is also capable of Auger electron spectroscopy but it has not been used in this study. In the STM chamber there is a storage carousel for 8 sample plates meaning that samples stored can be isolated via the gate valve from the main chamber during deposition or outgassing, keeping them clean. The growth chamber has a fast entry lock attached to one side allowing sample plates to be introduced to the system without breaking the vacuum in the main chamber. The manipulator is capable of heating samples via DC heating or e-beam heating, as well as cooling to LN_2 temperatures. There are 8 ports for sources however one of the ports is used by a quad pocket source meaning there is space for 11 different materials on the system at one time.

Vacuum Conditions

The vacuum system is maintained by two ion pumps and a Titanium Sublimation Pump (TSP) to a base pressure of around 1×10^{-10}mbar, however the base pressure can be as low as 1×10^{-11}mbar depending on the system cleanliness and leakage rates. After venting the system to atmosphere for any repairs or alterations the system is baked at ~130°C to outgas the chamber walls for two days. Before any samples are grown after the chamber pressure has recovered the sources are outgassed in two stages, first at a lower temperature without water cooling to outgas the shrouds. Once the source has cooled back down to room temperature the water cooling is reconnected and the source is slowly heated up to deposition temperature to outgas the deposition material.

The fast entry lock on the system enables the chamber to operate for ∼6 months without venting.

Sources

During the course of these experiments more than one type of source was used to deposit material onto the silicon substrate.

Ta Boat: These sources were designed and built within the department and were used to deposit erbium. A tantalum boat is bolted onto two copper pins through which a current of up to ∼25A can be passed through the Ta boat. The material to be deposited is held within the boat and is heated via the current. Due to the design of the holders, this method can only work for materials that sublime and have a vapour pressure in vacuum at temperatures lower than tantalum. The Ta boat is surrounded by a copper shroud which prevents material being deposited throughout the chamber, and, through the use of an aperture, collimates the material beam. The shroud is water cooled to prevent it heating and outgassing during deposition.

Filament: This method was used to deposit titanium. We were able to deposit Ti by replacing the Ta boat with a TSP filament and heating with an AC current of ∼45A. However this method was found to be unreliable as the filament would burn out before any substantial covering of Ti was achieved.

e-beam: An Omicron EFM3 electron beam source was used to heat the deposition material. This method was used to deposit silicon which is unsuitable for deposition using the Ta boat. A bar of silicon was heated at one end via an electron beam. The silicon only achieves a suitable vapour pressure when a molten droplet is formed, so heating must be carefully controlled to prevent the silicon droplet getting too large and falling to form a contact between the silicon rod and the shroud. This shorts the accelerating voltage circuit breaking the source; hence only slow deposition rates of silicon can be achieved with this method.

Temperature measurements

The temperatures within the growth chamber were measured using an IS50 Si-LO plus infra red pyrometer calibrated to an emissivity of 0.7 for silicon. The pyrometer has a built in laser allowing easy alignment and focusing onto the sample through a port window ensuring that only the sample temperature is being measured, leading to more accurate measurements during outgassing and growth.

Growth Rate Calibration

The deposition rates of the sources were calibrated prior to deposition using a 6MHz quartz microbalance. The quartz microbalance was measured by a Labview VI which logs the frequency over time and is capable of correcting for background drift, which is essential for low growth rates.

3.1.2 In-Situ Capabilities

Low Energy Electron Diffraction

For early samples the Si(001) surface was characterized by LEED, using an Omicron LEED gun and optics system. The characterisation was performed after cleaning to ensure that the surface was well ordered. It was found that the preparation technique reliably produced good quality surfaces. It was found during other preliminary experiments that the growth of the nanowires can be greatly affected by surface contamination. Outgassing of the the electron gun and carbon cracking from the electron beam used in LEED can deposit small amounts of carbon onto the surface, so in order to limit the contamination of the surface, this step was omitted in later samples.

Scanning Tunneling Microscopy

STM measurements from an Omicron room temperature STM/AFM were taken to observe the morphologies of the nanowires post growth on some samples. STM was used to check for the presence of nanowires especially after the chamber had been vented for maintenance to ensure that the growth of the nanowires was occurring as expected.

3.1.3 TEM Sample Preparation

The samples were prepared for cross sectional Transmission Electron Microscopy (TEM) using a variant of the 'tripod polishing technique' [129]. The details of the procedure are described in Appendix A.

A schematic of the main steps of our preparation method are shown in Fig. 3.2, this results in samples similar to the one shown in Fig. 3.3. Fig. 3.2 shows a sample being prepared that will result in images viewed parallel the direction of extended growth of the nanowire. The vast majority of the samples prepared were prepared in this orientation. There were a limited number of samples prepared that resulted in images that are viewed perpendicular to the direction of extended growth of the nanowire the difference between the orientations is shown in Fig. 3.4. It should be noted that Fig. 3.2 does not show the capping step that would occur after point (b) and before the sample was taken out of the growth chamber for point (c).

When preparing samples it was the procedure to aim for a failure ratio of 1:3. As the operator gets more experienced at sample preparation and the number of failures drops it is possible to aim to produce thinner samples, which results in a higher failure ratio. By aiming to keep this ratio a constant the number of samples produced remains at a suitable level while always aiming to produce better quality samples.

In later samples we also experimented with only having the silicon overlayer. The omission of the under layer allows the sample to be rotated 180° when glued onto the Mo half-ring so that the interface edge is towards the center of the ring. This means that the critical thin area is protected by the half ring and the backing silicon, with the added benefit that during ion polishing there is no shadowing of the interface from the half-ring when milling from the 'back', leading to shorter ion milling times. Fig. A.1 shows the two arrangements of the half ring with the silicon.

3.2 Surface Sensitive Techniques

The techniques described here have not been used in any great capacity in this work, however the discussion of previous work and the discussion of the results in the context of previous work will require a working understanding of the principles of these techniques.

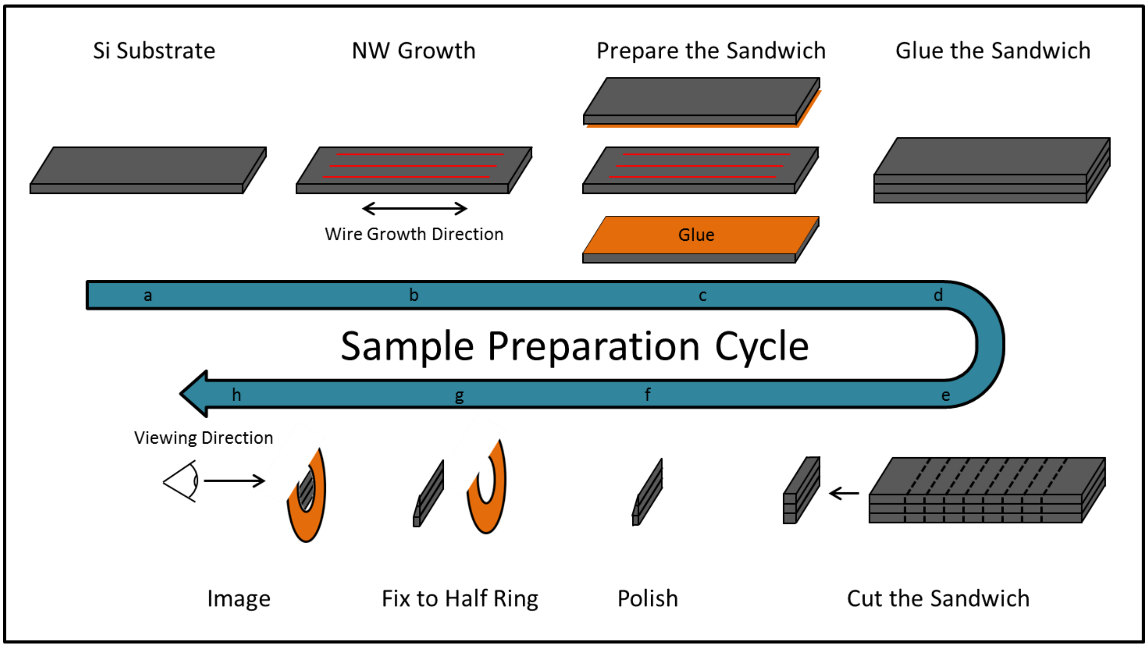

Figure 3.2: A schematic showing the main features of preparation method and how the sample progresses from one stage to the next. (a) A chip of silicon is cut to act as a substrate during deposition. (b) Nanowires are grown on the substrate. (c)&(d) The silicon chip is sandwiched between two others and glued in place. (e) The sandwich is sawn to produce smaller cuts. (f) The cuts are polished to thin them to electron transparency. (g) The thinned samples are fixed to half rings. (h) The individual samples are imaged.

3.2.1 Scanning Tunneling Microscopy

Scanning tunneling microscopy (STM) was developed by Binnig et. al. [130] in 1982. It involves scanning an atomically fine probe across the sample surface, with an applied bias voltage between the surface and the tip, and measuring the tunneling current between the surface and the tip. A positive bias is defined as the surface having a positive surface potential with respect to the tip. As the tip gets closer to the surface the tunneling current will exponentially increase [131], and vice versa when the tip gets further away the current will decrease. By measuring the tunneling current a feedback loop can be generated in order to keep the tunneling current constant. A generalized schematic of the STM system is shown in Fig. 3.5.

In general the STM is used to build up an image of the surface in one of two ways, either the tip to sample distance is varied in order to keep the tunneling current constant, where the tip follows contours of constant charge density, and the Z position of the sample measured (constant current mode) or the tip to sample separation is held constant and the tunneling current measured (constant height mode). In general the STM is operated

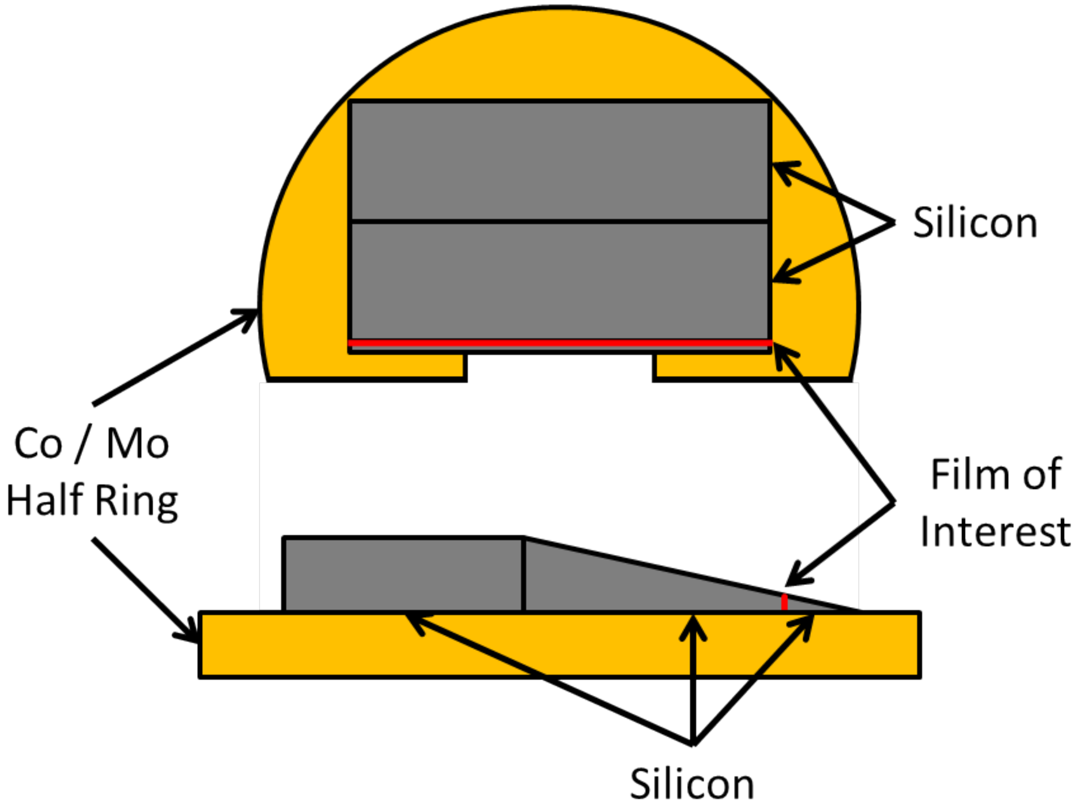

Figure 3.3: A schematic of the arrangement of the majority of the TEM samples used in this study. Some samples were produced that resulted in having the film of interest towards the center of the half ring.

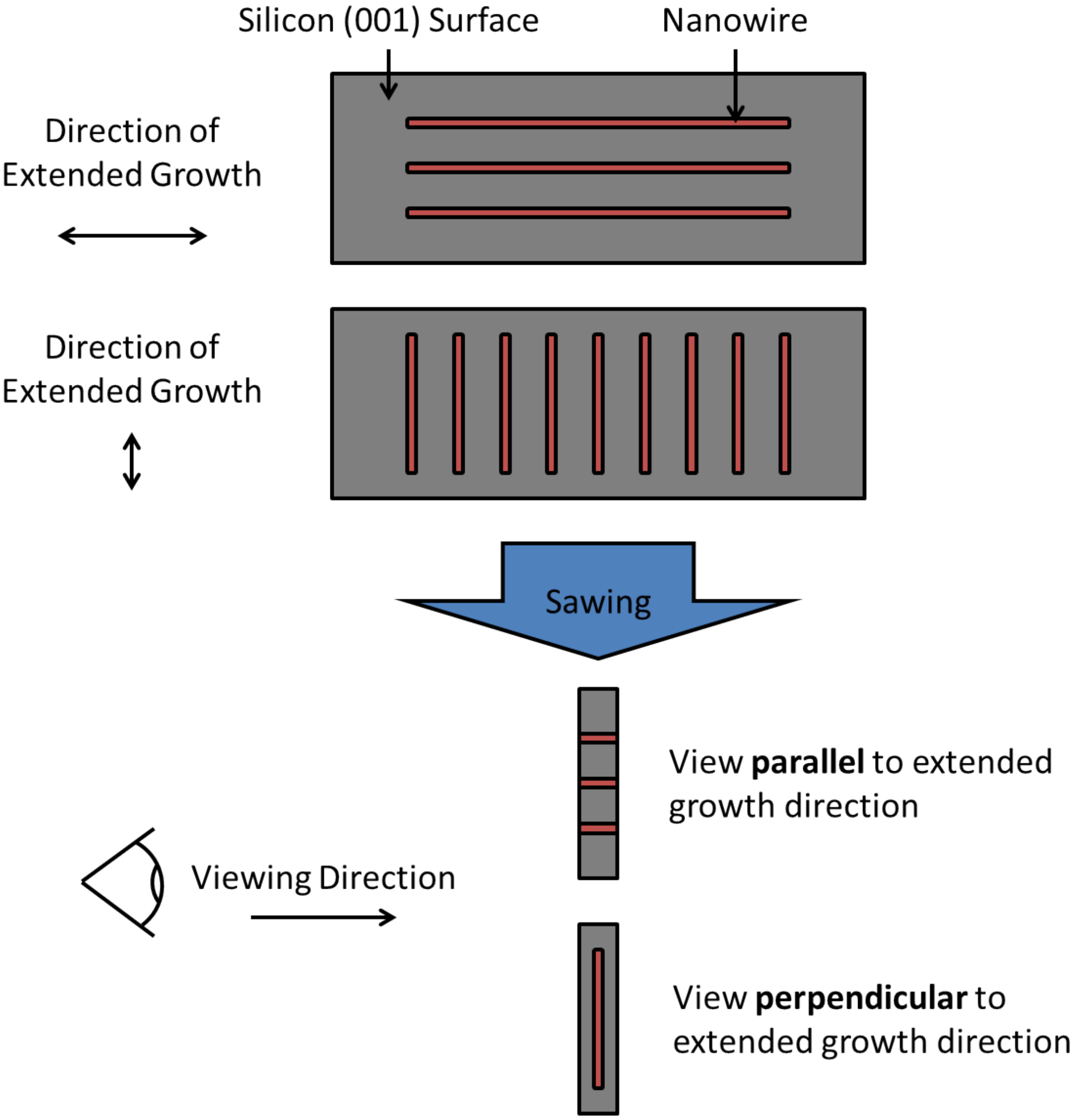

Figure 3.4: A schematic showing the different geometries of the two sample orientations used in this study, parallel to the direction of extended growth and perpendicular to the direction of extended growth.

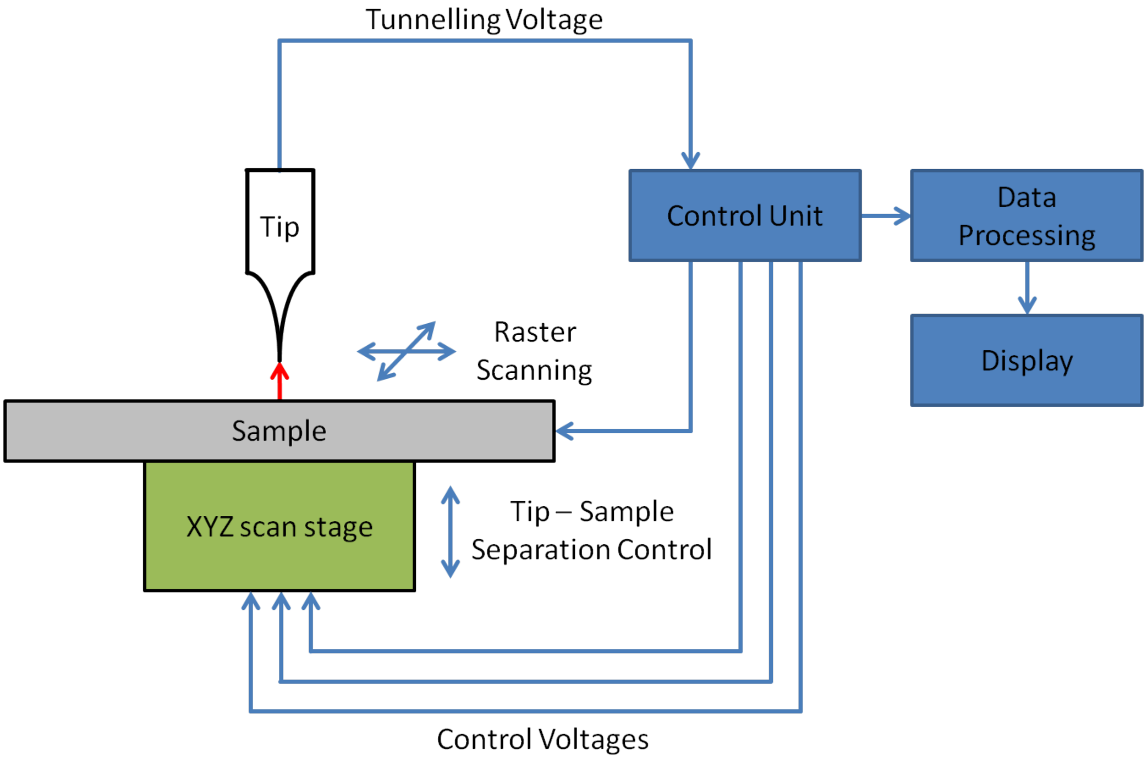

Figure 3.5: A schematic of an STM. In this design the tip is stationary and the sample is scanned to produce images. A voltage is applied between the tip and the sample and a tunelling current is generated. This current is measured by the control unit which controls the scan stage and in constant current mode moves the sample to keep the current constant. The XYZ data is then used to produce an image. In constant height mode the tip-sample separation is not included in the feedback, as the tip scans over the sample the tunneling current varies and is used to produce an image.

in constant current mode as it is much less risky. In constant height mode there is no feedback to stop the tip crashing into the surface and potentially ruining the tip.

By scanning the tip over the sample a tip height-position image or a current-position image can be obtained. The STM has the resolution and sensitivity to be able to resolve individual atoms on a surface making it an extremely powerful tool in surface characterisation. However as the mechanism that is used to observe the surfaces is a tunneling current there are some issues with this technique.

One of the problems with the STM technique is that it does not produce topography images, but is built up from tunneling current measurements. The tunneling current is dependent on the tip to surface separation, however it is also dependent on the local density of states at the surface. If there is a local reduction in the number of available states for the electrons to tunnel into or out of that will appear as a reduction in the tunneling current and appear as a depression on the surface. As the local density of states is dependent on the atomic species and structure this can result in misleading images. This effect can be mitigated by averaging each atomic position over a number of tunneling voltages to sample many points in the density of states. The effect of local density of states giving false topography measurements is highlighted by STM measurements of graphene, where the graphene appears highly corrugated [131][132].

3.2.2 Low Energy Electron Diffraction

LEED is often performed in the growth chamber as an in-situ technique to characterize the surface periodicities of the samples to check the quality of the cleaned surfaces or the periodicity of the grown films. By firing a low energy electron beam (from 10-300eV [133]) at the surface some of these electrons will elastically backscatter from within the first few atomic layers of the sample and diffract off the first few atomic layers on the way back out. These electrons can be picked up on a phosphor screen and the diffraction pattern observed. The pattern of spots that results from LEED result from diffraction from the surface and immediately sub-surface layers, as electrons that travel a long way into the sample before being backscattered are likely to have lost energy through inelastic scattering. These electrons are then blocked from contributing to the final diffraction pattern by retarding grids in the electron optics. Thus the LEED pattern contains detailed information about surface reconstructions and surface quality.

By looking for extra spots between the major spots that result from the bulk structure the relative periodicity of a surface reconstruction can be found, where the sharpness of the spots in the pattern indicate the quality of the surface.

3.3 Transmission Electron Microscopy Based Techniques

3.3.1 General Background and Considerations

Electron Optics

In order to produce a focusing action on an electron beam magnetic lenses are needed. When a moving charge such as an electron encounters a static magnetic field it experiences a force described by the Lorentz equation (3.1):

$$\mathbf{F} = q_e(\mathbf{E} + \mathbf{v} \times \mathbf{B}) \tag{3.1}$$

Where **F** is the force, **E** is an electric field, **v** is the velocity of the electron and **B** is the magnetic field. In an electron microscope no static electric fields are used in the electron lenses so **E** = 0 and equation (3.1) simplifies to a cross product between the velocity and the applied magnetic field. If there was a perfect uniform field along the direction of travel of the electrons, the electrons would experience no force from that field as the $\mathbf{v} \times \mathbf{B}$ term is also zero. However in a magnetic lens the field bows outwards at the top and bottom of the lens producing a radial magnetic field component B_r. This radial magnetic field induces a velocity in the θ direction for the electrons V_θ. This V_θ velocity and the B_z magnetic field cause the focusing action of the magnetic lens as the electrons gain a V_r component and move towards the optical axis. Fig. 3.6 shows the polar coordinates used and the helical path of the electron within the lens. This process requires that the electron lens be symmetric in θ about the optic axis.

3.3.2 Aberrations

In optical microscopy the limiting factor for obtaining higher resolution images is the wavelength of the radiation used to form the image. In an electron microscope the limiting factor are the aberrations associated with the electron lenses. These aberrations come in many forms; however the most commonly encountered are are astigmatism, spherical

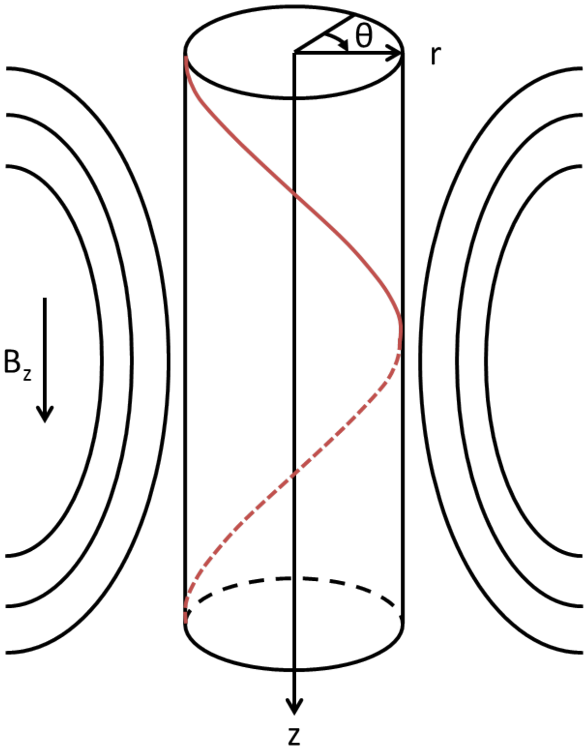

Figure 3.6: The helical path of the electrons induced by the magnetic field within the electron lenses

aberration and chromatic aberration. The basic ray diagrams for these aberrations are given in Fig. 3.7. Astigmatism occurs when the lens is asymmetric, i.e. the horizontal and vertical focal points of the lens are different and can be easily corrected. Spherical aberration occurs when the outside of the lens has a different focal point to the center of the lens, and is inherent in the design of electron lenses, it is also much harder to correct for. Scherzer proved in 1936 that it is impossible to create a spherically symmetric electron lens that has no spherical aberration [134]. To be able to correct for the inherent aberrations the spherical symmetry must be broken. In non aberration corrected microscopes the spherical aberration is the limiting factor of the resolution.

Aberration Correction

Due to the resolution of microscopes being limited by spherical aberrations a lot of effort was made to reduce or correct these aberrations. This can be achieved in a variety of ways, as an example, Rose's [23] solution is shown in Fig. 3.8(a) with a graphical representation of the ray paths in 3.8(b). This is achieved experimentally by measuring the aberrations in the whole microscope by reverse engineering them from a tilt series of images, then

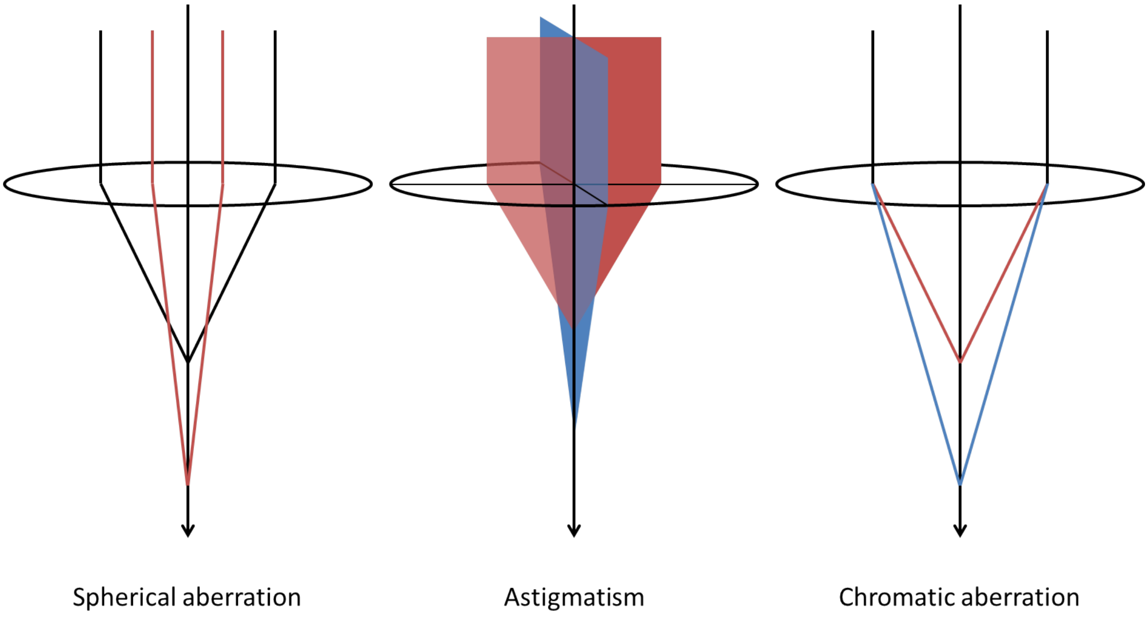

Spherical aberration

Astigmatism

Chromatic aberration

Figure 3.7: Spherical aberration: Rays further from the optical axis are focused at a different plane to those from the center of the lens. Astigmatism: Different planes have different foci. Chromatic aberration: Different wavelengths are focused to different planes.

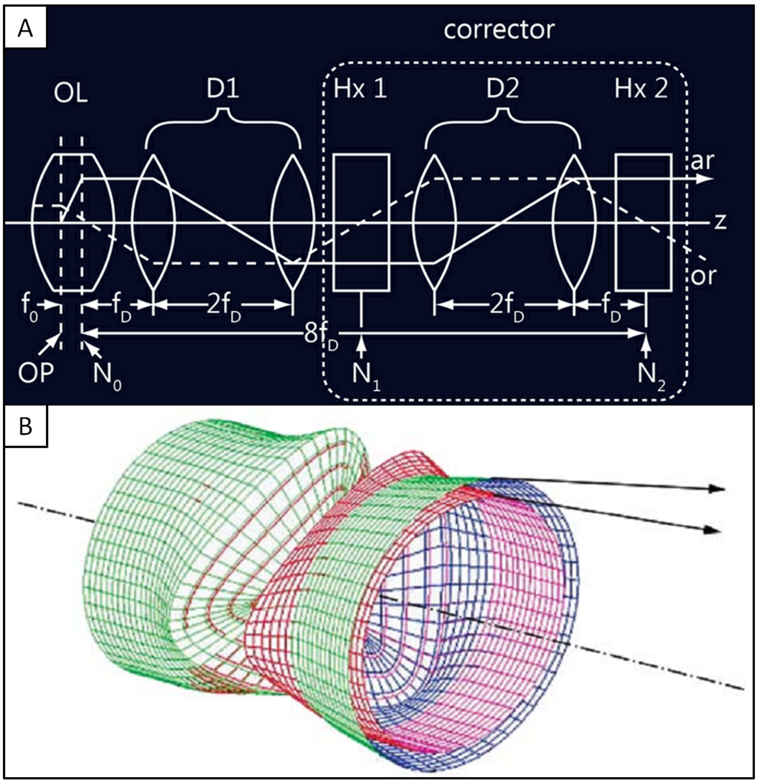

Figure 3.8: (a) Rose’s design for an aberration corrector [23]. (b)An image from an FEI publication [24] showing the breaking of the spherical symmetry using two hexapoles separated by a telecentric round lens couple.

applying the necessary magnetic corrections, and repeating the process. The use of an aberration corrector within an electron microscope greatly improves the possible resolution [25], it is possible to achieve sub angstrom resolution, however it can take days to align correctly.

3.3.3 Abbe Theory

In an electron microscope the sample is illuminated by a coherent beam, thus diffraction and interference must be considered when modeling image formation. E. Abbe solved this problem by postulating that the sample acts as a diffraction grating, coupled with the fact that the coherent illumination will diffract from the condenser aperture. Thus every point in the object, as well as every point within the aperture, must be considered when determining the complex disturbance at all points in the image plane. Abbe theory tackles this problem by modeling the lenses as a double Fourier transform of the object function. The object function is Fourier transformed to access the phase space, some ‘aperture’, ‘envelope’ and ‘aberration’ functions are then applied,then the resultant is Fourier transformed again to obtain the image.

The phase space representation of the object is the diffraction pattern, so Abbe theory tells us that we can access the diffraction pattern after the aperture, envelope and aberration functions have been applied. These functions act to remove the high frequency information from the diffraction pattern, so in general we are able to observe the low frequency spots of the diffraction pattern in the FFT of the image. How much of the diffraction pattern that we are able to observe in the FFT gives us information about the aperture, envelope and aberration functions that were applied by the imaging system. By looking at the high frequency cut-off in the FFT and the shape of the cut-off we can quickly obtain the resolution and astigmatism of the microscope.

3.3.4 HRTEM

Electron microscopy is a powerful tool that has been extensively used to characterize the rare earth silicide system [17]. The high resolving power available allows detailed examination of the structure of thin films, interfaces and nanostructures. Experimental results however have been hampered by oxidation of the rare earth silicide nanostructures [118] thus limiting the smallest size of nanowire that can be observed. Attempts have been made to cap the nanowires in many different materials such as titanium [26, 35], CaF_2 [97], amorphous silicon [127], amorphous carbon [135] and tungsten [128]. The basic setup of the TEM is shown in Fig. 3.9. The electron beam is manipulated by the condenser system to form broad parallel illumination for the sample. The objective lens system and projector lens system can form either an image or a diffraction pattern depending on the excitation of the projector lens.

HRTEM requires that the sample be very thin as the electron beam has to pass through the sample to be imaged, this condition can make preparation of HRTEM viewable samples quite challenging as a typical HRTEM sample will be $\leq$50 - 100nm; although in general thinner is better.

Contrast

At high magnification in a TEM the contrast that we observe is usually not related to mass or thickness. In order to describe the image we assume that the object has no effect on the amplitude of the wave illuminating it, but imparts some phase information onto it instead. This is the weak phase object approximation (WPOA). Thus intensity at the image plane in the WPOA is the square of the phase of the wave and contains no mass or thickness information.

Thus the variations in contrast in a HRTEM image are due to interference and cannot be directly interpreted as atomic structure.

Delocalization

Contrast delocalization means that at any given point within the image the contrast is not directly related to the corresponding point within the object, the contrast is constructed from the intensity from neighboring areas as well. In an aberration uncorrected microscope, or a poorly focused microscope, delocalization can have dramatic effects on the image, further complicating the contrast variations observed in the HRTEM image, especially at interfaces or boundaries.

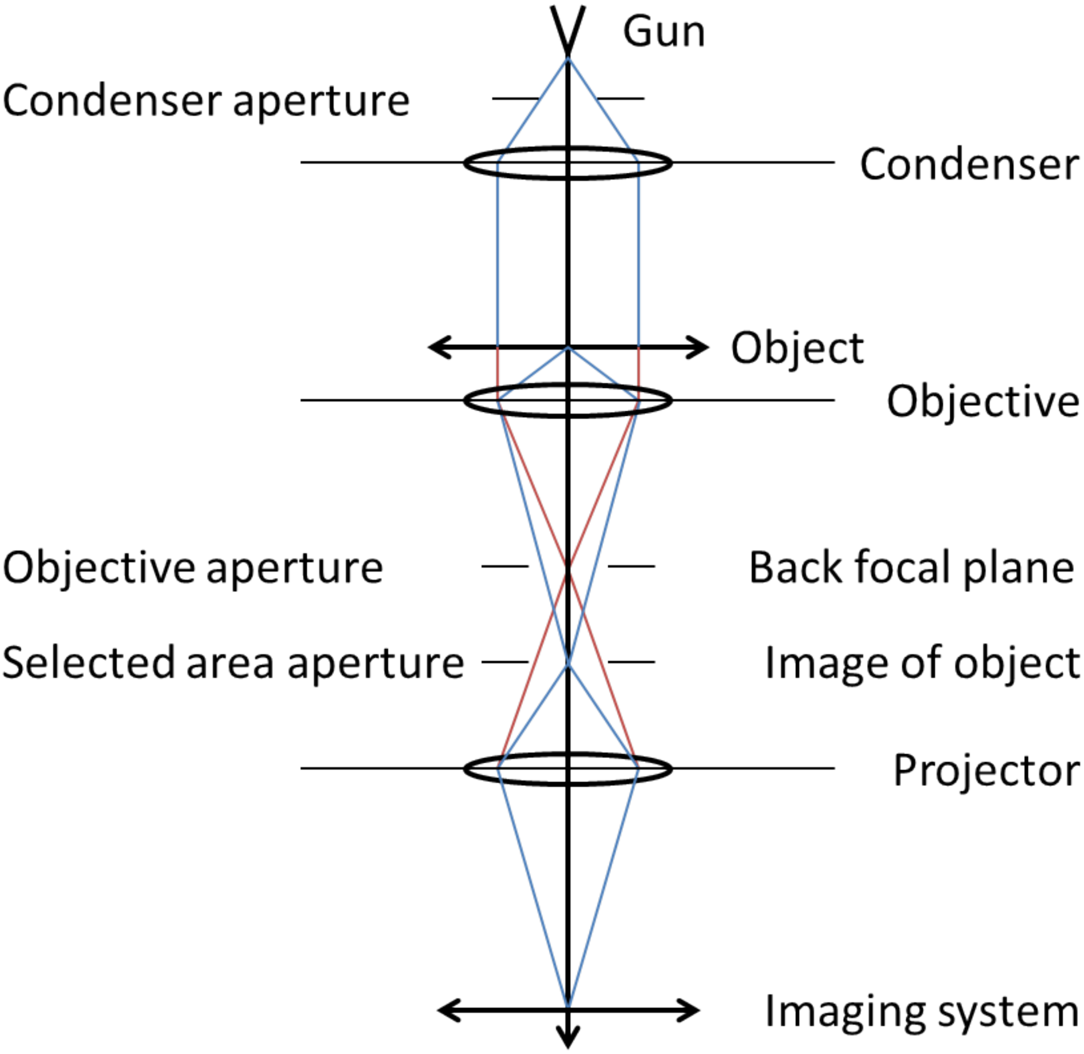

Figure 3.9: The basic set up for a transmission microscope. This general ray diagram can be extended to either optical or electron microscopy. In imaging mode the projector lens is focused onto the image plane of the objective lens and in diffraction mode is focused onto the back focal plane.

Diffraction and Fourier Transforms

A diffraction pattern from a selected area of the sample can give highly detailed information about the crystal structure that may not be obvious from the image itself. As Abbe theory tells us that a lens acts as a double Fourier transform to form an image, we can obtain similar information from a Fourier transform of an image as would be obtained from a diffraction pattern. However in general a FFT will give lower quality information as the image does not contain all the spatial frequencies that are apparent in a diffraction pattern. However we are able to more precisely place a FFT window so the spatial resolution can be improved over a diffraction pattern. By looking at the Fourier transform of the image in some cases we are able to get similar information that we would have obtained from the diffraction pattern.

Diffraction patterns and Fourier transforms can show relative rotations of crystals in the sample, changes in the lattice spacing and give information on vacancy structures that are not visible in the image. Geometric phase analysis uses a Fourier transform of an image to check for any local changes in the lattice spacing of the crystal in the image. The technique highlights areas of strain along defined axies.

The diffraction pattern displays spots corresponding to much higher spatial frequencies than the Fourier transform as the Fourier transform of the image is subject to the envelope functions that cut off high frequencies being expressed in the image.

3.3.5 STEM

Aberration corrected scanning transmission electron microscopy uses a focused electron beam, of typically $\sim$100pm [25], which is rastered across the sample. Usually this illumination mode is coupled with a dark field detector, an annular detector that has a hole to allow the straight through beam to pass through. This ensures that only electrons that are scattered at high angle are collected on the annular detector. As the scattering coefficient of electrons scales with atomic number, heavier atoms will produce more scattering and will appear brighter in the image. This effect can be used for quantitive analysis as the scattering intensity scales roughly $\sim$as Z^2 [136]. At each point on the sample the intensity of the electrons scattered at high angle is collected to form an image. This point by point data acquisition approach has a major drawback compared to HRTEM in that it takes

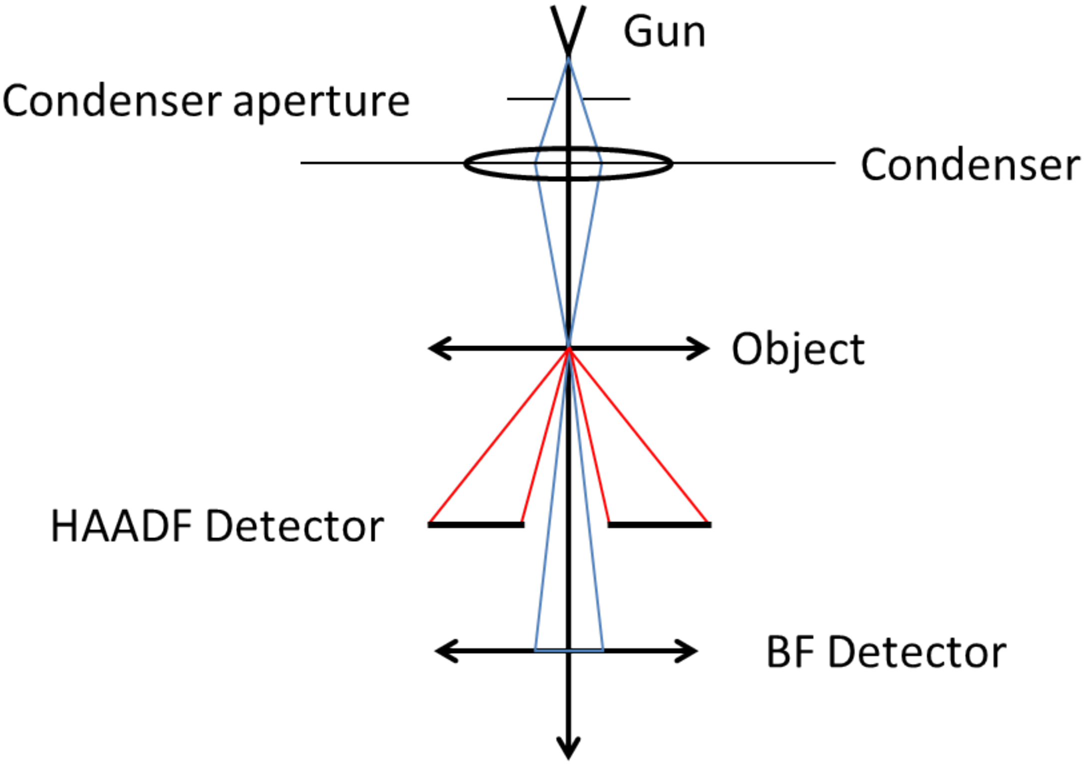

Figure 3.10: The basic setup of the STEM

much longer to collect high quality data, and drift often occurs during the scan process. However there are major benefits to this mode and drift can be reduced by allowing the microscope time to stabilise before acquiring an image.

The basic set up for the scanning transmission electron microscope is shown in Fig. 3.10. Two detectors are shown, the dark field HAADF detector and the bright field detector. Only data from the HAADF detector was used for this study.

In some cases beam sensitivity can be an issue as the illuminating electron beam is focused to such a small area it can be very intense which can damage or alter the structure of the sample during imaging. In extreme cases, with highly focused beams, its is possible to mill areas of the sample away.

Incoherent Imaging

Electrons that are scattered at high angle tend to be elastically scattered from the nucleus of atoms within the sample. In general these scattering events do not result in any coherence and therefore do not cause any interference effects at the image plane. Thus an image collected in this point by point incoherent manner can be directly interpreted as structure [136], eliminating the need to produce many calculated images to match to experimental through focal series to find a structure as would be the case in HRTEM.

Electron Channeling

Electron channeling occurs when the focused illumination beam is exactly aligned with an atomic column. The nuclear charges act as lenses, focusing the beam along the column. As the electron beam is guided along the column there is an effective increase in the density of electrons near the atomic nuclei within the sample. This results in more electrons being scattered at high angle and extra brightness in the image.

Sample Orientation

The electron channeling effect is highly dependent on the relative orientations of the sample and the electron beam. A small angle between the incident electrons and the atomic column is enough to break the electron channeling effect. So, when imaging a sample in STEM, sample orientation is extremely important to get high quality images.

Convergent Beam Electron Diffraction

Convergent beam electron diffraction (CBED) as the name suggests is electron diffraction using multiple incident angles made available using the convergent electron beam in the STEM. CBED is able to give much more information about the sample than standard diffraction due to the increased number of incident angles.

CBED patterns have been used to accurately obtain thickness measurements of samples within the microscope. This is achieved by simulating the CBED pattern as a function of thickness to find the pattern that best matches the experimentally obtained pattern.[137–139]

Kikuchi Lines

By observing the Kikuchi lines in the CBED we are able to accurately align the sample to the beam [140], as the Kikuchi lines form a ‘road map’ to the major symmetry directions.

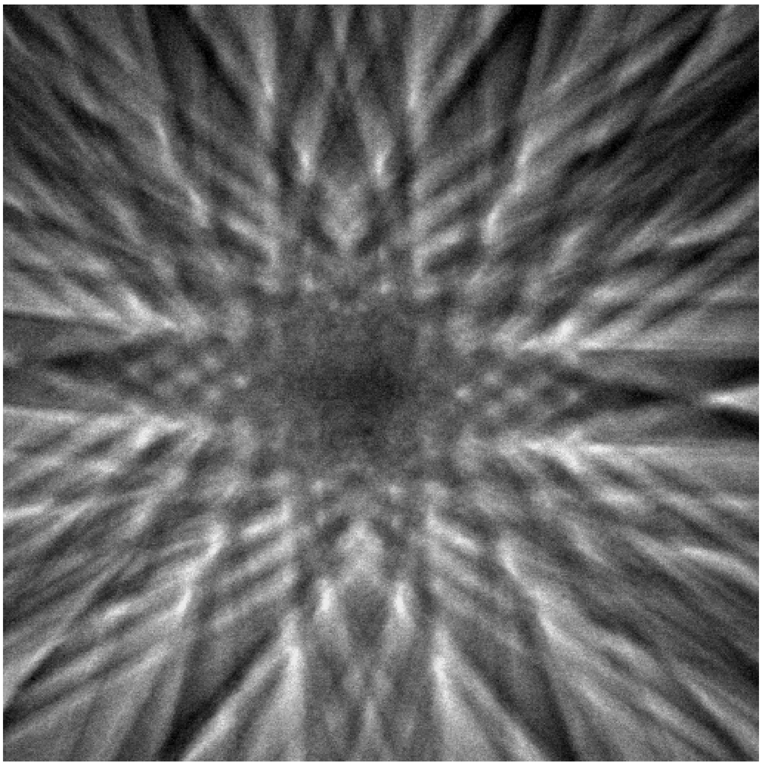

Figure 3.11: The Kikuchi lines present with a CBED pattern from a thick silicon sample viewed along the Si[110] direction. The conversion point of the lines at the centre of the image indicates a high symmetry direction, in this case the Si[110] direction, and is used to orientate samples for imaging.

An image of Kikuchi lines in a thick sample is shown in Fig. 3.11

Ronchigram

The Ronchigram is the shadow cast by the sample onto the image plane produced by convergent illuminating beam. It is extremely useful in aligning the STEM as it displays all of the aberrations within the microscope at the same time. A ray diagram showing how the spherical aberration can be observed in the Ronchigram is shown in Fig. 3.12. In a STEM that suffers from spherical aberration the rays that travel through the outer of the lens will be focused before the rays that travel through the center of the lens. By focusing the rays to a point, a virtual source is produced, and if this virtual source intercepts the sample this will form an image with infinite magnification. Fig. 3.12(A) shows a scenario where the central rays are focused below the sample, but the outer rays at some unspecified angle, are focused onto the sample due to the spherical aberration shortening the focal length, which will produce a ring image of infinite magnification surrounding an area of high magnification. Alternatively the scenario where the central rays are focused onto the

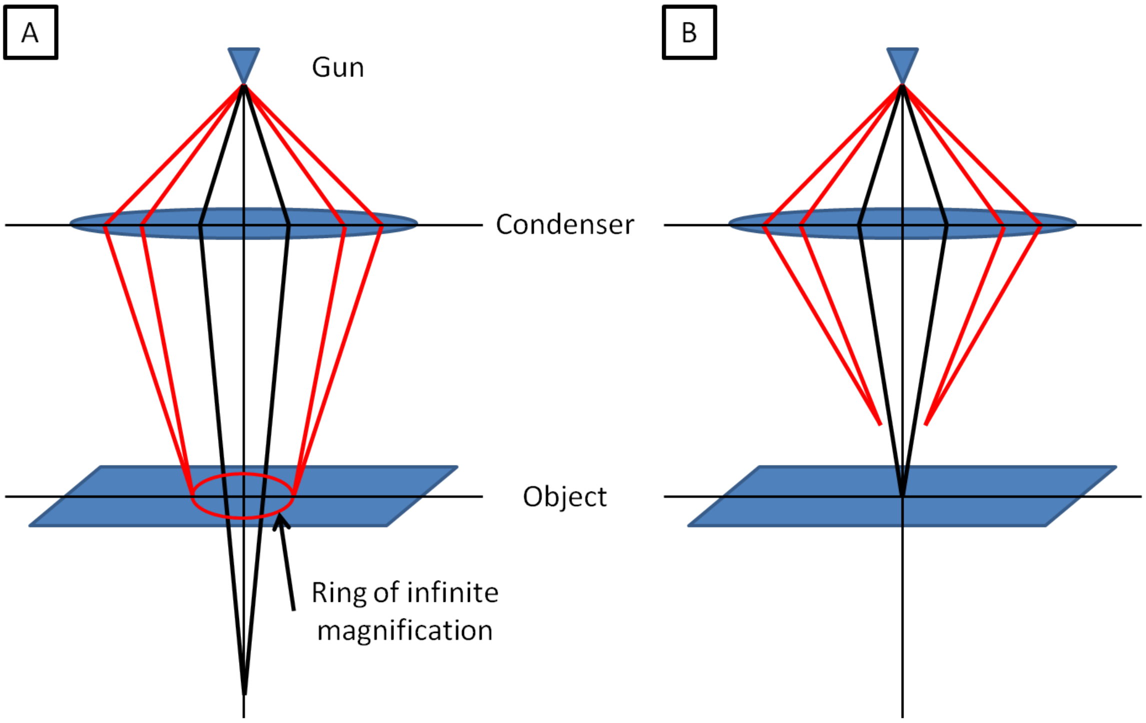

Figure 3.12: (A) A ray diagram showing how the ring of infinite magnification forms in the Ronchigram. The outer rays that suffer from the increased magnification (red) caused by the spherical aberration focus before the inner rays (black) producing a ring of infinite magnification around an area of high magnification. (B) The other extreme where the central rays are focused onto the sample, and the outer are focused above.

sample the outer rays will focus before the sample is shown in Fig. 3.12(B), producing an area of infinite magnification surrounded by areas of high magnification.

The larger the area of similar magnification, before the focal point of the rays deviates, for a given condenser lens current, the lower the spherical aberration in the microscope and therefore the higher the resolution. Other aberrations can be observed in a similar manner, for example any astigmatism will deform the ring of infinite magnification into an oval. In an aberration corrected microscope the difference in focal length between the outer rays and the inner rays is reduced, so larger areas of the Ronchigram will appear at the same magnification.

Fig. 3.13 shows some experimentally obtained Ronchigrams from JEOL JEM-2200FS aberration corrected microscopes Fig. 3.13(A) from a JEOL publication[25] showing the improvement from uncorrected imaging and corrected imaging and 3.13(B) from the microscope used in this study. The Ronchigrams in Fig. 3.13(A(b))&(B) show the breaking of the spherical symmetry used in aberration correction, as the patterns in the Ronchigram are not spherically symmetric.

Multislice Simulation

The modeling of HRTEM images involves the calculation of the exit-wave function i.e. the function of the electron wave after it has passed through the sample. This is achieved by one of two methods, either the Bloch-wave method or the multislice method. Here we shall briefly describe the multislice method.

The multislice method models the crystal as many thin slices, so that the WPOA applies to each slice. The potential of the slice is projected onto a 2D plane, then the projected potential calculated. The electron wave is then propagated through each slice. The exit wave from the slice is then used as the incident wave for the next. This process is repeated until all the slices have been taken into account. This exit wave is then propagated through a simulated microscope and an image formed. This process allows the comparison of images from proposed structures and experimental images. In general this process is repeated as a function of thickness and defocus for any given structure.

Modeling of STEM images is much more computationally expensive than HRTEM as each pixel must be simulated individually then reconstructed back into an image. This

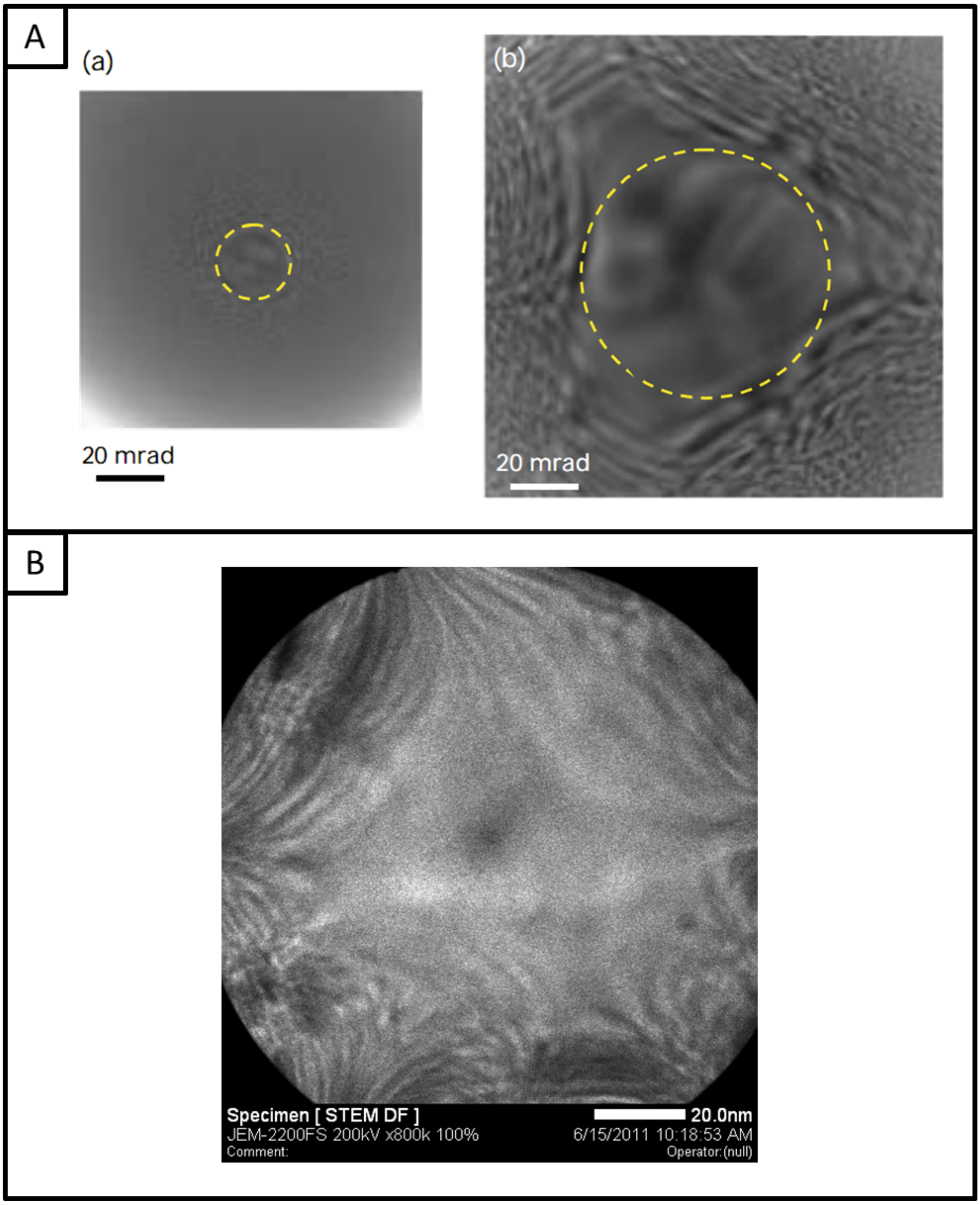

Figure 3.13: (A) two Ronchigram images from a JEOL publication[25] detailing effect of the hexapole aberration corrector on the JOEL JEM2200FS microscope (a) the Ronchigram with the hexapole off and (b) with the hexapole on, showing the improvement. The yellow dotted line indicates the area of similar magnification, expressed as an angle in mrad. (B) a Ronchigram from our microscope. Note that the scale bar in (B) has not been calibrated to mrad.

process is usually repeated many times with the atoms slightly deviated from their optimum positions and the resultant images averaged. This is the frozen phonon method and tends to give much more realistic results.

3.3.6 EELS

EELS spectroscopy gives detailed information about the chemical nature and bonding within the sample by examining the intensity of the transmitted electron beam as a function of energy-loss. The shape of the loss spectra gives characteristic information about the sample through the position and shape of peaks within the loss spectra.

3.3.7 Characteristic energy-losses

As a high energy electron from the incident beam passes through the sample there are a limited number of interactions that the electron can undergo [141]. These specific interactions can impart a specific energy-loss to the electron as it passes through the sample [142]. If the sample is thin enough we can assume that each electron only undergoes a single energy-loss incident as it passes through the sample. This assumption is usually valid as areas in the sample that give good images tend to be very thin, of the order of $\leq$100nm and the mean free path for plasmon generation is of the order of $\sim$100nm and for core loss events are $<$100nm.

By examining the energy of the electrons after interacting with the sample it is possible to associate the energy-loss peaks with specific events. The JEOL JEM-2200FS is equipped with an Omega filter which allows the splitting of the electron beam into its component energies to achieve this. The energy-loss processes that are of interest to this study are core losses, where the electron in the beam excites an atom in the sample by removing a core shell electron, and the fine structure of the core losses, that impart information about the local bonding of the excited atom [143]. The energy required to remove the core shell electron is well defined and leaves a characteristic peak in the energy-loss spectra. The fine structure appears as a variation in the shape of the core loss peak and can be used to identify different bonding arrangements, i.e. it is possible to distinguish between Si atoms in crystalline Si and Si atoms in SiO_2 using the fine structure.

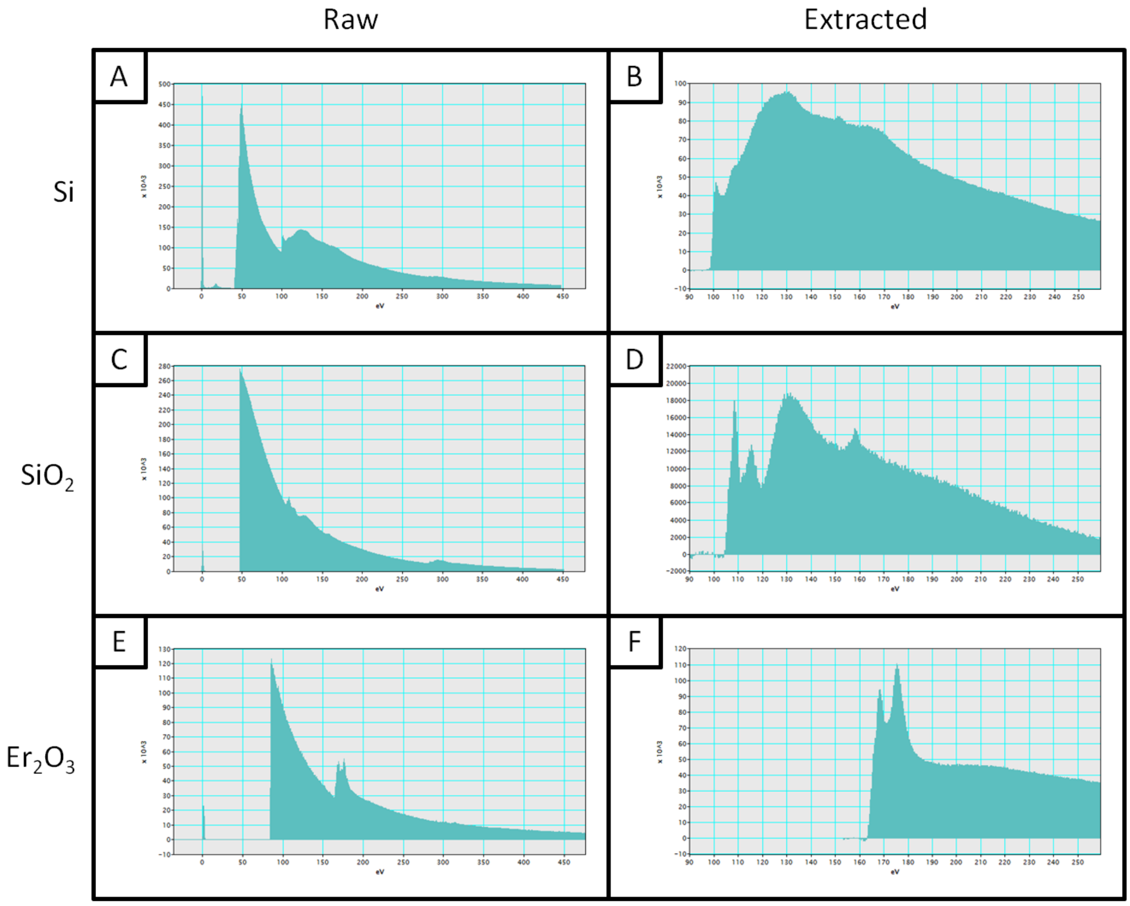

Figure 3.14: Three sample spectra and extracted signals from a Si sample (A) & (B), a SiO$_2$ sample (C) & (D), showing the Si$_{L_{2-3}}$ edges and a Er$_2$O$_3$ sample (E) & (F) showing the Er$_{N_{4-5}}$ edge.

3.3.8 Sample Spectra

Fig. 3.14 shows three sample spectra from the GATAN EELS atlas from the Digital Micrograph program [144], alongside the extracted peak. Images (A) & (B) show the energy-loss spectra for the silicon Si$_{L_{2-3}}$ edge, images (C) & (D) show the energy-loss spectra for SiO$_2$. Images (E) & (F) show the energy-loss spectra for erbium oxide Er$_{N_{4-5}}$ edge. The different samples have different EELS spectra that vary in the onset energy of the edge and the shape (fine structure) of the edge. These variables are used to identify different elements and chemical bonding arrangements within a sample.

3.3.9 Image Manipulation and Display

Contrast and Brightness

Due to the Z-contrast imaging in STEM and the large difference between Er(Z=68) and Si(Z=14) the STEM images that we obtain have a huge difference in intensity between the Er and Si columns. This presents challenges to get both Er and Si to display within one image. There are various methods to combat this with non-linear look up tables (LUTs), colour images or colour ramped LUTs etc. However it was found that as we are interested in the interface of the rare earth silicide and the silicon, having a colour transition in this critical region was not workable. Colour ramped LUTs place colour transitions at the interface which make interpreting the structure confusing, and non-linear LUTs smooth out the intensity variations in order to better display the areas of extreme low and high intensity.

Throughout this work there have been images obtained with very different levels of resolution and sample thickness, thus we shall treat each image individually in order to best display the information that is relevant at the time. We shall not display any colour images as often an image that displays well in colour also displays well in gray scale which is easier to interpret as intensity. Where necessary we shall include insets where the contrast and brightness have been stretched to better show the silicon positions.

Bandpass Filtering

The images obtained often have noise associated with scan coil instabilities, superimposing high frequency noise onto the image, and leading to spurious structure within the images. Bandpass filtering selectively removes the high frequency and low frequency noise from an image, by filtering in reciprocal space. This is an extremely powerful technique that is capable of dramatically improving the interpretability of images, however care must be taken when filtering in order not to introduce artificial features. Fig. 3.15 shows the effect of changing the filter frequencies on an image. On the left hand side Fig. 3.15(A,C,E) show how decreasing the high frequency cut-off can remove scan noise from an experimental image (C), but decreasing too far can begin to smooth out the signal (E). Increasing the low frequency cut-off can be used to limit intensity variations within an image, however if done incorrectly this can introduce artificial intensity variations. An example of this is shown in Fig. 3.15(B,D,F) where a dark region appears underneath the bright feature in the image. In our case we want to filter out any scan noise while not altering the low frequency variations. In order to achieve this we filter high frequencies that are shorter than half the Si atomic size and low frequencies that are $\sim$5 times the size of the image. For example a 1024px$\times$1024px image with a separation of the silicons within the dumbbell of 10px the standard settings would be a 5px-5000px filter.

Image Tilting

During STEM scanning, the sample can sometimes drift during the image taking procedure. This drift can lead to a distortion of the image that effectively transforms a square object into a parallelogram. If we assume that the drift is constant throughout the image acquisition and that the time to acquire a single line is small compared to the drift rate we can correct the image by shifting each row of pixels relative to the next and imposing an artificial drift.

We can measure the amount of shifting required by making measurements on the silicon substrate from STEM images. The angle between the (001) and $(1\bar{1}1)$ directions should be 90° when viewed along the [110] direction, as is the case in the cross sectional samples used in this study. Any deviation from this shows a distortion within the image which can be corrected. This was achieved using Matlab codes which are shown in Appendix C.

3.4 Density Functional Theory

Although not used in great depth in this thesis there are a lot of publications referenced in the discussion and analysis that rely on Density Functional Theory (DFT) results. As no results from this technique are presented in this thesis however a working knowledge of the technique will be useful to understand background material and future work.

DFT allows the calculation of the electronic configuration of a many body system. This information on the electronic structure is used to determine many properties of the system, but most commonly the ground state energy of that system.

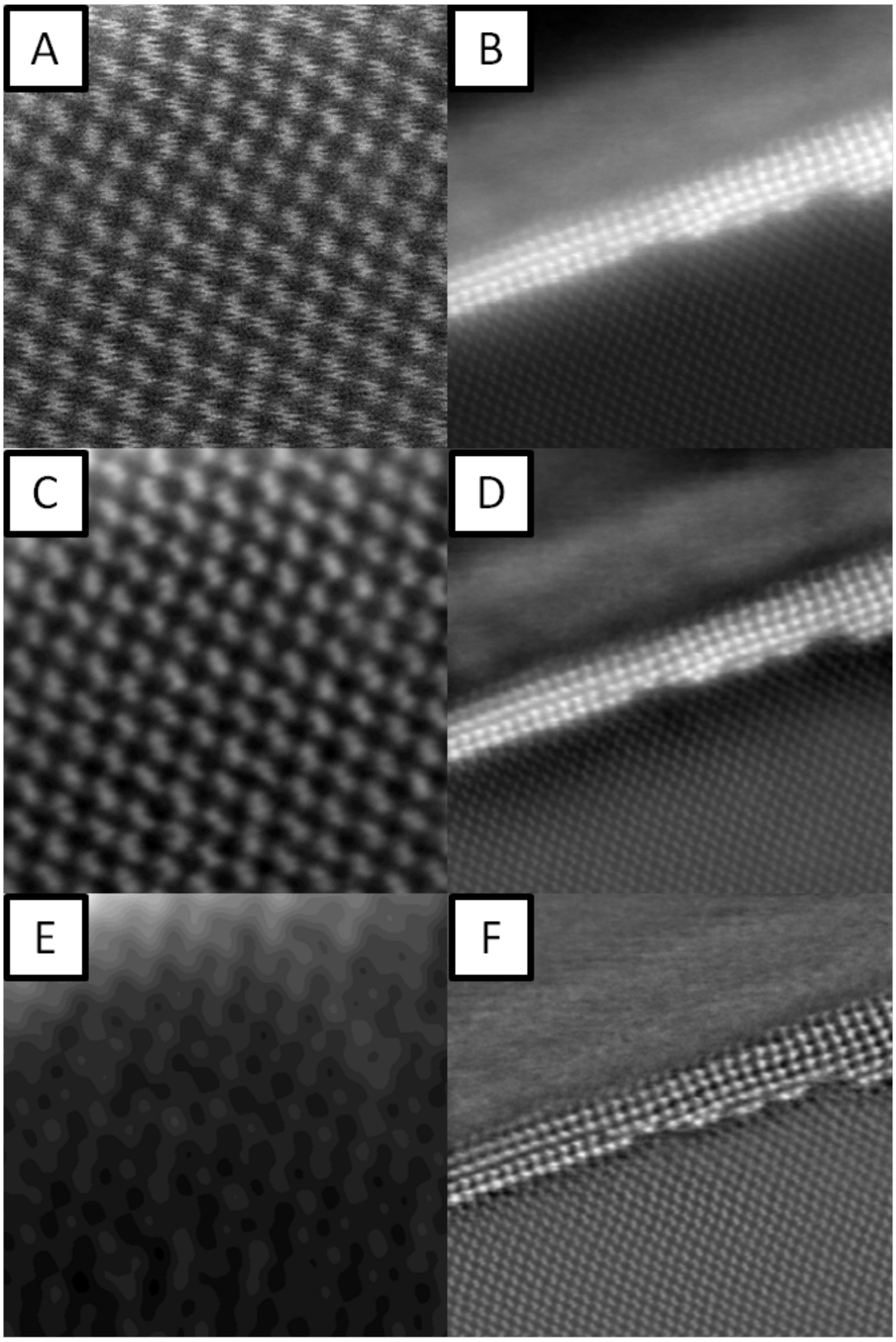

Figure 3.15: Images detailing the effect of bandpass filtering on an experimental image. The images of silicon on the left are cut from larger images similar to the ones on the right. (A)&(B) are unfiltered images, with (A) showing scan noise in the image. (C) shows appropriate high frequency filtering, removing the scan noise, without significant degradation of the atomic structure. (D) shows low frequency filtering introducing a dark band above and below the bright feature in the image. (E) shows high frequency filtering that has removed the signal from the silicon columns. (F) shows very aggressive low frequency filtering that has removed the intensity variation in the image.

3.4.1 Structure Optimisation

Using DFT to compute a ground state energy for a given structure in itself is not particularly useful, however by allowing the program to calculate the forces on all the atoms in the given structure and allowing the program to shift the positions of the atoms between ground state energy calculations, DFT can be used to find lowest energy structures. This method will only ever find the local minimum, so configurations of atoms that are lower in energy than the local minimum but have some energy barrier for formation will not be found.

3.4.2 Strained Energy Estimation

Once the lowest energy atomic configuration is known and its associated electronic and bonding energy this structure can be deformed and the ground state energy of the deformed structure calculated. By comparing the ground state energy of the original and deformed structures the energy required to deform the structure can be estimated. This can be extended by performing a series of calculations for increasing deformation the equivalent of the spring constant of the structure can be found.

3.4.3 Electronic Properties

Once the optimal structure has been obtained, and therefore the corresponding electronic structure for that system the electronic properties of that system can be estimated by looking at the band structure.

3.4.4 Combined Calculation and Image Simulation

Combining DFT structure optimisation and energy calculations with electron microscopy techniques produces a powerful tool for determining structure. Approximate structures can be produced by examining images of a crystal structure, these initial guesses can then be optimised and compared using DFT and the most likely (lowest energy) structure can be put forward. This greatly reduces the number of calculations that need to be performed to find a likely structure.

DFT and STM

By combining DFT and STM initial nucleation and preferential binding sites can be investigated in great detail. Structures observed in STM can be directly compared to results of DFT calculations [145] which provide greater detail on the bonding mechanisms. This combination of techniques allows the investigation of the earliest stages of epitaxial growth. By investigating the stable structures during this early stage of growth the growth mechanisms can be investigated and the driving forces behind the growth found.

DFT and STEM

By performing a structural optimisation on an initial guess structure and feeding the result into a STEM simulation, DFT structure results can be compared to experimental STEM results. This gives a rigorous check for the DFT results, as well as allowing various candidate structures to be compared against each other.

By comparing the relative intensities of columns in the experimental and simulated STEM images small variations in the structure such as vacancies along an atomic column can be observed.

3.4.5 Issues

DFT calculations, depending on the size and atomic species present in the system can be extremely computationally expensive. In general the more electrons an atoms has the more computationally expensive it is to model, thus large systems of rare earth silicides are currently extremely challenging. Meaning that as of yet no calculations have been published of nanowires that contain more than 5 rare earth atoms in cross section. In order to compare calculated structures with experimental results either experimental results of smaller nanowires are required, or calculations of larger structures which using available computers and methods are not forthcoming.

Chapter 4

The Growth and Effect of Capping on ErSi_{2-x} Nanostructures on Si(001)

4.1 Introduction

This chapter focuses on the proving of the chosen growth method and the subsequent steps taken to improve the method in order to reduce oxidation of the nanostructures during TEM sample preparation. In order to protect the ErSi_{2-x} nanostructures the nanostructures were capped, post growth in titanium or silicon. To ensure the capping procedure was not affecting the nanostructures some checks were performed and the effect of the capping procedure on both the structure and the beam sensitivity will be detailed here.

4.2 Experimental

4.2.1 Sample Preparation

Growth Method

The methods used in the literature for growing the rare earth silicide nanowire system on Si(001) can be grouped roughly into two types. Depositing the metal onto a cold surface and post annealing [20, 116], or depositing directly onto the Si(001) surface held at elevated temperature [28, 72]. Post annealing of the sample for a few minutes is more common than not [109], however it has been found that ‘freezing’ the sample post growth also produces nanowire structures [26, 28] and allows access to structures that form during the early stages of growth.

Our nanowires were grown by depositing sub-monolayer amounts of erbium onto 4° vicinal Si(001) at elevated temperature with no post annealing. The silicon substrate was outgassed overnight at 600° C. As the quartz microbalance is extremely sensitive to small temperature changes within the chamber the Er source was calibrated prior to flash cleaning the sample. This procedure has a twofold benefit of cleaning off any contamination from the outgassing of the erbium source, and eliminating any background temperature effects that are caused by having heated up and cooled the sample manipulator during the flash process. However care must still be taken as the source does heat the quartz microbalance slightly. In order to limit the effect of heating, the source was heated to a point just below the onset of deposition, usually around 18A so the microbalance has time to stabilize and a background reading can be obtained.

The source heating current was tuned to give a deposition rate of 0.5ML in $\sim$20 minutes. Once the deposition rate of the source was calibrated the sample was flash heated to 1200° C for 30s, then held at 900° C for 60s. The sample was then slowly cooled to 700° C at a rate of 10° C every 20s to ensure a good surface reconstruction. Once at 700° C the sample was cooled at a non specified rate to 600 ° C ready for deposition. 0.5ML of erbium was then deposited onto the substrate. At the end of the deposition the sample heating was immediately switched off. This ensures that we have the highest concentration of the smallest nanowires and are able to investigate the initial growth of nanowires and islands.

Care was taken to ensure that each chip of silicon used to grow nanowires was orientated in the same direction so that the heating current was always passing through the sample in the same way, as it is possible that electron current is able to affect the migration of Er atoms on the surface as electromigration of adatoms on semiconductor surfaces has been observed [146] in other systems. Our samples were orientated with the current passing parallel to the terraces, i.e. parallel to the extended growth direction of the nanowires.

During the deposition the pressure within the system was never greater than 1×10^{-8} mbar and routinely less than 1×10^{-9} mbar and at best less than 5×10^{-10} mbar. For those samples that were capped, titanium or silicon was deposited onto the sample at room temperature, after any STM imaging, to protect the nanowires from oxidation during the cross sectional sample preparation.

TEM Sample Preparation

The samples were cut and thinned using the standard method described in Appendix A to give cross sectional TEM samples orientated so that the extended growth direction of the nanowires was parallel with the viewing direction. Some samples were cleaned with optical baking at ∼60°C in vacuum and / or low energy plasma cleaning to reduce contamination during electron microscopy imaging. Neither of the two methods were found to alter the morphology of the nanostructures.

Image Manipulation

The images obtained often have noise associated with scan coil instabilities and drift of the sample. The huge difference in intensity in HAADF STEM between the Er and Si atoms also presents some issues with displaying images as the contrast and brightness often have to be adjusted in order to display either the Si or the Er structure as it is can be difficult to display both within one image without harsh bandpass filtering or nonlinear look-up tables (LUT's). Often we choose to limit the amount of image manipulation to a minimum, while still being able to display the feature of interest within the image, in order not to introduce any contrast variations that can be mistaken for structure, as highlighted in section 3.3.9.

Some images have been manipulated by one or many of the following procedures: scaling, contrast and brightness adjustment, tilting and real space nearest neighbor smoothing or FFT bandpass filtering, in order to improve the quality of the displayed images, while highlighting the important structure. The procedure used for FFT bandpass filtering was discussed in detail in Section 3.3.9.

4.2.2 Sample Analysis

In-Situ Analysis

The initial characterization of the growth was performed to ensure that the chosen method was producing structures of interest reliably. The analysis was performed in-situ using STM and LEED. LEED was used to check the quality of the cleaned silicon surface to ensure that the Si(001) (2×1) reconstruction formed on the Si(001) surface prior to growth, and to quickly check to see if the LEED pattern had altered indicating the presence of nanowires after the growth. After it was found that the cleaning process was reliably producing suitable surfaces this step was omitted as the electron beam used in LEED can introduce small amounts of contaminants to the surface through outgassing of the electron gun and carbon cracking. The deposition rate from the source can drift during the extra time required to make measurements, reducing the accuracy of the deposition thickness. After the sample had cooled to room temperature some samples were transferred to the STM to observe the morphology of the grown nanostructures. This was initially done after every growth to confirm the presence and the quality of the nanostructures. In later growths this was step was performed only after the system had been vented to ensure that nanostructures were being produced, as the growth was found to reliably produce nanostructures and we are not concerned with the relative concentration of nanowires to islands.

Ex-Situ Analysis

Ex-situ analysis was performed in a JEOL JEM-2200FS operating at 200kV in HAADF STEM mode and EELS spectra were also obtained to compliment HAADF data when necessary. The microscope was operated with condenser aperture 3 with a semi-angle of 24 mrad, at a camera length of 30-50cm. The tuning was performed until the usable area of the Ronchigram, as measured by the CEOS corrector, was $\geq$17 mrad. The tuning of the aberration correctors was performed with condenser aperture 4 with a semi angle of 12 mrad.

4.3 Growth

4.3.1 Background

The morphology of ErSi_{2-x} nanostructures has been shown to highly sensitive to the growth conditions [20, 93, 98, 109, 110]. So careful analysis of the final structures is necessary as temperature measurements from one growth system to the next are rarely consistent. This means that growth procedures perfected on one system must be checked when transferring to a different system. We need to ensure that the growth procedure that we are using is producing nanowires that we are interested in analysing. In this case we are optimizing for long thin nanowires with a few larger islands, so we are able to analyse long thin nanowires which are of more technological and fundamental physics importance while checking our results with the better studied larger islands.

Ye et. al. found that a slow deposit encouraged a higher ratio of nanowires [98].

Zhu et. al. investigated the effect of post annealing time and temperature and found that increasing the annealing time encouraged the wires to get longer and wider, reducing the frequency of the thinnest nanowires. They report that an increase in annealing temperature of 50° C from 650° C to 700° C was enough to reduce the number of the smallest nanowires to effectively zero [20]. The figures showing the distributions of observed nanowires for the varying conditions are shown in Fig. 4.1. Zhu et. al. used a cold deposit, post anneal growth, where we have used a hot growth, however the evolution should be similar between the two growth methods.

Throughout this thesis we shall make the assumption that in general a wider nanostructure is ‘older’ in that they have had longer to grow then the thinner nanostructures. This is justified in that our growth method has a continuous deposition over $\sim$20 minutes and no post annealing, so a structure that nucleated at the beginning of the growth will have had much longer to form than one that nucleated towards the end of the growth. This combined with previous studies that have found that post annealing for longer after the growth encourages wider features [20] allows us to make this assumption.

Liu et. al.’s growth method [28] is much more similar to the one we use where samples are grown at elevated temperature with either post annealing or a post deposition quench where the heating to the sample is immediately switched off. Liu found that by post deposition quenching it was possible to limit the formation of islands and preserve the smallest and thinnest wires for dysprosium silicide[28].

Our growth method aims to produce a high concentration of long nanowires as these are the more technologically interesting structure with a number of larger islands in order to link our work to previous studies. To that end we have chosen a long deposition time (15-20 minutes) at a low growth temperature (600°C) with no post annealing.

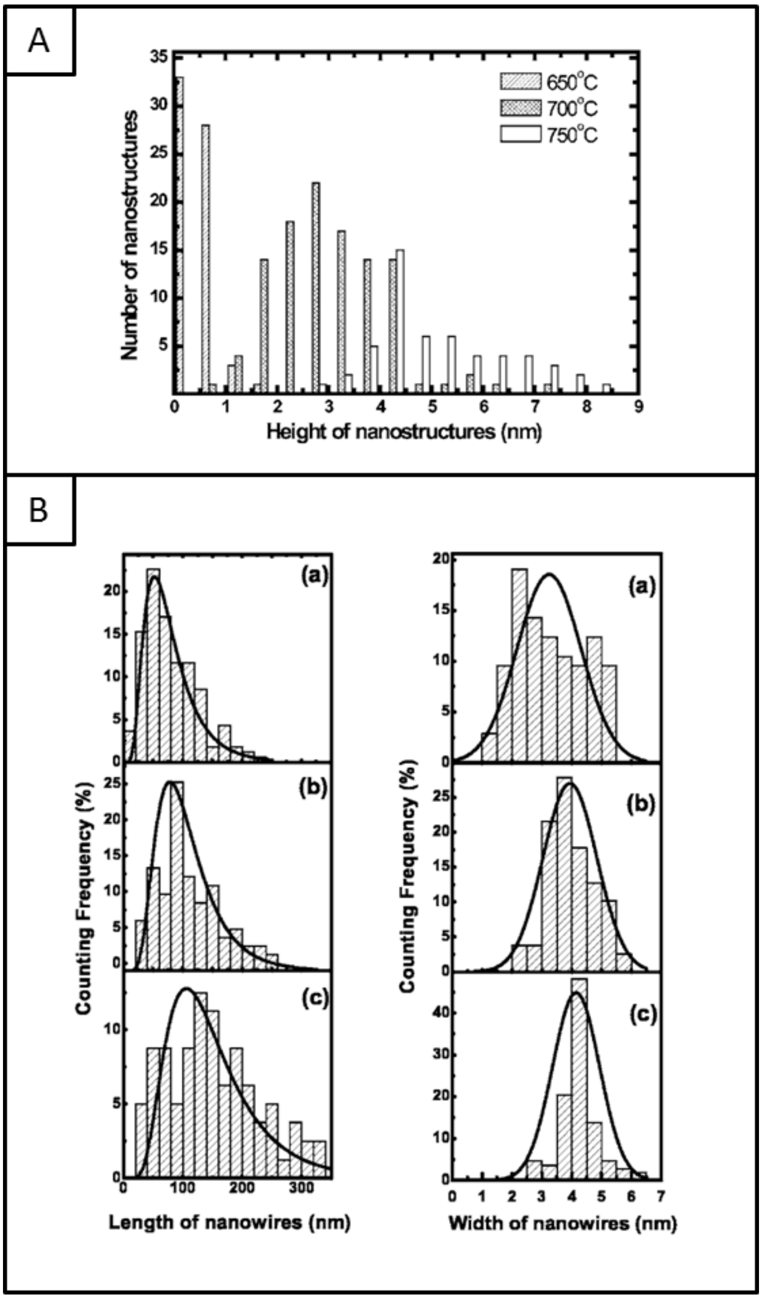

Figure 4.1: A composite image showing the results from Zhu et. al.'s paper [20]. (A) The effect of a 10 minutes anneal on the height of the nanowires as a function of post annealing temperature. As the temperature increases the nanowires get taller. (B) the effect of a 615°C anneal on the nanowires as a function of time, (a) 30 minutes (b) 90 minutes (c) 180 minutes. As the annealing time increases the nanowires get longer and wider, widening the length distribution and narrowing the width distribution.

4.3.2 Interpreting STEM Images

When interpreting STEM images it is necessary to understand which bright features correspond to which atomic columns in the structure. Fig. 4.2(A)&(B) show two simulated

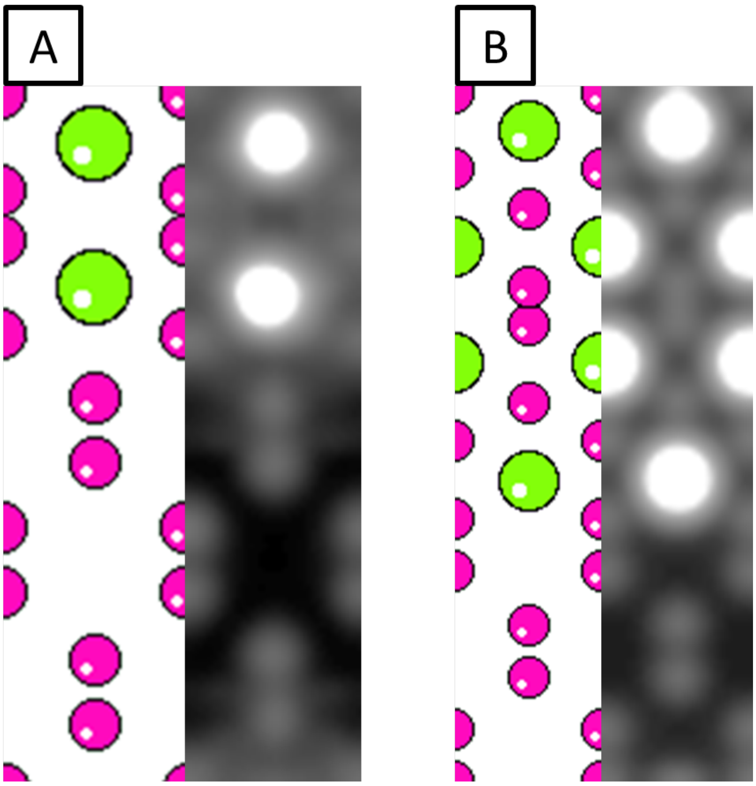

Figure 4.2: Two simulated STEM images next to the corresponding models that were used to generate them. Here pink atoms are silicon and the green atoms are erbium.

STEM images next to the models that were used to generate them. In this example the smaller pink atoms represent silicon and the larger green atoms represent erbium. We can see that the erbium columns correspond to an extremely bright feature in the simulated image, where the features that correspond to the silicon are much dimmer. This is due to the Z-contrast imaging that was mentioned in section 3.3.5. The two simulations have different interface structures and different bulk structures, and have a good 1:1 correspondence between bright features in the image and atomic columns in the model. We can therefore assume that any bright features that we observe in any STEM images correspond to atomic columns, and that relatively bright columns correspond to erbium and relatively dim columns correspond to silicon.

4.3.3 Results - Growth

STM

STM images of samples prepared using the growth method outlined in section 4.2.1 are shown in Fig.4.3(A) & (B). Fig. 4.3(A) shows a tunneling current map of a sample grown under the conditions outlined in section 4.2.1. Here the current map is presented as the height map is low quality. In this instance the scan speed was set too high for the tip to correctly follow the surface so features were introduced into the current map even though the STM was operated in constant current mode. The shadows after the features are areas where the tip is not in contact with the surface so no tunneling current was measured. Fig. 4.3(B) shows a height map of a sample grown at similar conditions to Fig. 4.3(A). The widths of the nanowires highlighted in Fig. 4.3(B) are given in Fig. 4.3(F) showing that the growth procedure is producing the ultra small nanowires of interest. The growth method is producing a suitable density of long nanowires of 100nm in length or greater, together with islands allowing analysis of both structures.

In general the STM operating conditions would start at a tip-sample potential of +2V on the sample, a tunneling current of 2nA and scan size of 500nm however these values were continually adjusted to obtain the best quality image.

The images show that even with similar growth conditions there can be a disparity between the relative numbers of nanowires per area and between the numbers of nanowires to islands. However we are not interested in the relative numbers of each or the relative concentration. We are interested in the bulk and interface structure of the grown nanostructures. Fig. 4.3(C) shows a nanowire from a sample that was grown at a slightly lower temperature than the rest of the samples shown in this thesis, however the structure of the nanowires has not been found to vary with growth temperature, just the relative numbers and morphology. The black lines indicate the location of the linescans shown in Fig. 4.3(D)&(E) which shows the nanowire to be $\sim$3nm in width. The nanowire shows that the top surface is not smooth but has areas that are higher than the rest. These features have been attributed to second layer growth on the nanowire.

STEM

The nanowires and islands on our samples produced a variety of different structures and morphologies that are not necessarily evident from STM. The structure of the ultra small nanowires will be discussed in Chapter 5 and the interface structures we observed will be described in Chapter 6.

It was noted that the although the relative numbers and density of islands or nanowires can vary greatly from one sample to the next, the structures of the islands and nanowires

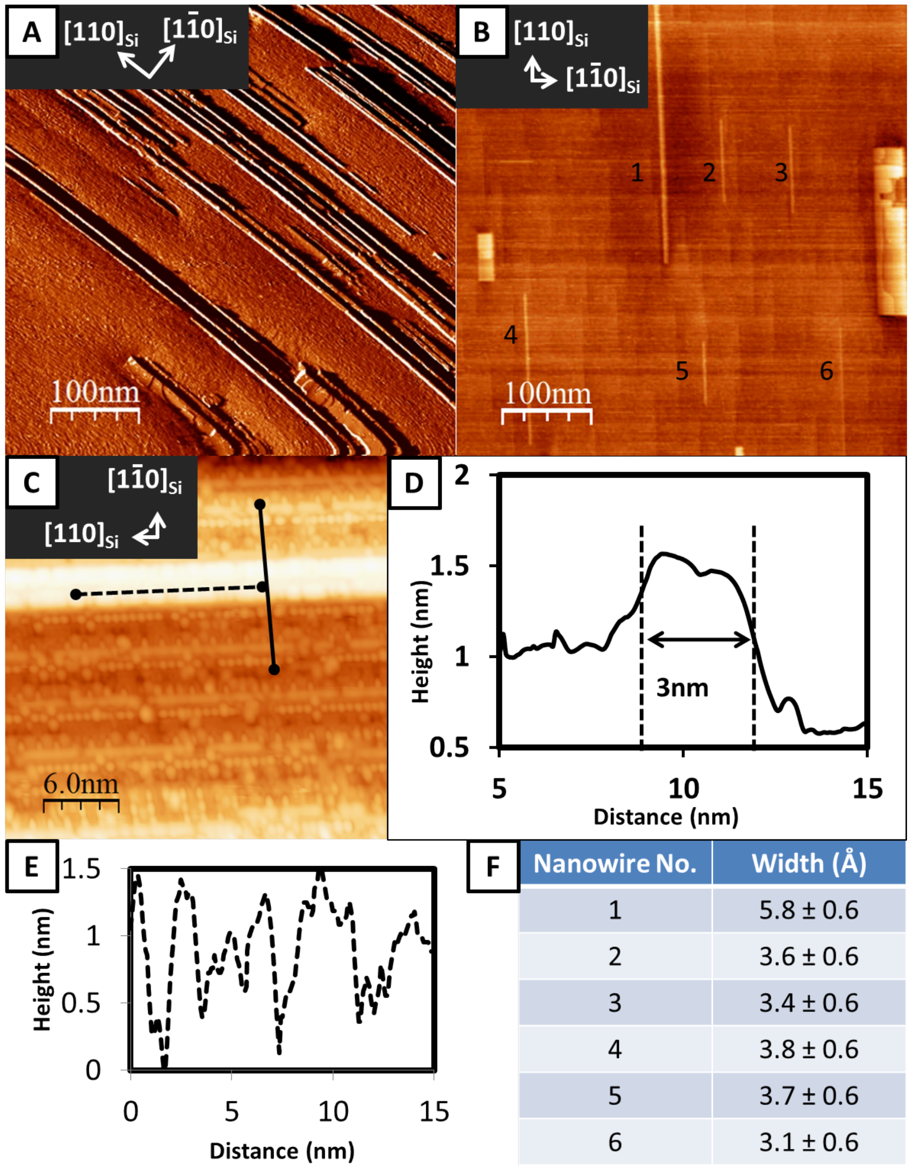

Nanowire No.	Width (Å)
1	5.8 ± 0.6
2	3.6 ± 0.6
3	3.4 ± 0.6
4	3.8 ± 0.6
5	3.7 ± 0.6
6	3.1 ± 0.6

Figure 4.3: (A) A tunneling current map of a sample grown under the conditions outlined in section 4.2.1. (B) A height map of a different sample grown at similar conditions. (C) A high magnification STM height map of a single ultra small nanowire from a sample grown at a slightly lower temperature. The solid black line represents the location of the line scans shown in (D) and the dashed black line shows the location of the line scan shown in (E). The silicon surface shows the terraces that are introduced by using vicinal silicon. (D) A line scan of the nanowire in (C) with a width of 3nm. (E) A line scan from (C) showing that the surface of the nanowire is not flat and has a lot of second layer growth (F) The widths of the nanowires marked in (B).

vary in a similar way across all samples, and independently of the relative concentrations. Five separate nanostructures from five separate TEM samples, separately grown over the course of 23 months are shown in Fig. 4.4. The structures show similar features in their bulk structure and their interfaces showing that there is a high level of reproducibility in

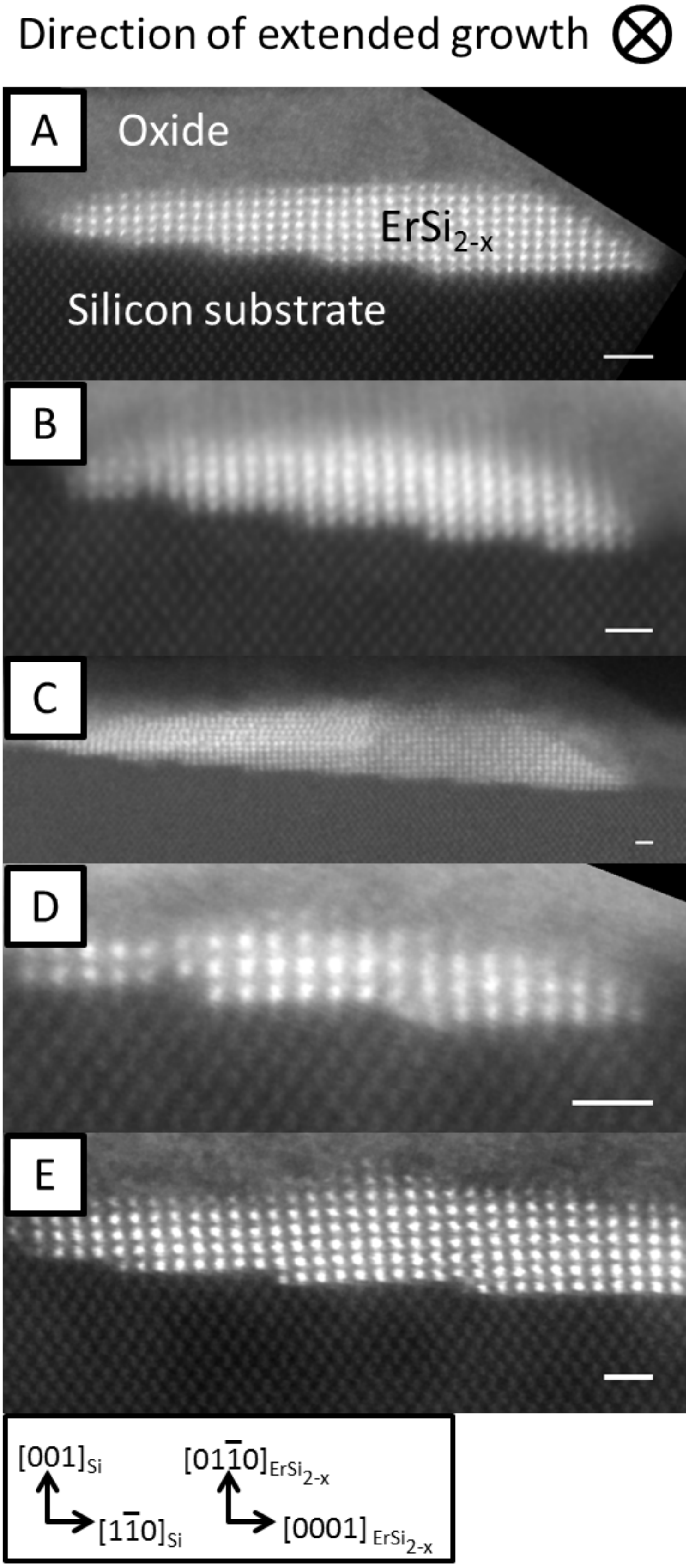

Figure 4.4: Five images of islands taken from 5 separate TEM samples from 5 separate growths spanning 23 months all showing similar structures. The scale bars in each of the images are 1nm in length. (A) grown June 2009 (B) Grown Jan 2010 (C) Grown Dec 2010 (D) Grown Mar 2011 (E) May 2011.

the structure of the nanostructures even if the reproducibility of the nanowire vs island ratio is poor. Common features across all samples were also observed for the smaller structures, however the details of these features will be discussed in later Chapter 5.

4.4 Capping

4.4.1 Background

The oxidation of the smallest nanowires has been a problem for microscopists who are trying to study the nanowire system [26, 35, 97, 98, 127, 128]. The rare earth silicides bind readily with oxygen as soon as they are brought out of the growth chamber into ambient conditions. The oxide will be shown to be self-limiting so larger islands are still able to be studied without capping. Many studies have been done on the silicide system using large islands and conventional HRTEM. However the ultra small nanowires have proven themselves to be extremely interesting from a fundamental view [13, 44, 58], as they show interesting 1D quantum effects. Being able to obtain a structure for the nanowires experimentally would be of great use for these studies. In order to be able to obtain the structure, first the oxidisation issue must be solved. One method to achieve this is to cap the samples post growth in a layer that will protect the nanowires from oxygen. However it must be shown that the capping procedure has not affected the system under study. This is impossible to achieve directly as we have no data for the unperturbed system; however we can look at the features of larger nanowires that have formed an oxide layer and compare with capped nanowires and see if there are any notable differences between the systems. We can also cap in more than one material and observe any differences between the structures observed under each layer. If the structures are identical we can postulate that the capping layer has not affected the nanowire structure as it is unlikely that the effect would be consistent across different capping layers.

In previous work there have been many attempts at reducing the oxidation of the nanostructures using a variety of different capping materials. As previously stated, attempts were made to cap the samples with titanium [26, 35], CaF_2 [97], amorphous silicon [127], gold [98] and tungsten [128]. These different materials had varying degrees of success. The titanium layer was found to be effective at protecting the erbium silicide from oxygen, however it was found that if deposited prior to heating a titanium silicide layer was formed [35]. CaF_2 was shown to effectively limit the oxidation, but there was no mention of the effect, if any, the capping layer had on the nanostructures. Amorphous Si has had no electron microscopy data as it was only used in UHV SEXAFS. Gold was determined not to alter the structure of the $RESi_{2-x}$ nanostructures, but was ineffective as a capping layer. Tungsten was shown to effectively protect Y from oxidation via X-ray photoelectron spectroscopy (XPS) with little intermixing on thin film source drain contacts, although no cross sectional electron microscopy measurements were made of this system.

Of the capping layers that were shown to be successful at reducing oxidation of the silicide no evidence has been presented to show that the capping procedure has not affected the morphology of the nanowire system. Here we compare the structures of uncapped nanowires and nanowires that were capped post growth in titanium or silicon. Titanium and silicon were chosen as they are readily available in our chamber and have been previously shown to be effective at limiting oxidation [35, 127].

4.4.2 Results - Capping

Oxide Layer

The bright amorphous layer above the silicide nanowires which can be seen in Fig. 4.6(B), (C) & (D) has long been assumed to be an oxide layer, however there has been no evidence published to prove this. We have the capability to prove this so, EELS spectra were taken from the three characteristic regions, the substrate, the nanowire and the bright overlayer. When silicon oxidizes there is an associated shift of the EELS spectra, the onset energy of the Si edge moves from 99.7eV to 106eV, where erbium has two characteristic peaks at 168eV and 175eV. Both the shift in the silicon edge from 99.7eV to 106eV and the twin peaks at 168eV and 175eV were observed in the bright amorphous layer, showing that in this case there is a fully oxidized Si layer present, hence, the assumption was correct. The EELS spectra from the three regions next to three reference spectra from Er_2O_3, Si and SiO_2 are shown in Fig. 4.5.

Uncapped Samples

Large nanostructures on uncapped samples were found to produce a self-limiting oxide layer that effectively protected the nanostructure from further oxidation. Smaller nanos-

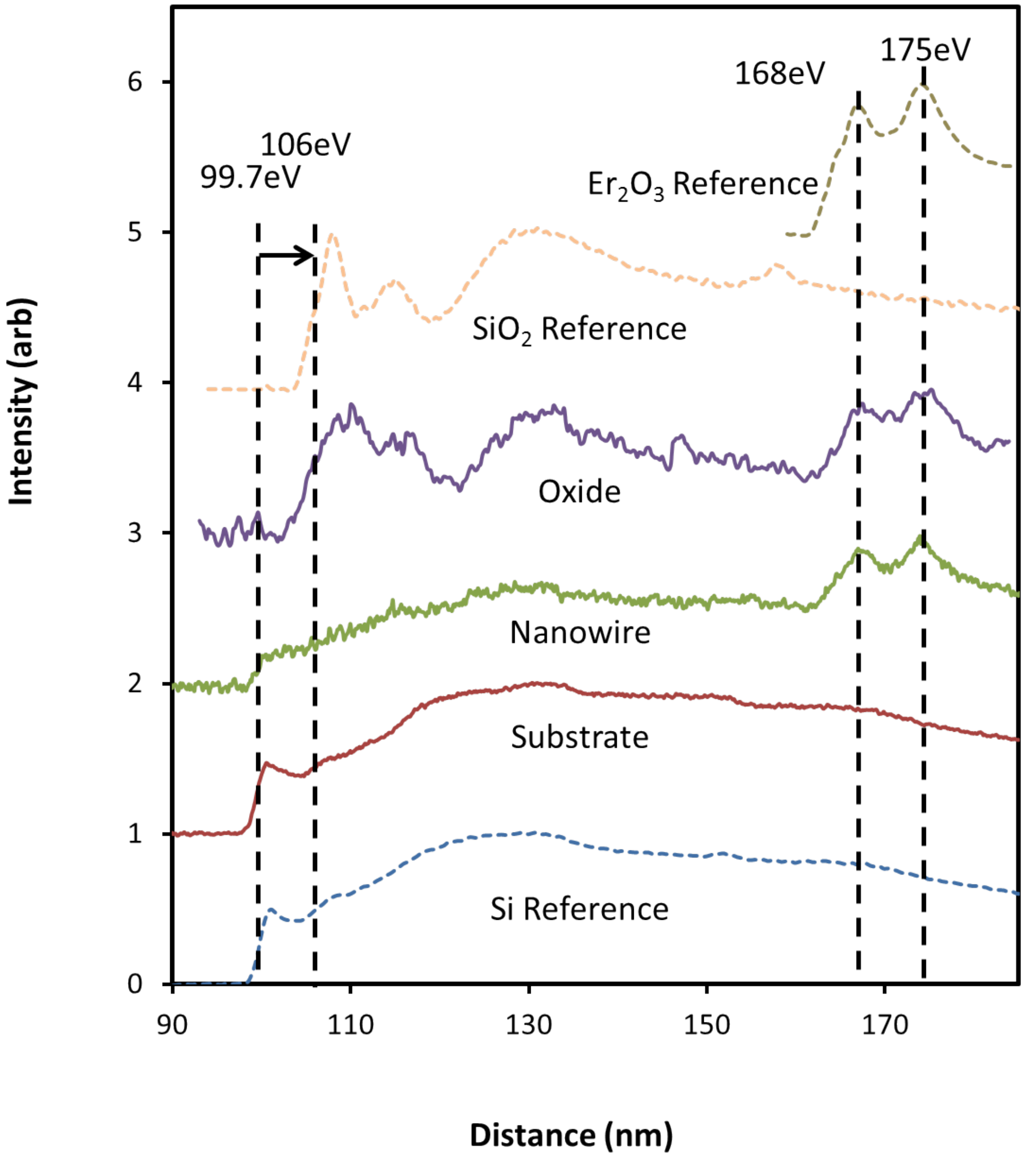

Figure 4.5: Three Representative EELS spectra from three distinct regions of the ErSi$_{2-x}$ system (solid lines), alongside three reference spectra (dashed lines): Upper Dashed Line: Er$_2$O$_3$ reference spectra. Middle Dashed Line: SiO$_2$ reference spectra. Upper Solid Line: The layer found above the silicide islands suspected of being an oxide. Middle Solid Line: From within the nanostructure. Lower Solid Line: From the substrate. Lower Dashed Line: Si reference spectra. There is a shift in energy of the main peak in the substrate spectra compared to the oxide spectra from 99.7eV to 106eV indicating that silicon has oxidised. The spectra from both the nanostructure bulk and the oxide layer show the characteristic twin peaks at 168eV and 175eV indicating the presence of erbium. The spectra have been scaled and shifted vertically for ease of viewing.

tructures were not able to form this protective layer and were completely amorphized by the oxidation. This is consistent with previous studies in that no small structures have been reported.

Fig. 4.6 shows some representative images from an uncapped sample. (A) A low magnification image showing bright nanostructures with a bright amorphous cap over the top of the nanowire. This was characteristic of all samples without capping. In some cases the bright area underneath the bright amorphous cap was absent, indicating that all the erbium had been incorporated into the oxide layer, this was most common for the smallest structures. (B) shows a higher magnification image of a similar structure, where the amorphous cap has been insufficient to protect the underlying nanostructure from amorphization. This structure of a bright cap with a bright amorphous region in contact with the silicon was extremely common. (C) A nanostructure where some structure remains underneath the amorphous cap. (D) A large nanoisland showing the amorphous cap and structure.

Titanium Capped Samples

The nanostructures on the titanium capped samples showed a reduced oxide layer, where many of the smaller nanostructures were still observable. The smallest nanowires were still amorphized and showed no structure. This ineffective capping was attributed to difficulties in depositing the capping layer resulting in the layer being too thin to effectively protect the sample from oxygen. Fig. 4.7 shows some representative images from Ti capped samples. (A) shows a large nanoisland that has been well protected by the Ti layer, which was measured at ∼5nm in thickness. There is still some minor oxidation of the nanoisland which is most noticeable at the left hand edge as a bright band beneath the Ti layer and above the island. (B) shows an ultra small nanowire that retains some structure even with some residual oxidation. (C) shows a nanowire that has been heavily oxidized despite the titanium capping layer, however still shows some structure. (D) a wire that has been completely amorphized by oxide.

Silicon Capped Samples

Silicon capping was found to be technically easier than titanium capping with the equipment available, as the deposition method was more reliable, stable and controllable. Sili-

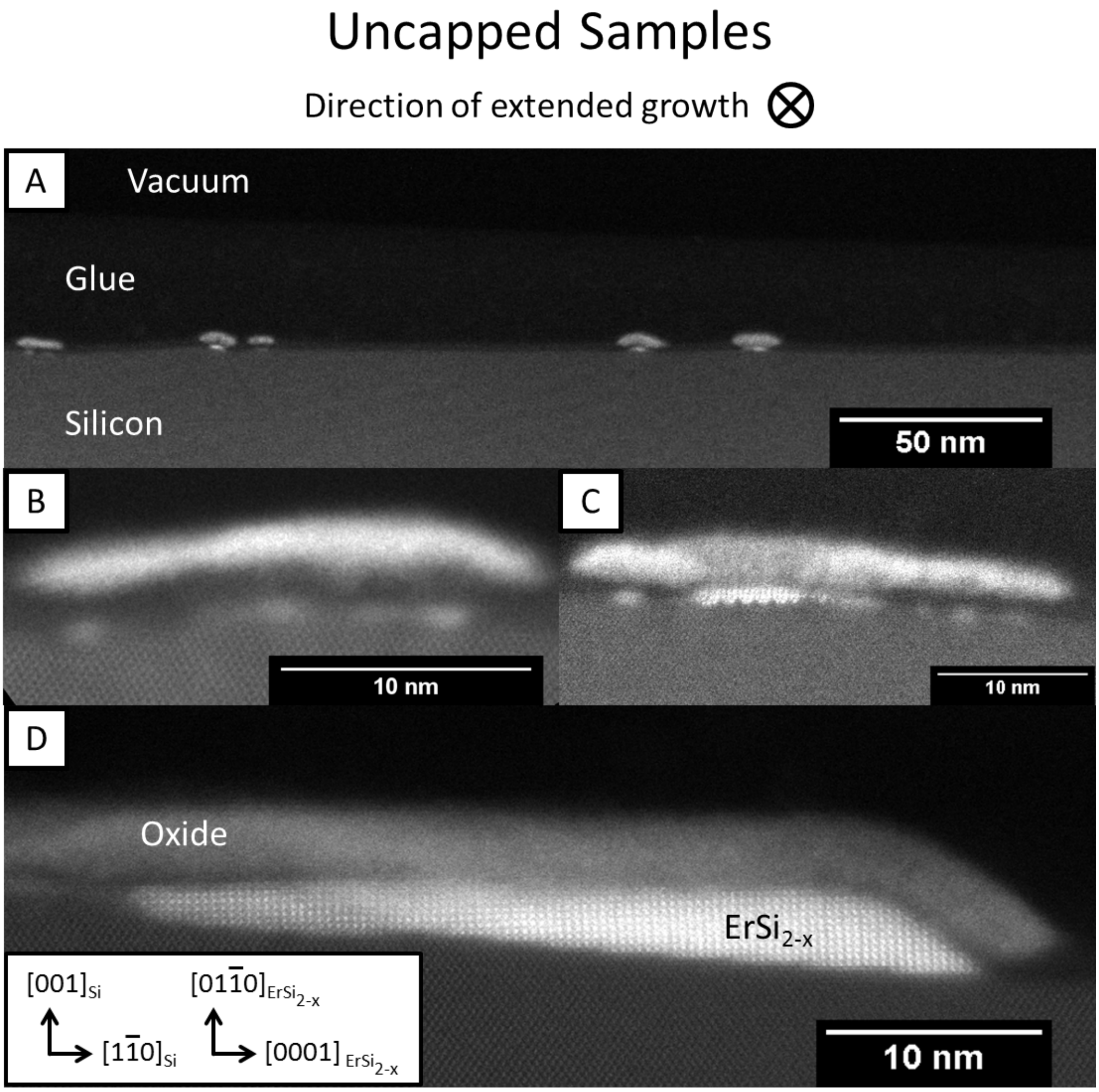

Figure 4.6: An overveiw of the types of structures that were observed on uncapped samples in HAADF STEM. (A) A low magnification image showing bright nanostructures with a bright amorphous cap over the top of the nanowire. (B) shows a higher magnification image of a similar structure, where the amorphous cap has been insufficient to protect the underlying nanostructure from amorphization. (C) A nanostructure where some structure remains underneath the amorphous cap. (D) A large nanoisland showing the amorphous cap and structure.

con capping produced the best protected sample observed with almost no oxidation on the smallest nanowires.

Fig. 4.8 shows some characteristic images from Si capped samples. (A) shows a low magnification image, which when compared with Fig. 4.6(A) shows the absence of the bright amorphous cap over the nanostructures. (B) shows a large island that has similar

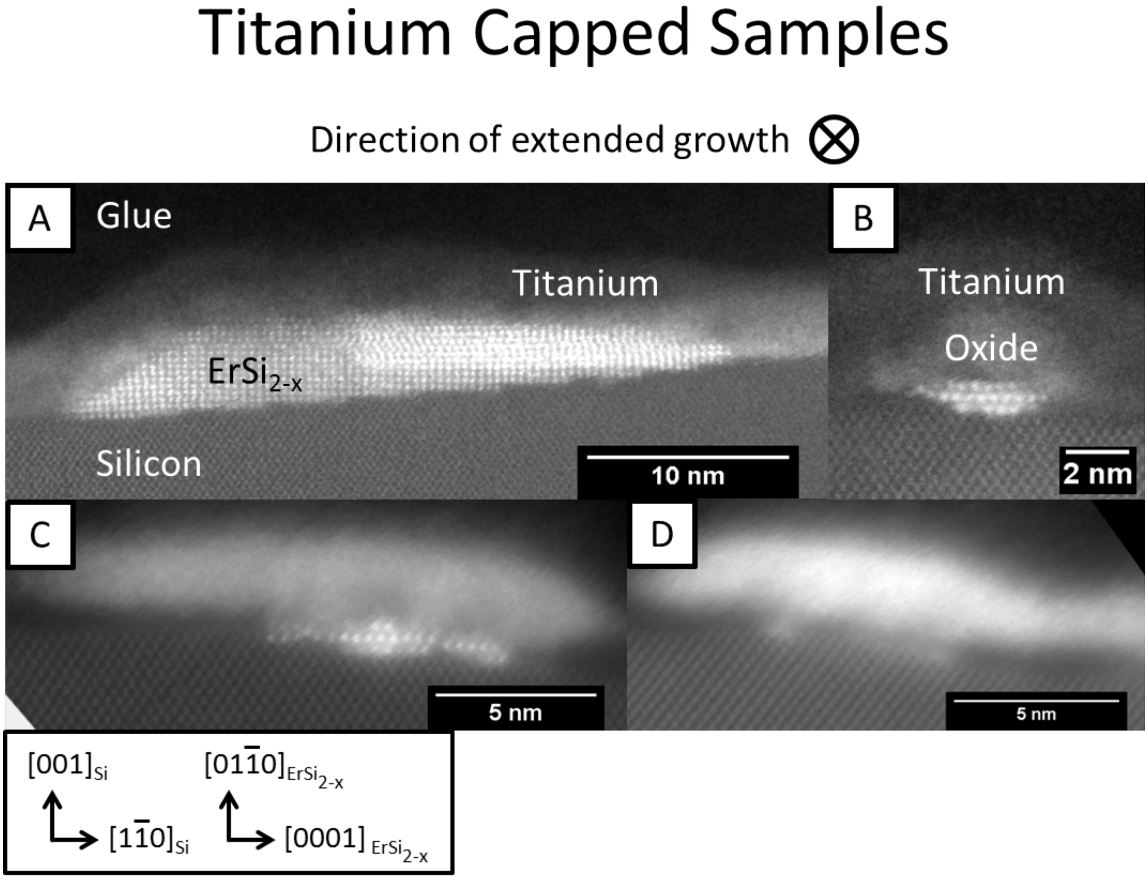

Figure 4.7: Typical HAADF STEM images from titanium capped samples. (A) a large island that shows signs of oxidation, despite the titanium capping layer. (B) An ultra small nanowire that has been protected from amorphization by the titanium capping layer, but still shows signs of slight oxidation. (C) A nanowire that still shows structure despite extensive oxidation. (D) A nanowire that has been completely amorphized.

interface features when compared with the large islands shown in Figs 4.6(D) & 4.7(A). (C) & (D) show a nanowire and an ultra small nanowire respectively that show almost no oxidation. The inserts in (C) & (D) have had the contrast stretched to better show the structure within the silicon substrate.

4.4.3 Discussion - Capping

Reduced Oxidation

Uncapped samples showed a typical bright amorphous oxide layer above the silicide island, as shown in the upper image of Fig. 4.9.

A layer of 5nm of Ti was sufficient to effectively reduce the oxidation layer from the

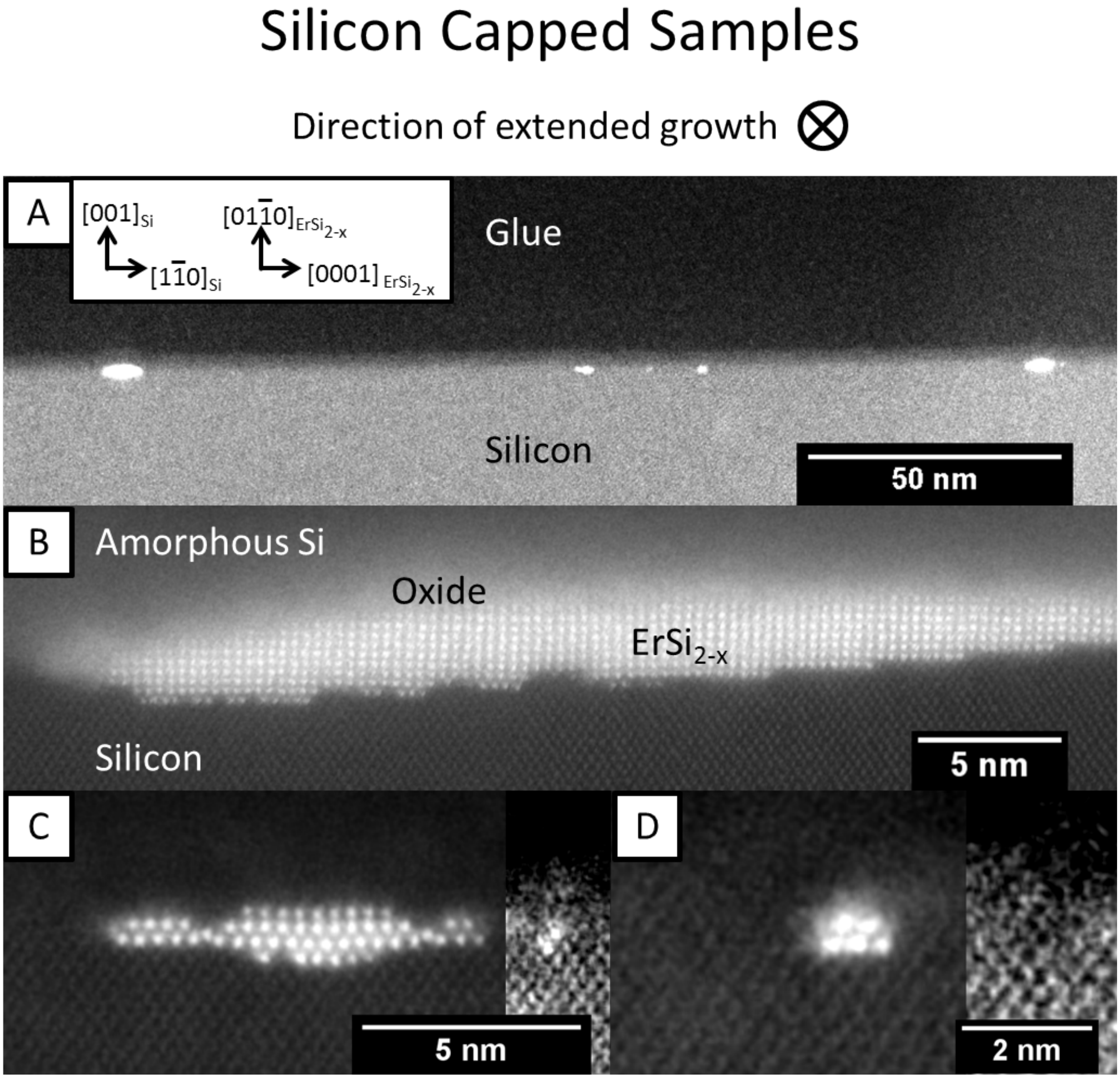

Figure 4.8: Representative images from silicon capped samples. (A) A low magnification image showing nanowires without the characteristic bright ‘cap’ that is observed in uncapped and some titanium capped samples that indicates oxidation. (B) A larger nanoisland from a sample where the Si capping layer was too thin and some oxidation has occurred. (C)&(D) Two nanowires that have been almost completely protected by the silicon capping layer, with (D) showing one of the smallest nanowires that was imaged with only 5 atoms in cross section. Images (C) & (D) have insets on the right with altered contrast and brightness to better show the silicon.

island shown in the lower image of Fig. 4.9. The titanium capped and uncapped samples shown in Fig. 4.9 have similar nanowire morphologies and interface characteristics, with similar average interface step widths. Silicon capped samples also exhibit similar characteristics as both uncapped samples and titanium capped samples. The fact that we observe similar structures under three separate capping layers, $ErSi_{2-x}$ oxide, titanium and silicon implies that the capping layers are not affecting the structure.

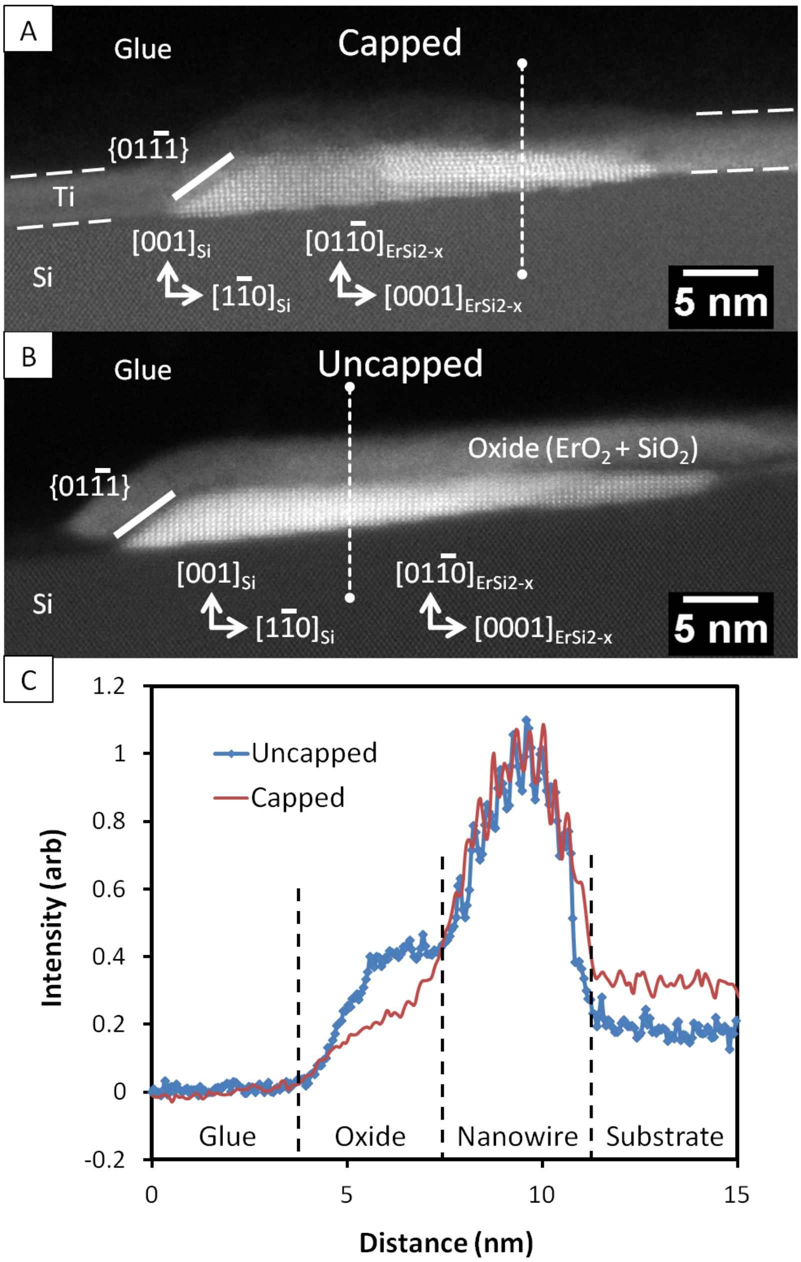

Figure 4.9: Images A and B show two similar $ErSi_2$ islands from a titanium capped sample (A) and an uncapped sample (B). The uncapped sample shows a bright oxide layer only above the silicide island, that has been shown to contain SiO_2 and Er from EELS analysis. In the Ti capped sample the capping layer is present as a continuous film across the whole sample and the presence of the oxide layer is greatly reduced. The dashed lines indicate the boundaries of the Ti layer. (C) shows two intensity line scans from the capped and uncapped samples, showing the reduction in intensity in the oxide region for the capped sample.

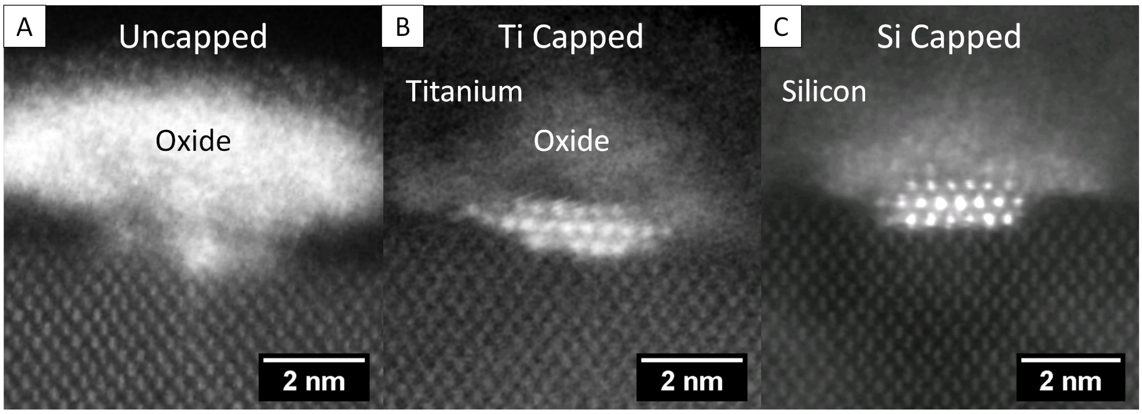

Figure 4.10: Three nanowires of approximately similar original size. The nanowire on the left was not capped and has been completely amorphised by the oxide layer. The middle nanowire was capped in titanium and has been protected from the oxide and still shows structure. The nanowire on the right was capped in silicon and in this case there is some oxide still present, however the oxide layer is much thinner than the titanium case. In general silicon capping gave the best protection.

The intensity profiles shown in Fig. 4.9 ‘C’ of the intensity across the islands shown in Fig. 4.9 ‘A’ & ‘B’ show the effect of the titanium capping. The uncapped island shows a characteristic bright shoulder on the intensity profile in the ’oxide’ region. The capped sample has a much smaller, less intense shoulder before the nanowire that corresponds to the titanium layer. The absence of the bright shoulder shows that the oxide has been effectively reduced. This is also observable from the images as the Ti capped sample does not have the bright amorphous structure just above the island.

The larger nanowires appear to be well protected by the capping layer, but the smaller nanowires show a greater degree of oxidation in both titanium and silicon capped samples. An example of three similarly sized nanowires are shown in Fig. 4.10. Here an oxide layer of approximately 2-3nm is observed above the titanium capped nanowire, where an oxide layer of approximately 1-2nm is observed above the silicon capped nanowire. When compared to Fig. 4.10(A) it can be seen that the capping has protected the small nanowire and preserved the structure.

Beam sensitivity

It was observed that samples that were capped in titanium were more sensitive to beam damage than samples capped in silicon. Successive scans of one nanowire on a titanium capped sample would quickly lead to the nanowire amorphizing, where on the silicon capped samples the nanowires were found to be much more stable, Fig. 4.11 compares the beam damage rates between an uncapped sample and a silicon capped sample. The nanowires are observed to react from the top down, where the nanowire is in contact with the titanium or oxide layer, which could be attributed to the electron beam driving a reaction between the silicide nanowire and the oxygen or titanium in the covering layer. After just 4 scans the nanowire in the Ti capped sample has almost been completely amorphized, where the Si capped nanowire survives 9 scans with no apparent change to the structure. The observation that the silicon capped nanowires are more resilient to beam damage and that the titanium or uncapped nanowires do not amorphize at the interface, indicates that the knock on beam damage is negligible.

4.5 Conclusions

We have shown that titanium or silicon capping does not seem to affect the morphology of ErSi_{2-x} nanostructures, as similar features were observed in titanium capped, silicon capped and non-capped samples. Smaller nanowires appear to be more susceptible to oxidation than larger islands as a greater degree of oxidation was observed on smaller wires than larger islands. Silicon capping is technically easier to achieve using the methods that were available and provides better protection as well as reducing the beam sensitivity of the nanowires when compared to titanium or uncapped samples.

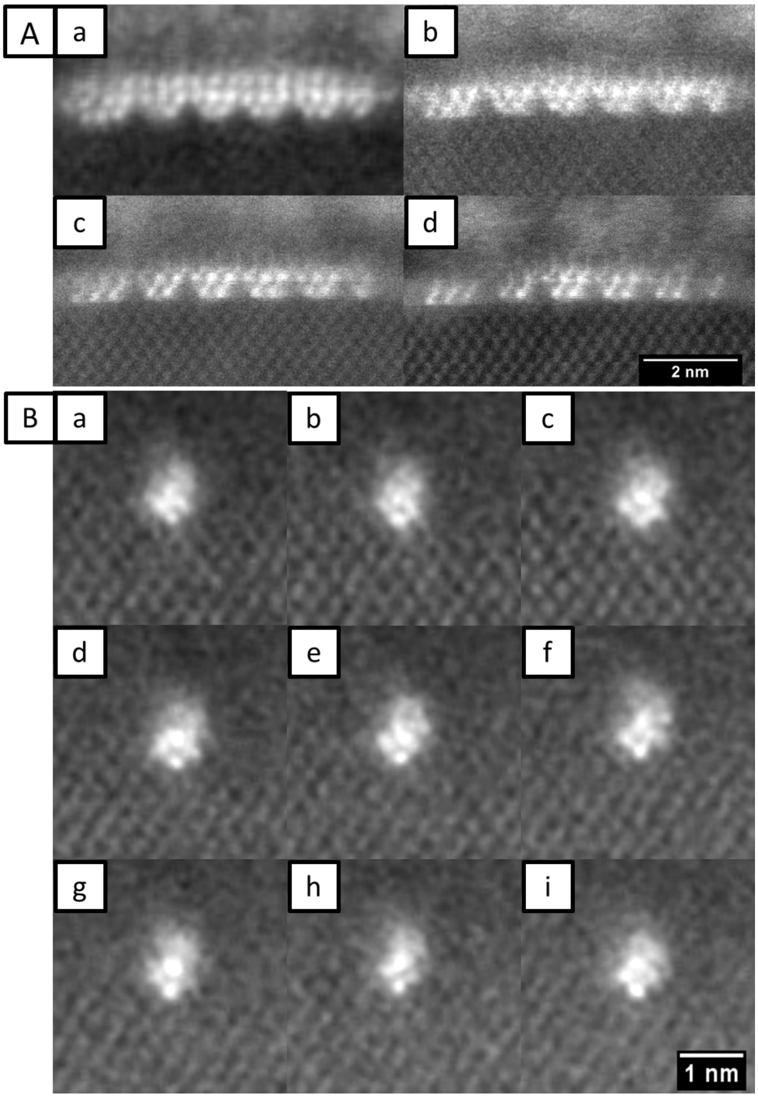

Figure 4.11: Two image series showing the difference between beam damage rates for uncapped samples (A) and silicon capped samples (B). Each image was taken in succession, however with (A) each image also corresponds to an increase in magnification and has been rescaled to match the first image, hence the improvement in image quality. In (A) we see a gradual loss of atomic columns at the nanowire / oxide boundary, whereas in the silicon capped sample the ultra-small nanowire shows no loss of structure even after 9 successive scans.

Chapter 5

The Structure of Ultra Small ErSi$_{2-x}$ Nanowires

5.1 Introduction

In this chapter we shall focus on the structure of ultra-small nanowires, i.e. nanowires less than 5nm in width, while using the larger better studied structures as a 'sanity check' for our results. The ultra-small structures have been deliberately singled out here as they were found to exhibit unusual structures that cannot be described using the accepted growth model and the associated assumptions. Here we shall investigate this unexpected structure and discuss the significance of the observed structure in terms of the accepted growth model. We shall show that the growth model suggested by Chen et. al. [12] adequately describes the larger hexagonal islands, however fails to describe the initial nucleation of these structures and the evolution of ultra-small nanowires.

5.1.1 Previous Work

Previous work on small nanowires has been quite limited. The smallest nanowires that have been analyzed with cross sectional techniques were reported by He et. al. [26]. In their paper they show one image of a dysprosium silicide nanowire that is less than 5nm in width and 5 atomic layers high which is shown in Fig. 5.1. However as the images were taken in HRTEM the structure at the interface of the nanowire is not resolved.

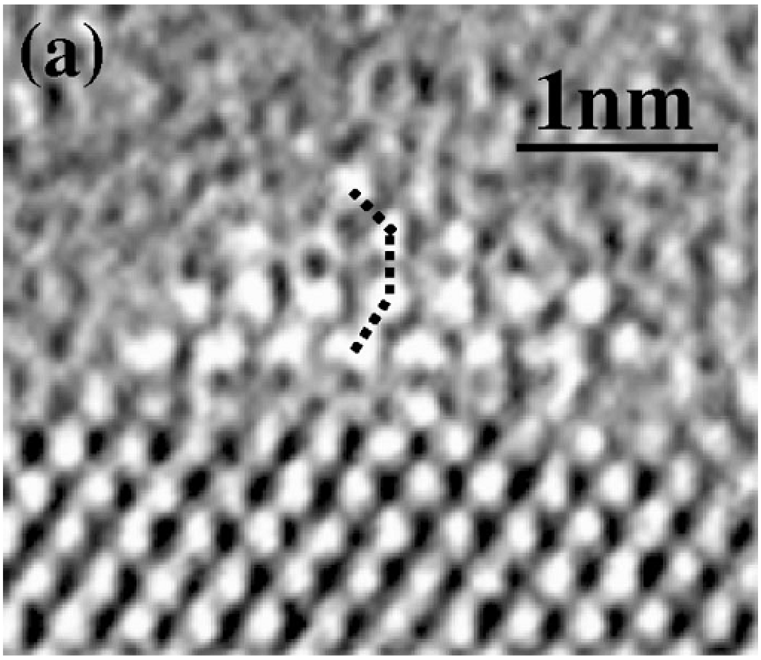

Figure 5.1: An image from He et. al.'s paper [26] showing a HRTEM image of a tetragonal nanowire 3.5nm in width and 5 layers high with an unresolved interface. The dashed lines highlight the tetragonal nature of this nanowire.

5.1.2 Experimental

The samples used for this investigation were grown using the same procedure as those used in the capping analysis. Thus all experimental set-ups and procedures are identical to those covered in Chapter 4.

5.2 Results

5.2.1 Evidence of a new orientation relationship

As previous stated in Chapter 4 our samples produced both small nanowires and large nanowires/islands. For the sake of this analysis a total of 218 separate structures were analyzed from 571 images. The observed structures were separated for the sake of the analysis into ultra-small nanowires of widths $\leq$ 5nm, nanowires 5-10nm and islands >10nm. The preferred structures for the ultra-small nanowire and island cases are shown in Fig. 5.2 and 5.4 respectively. There is no 'preferred structure' presented for the nanowire (5-10nm) case as this was found to be a transition region between the two regimes. Fig. 5.2 shows two orthogonal images of two separate ultra-small nanowires, taken from separate

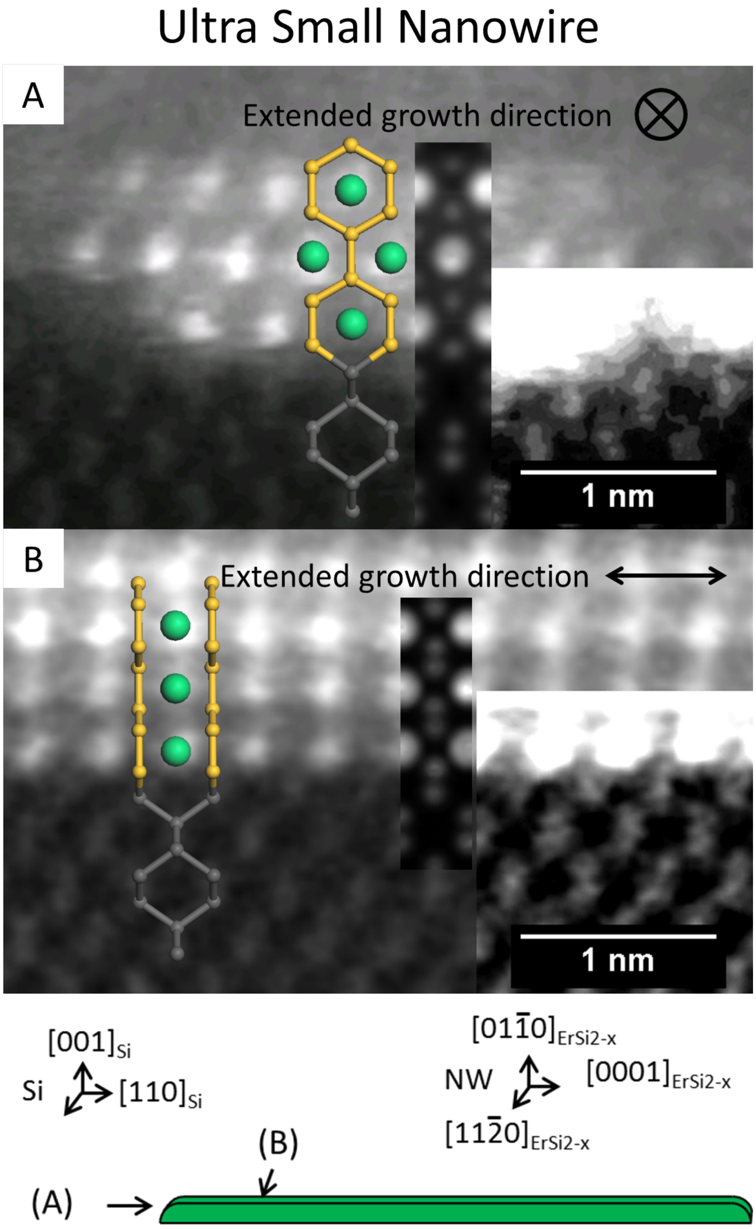

Figure 5.2: Two cross sectional STEM images of two separate but similar small nanowires showing the preferred structure of nanowires of 3 atoms in thickness and less than 5nm in width. (A) shows a hexagonal projection of the silicide, indicating that the c-axis is orientated along the viewing direction which in this case is along the nanowire length. (B) shows a rectangular projection which is representative of the hexagonal silicide with the c-axis perpendicular to the viewing direction. This particular nanowire was measured to be $\sim 1.3 \mu$m long, as shown in Fig. 5.3. The three insets in (A) and (B) show from left to right: (Left) The structure of the interface, where the gray and yellow indicate the silicon positions and the green the erbium. (Middle) A simulated STEM image using the crystal structure shown on the left. (Right) A section of the image that has had its contrast and brightness altered to better show the silicon structure.

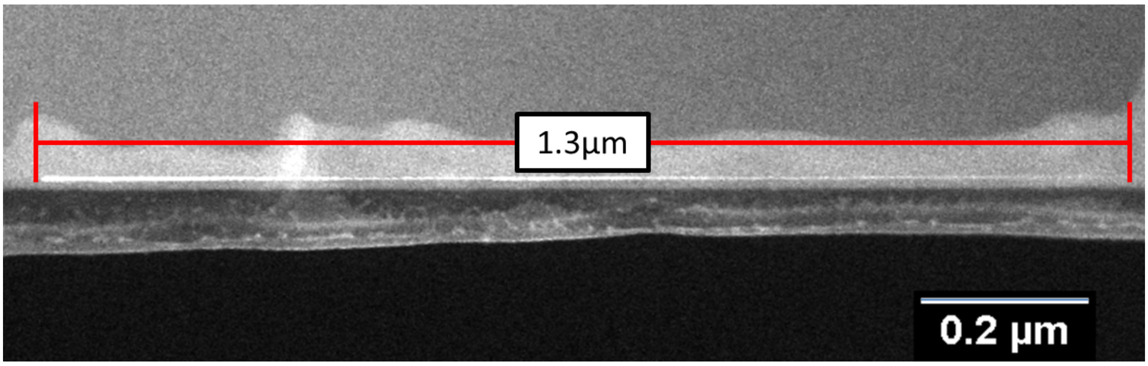

Figure 5.3: A low magnification cross sectional STEM view of the nanowire shown in Fig. 5.2(B) showing that the nanowire is $\sim 1.3\mu$m long

samples that were grown at similar conditions. The nanowires are hexagonal with their c-axis orientated along the direction of extended growth. The overlays in Fig. 5.2(A) show a structure model for the hexagonal silicide in projection along the $[0001]_{ErSi_{2-x}}$ direction alongside a HAADF STEM simulation produced using this structural description. The overlays in Fig. 5.2(B) show a structure model of the hexagonal silicide viewed along the $[11\bar{2}0]_{ErSi_{2-x}}$ direction and an associated HAADF STEM simulation. The overlays match well with the STEM results indicating that the proposed structure is a good description. The nanowire in Fig. 5.2(B) was measured to be $\sim 1\mu$m long from low magnification images ensuring that it is a side view of a nanowire, this image is shown in Fig. 5.3.

This structure was found to be typical for nanowires of widths <5nm and is described by the orientation relationship:

$$(001)_{Si}/(01\bar{1}0)_{ErSi_{2-x}}, [110]_{Si}/[0001]_{ErSi_{2-x}} \tag{5.1}$$

As a comparison the expected orientation relationship that is currently accepted and was proposed by Chen et. al. is:

$$(001)_{Si}/(01\bar{1}0)_{RESi_{2-x}}, [110]_{Si}/[11\bar{2}0]_{RESi_{2-x}} \tag{5.2}$$

The difference between the two orientations is a 90° rotation of the silicide with respect to the Si(001) surface taking the c-axis of the hexagonal silicide from being perpendicular to the growth direction as described by Chen's strained growth model to parallel to the growth direction. We also present that data for larger structures (>20nm) for comparison and the observed structures are shown in Fig. 5.4. Hexagonal islands with the expected orientation relationship described by Equation (5.2) were observed coexisting with tetragonal islands, which is consistent with previous studies on features of this size [17].

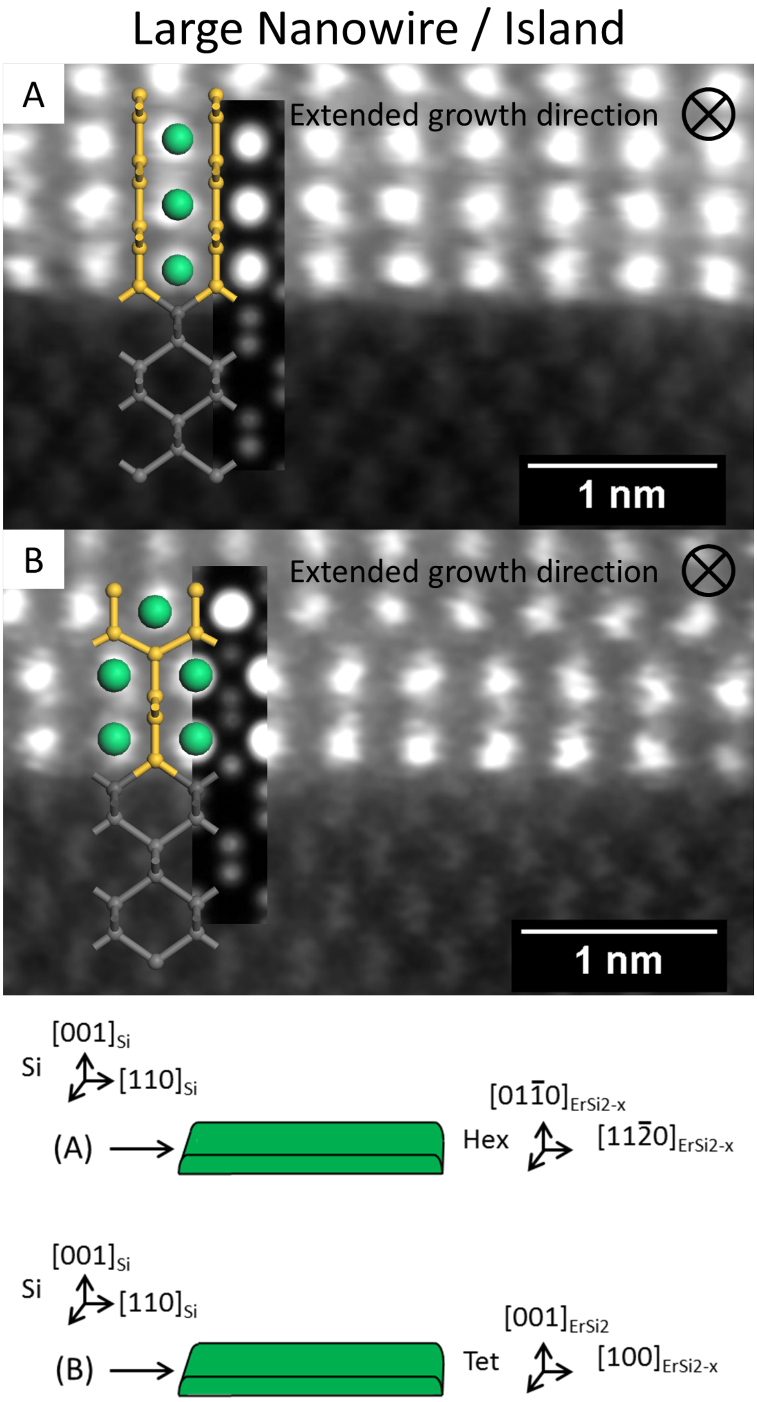

Figure 5.4: Two nanoislands showing the bulk hexagonal (A) and tetragonal (B) structures along their growth direction. The inserts show a structure model of the interface structure and associated HAADF STEM images simulations, the yellow and gray indicate silicon where the green indicates erbium.

5.2.2 Statistical Analysis

In order to find the statistical relevance of the new orientation relationship, every possible structure that can be generated just using the triangular subunit common to both the hexagonal and tetragonal silicides, described in Fig. 2.2, and the 90° rotation associated with it were generated up to a thickness of 4 atomic layers. The analysis was limited to 4 atomic layers as almost no nanowires of $<$5nm in width and 5 atomic layers thick were observed. The possible projections fall into 4 categories: (1) ‘2 atom’ which contains the two possible structures of two atoms in height, which cannot be labeled as hexagonal or tetragonal as the structure is common to both and we are not sensitive to the silicon to be able to distinguish using the silicon locations. However we can separate them into ‘triangular’ and ‘rectangular’ by looking at their projection along the direction of extended growth. A group for each of the pure (2) ‘hexagonal’ and (3) ‘tetragonal’ structures and a separate (4) ‘hybrid’ group, that contains features of both the hexagonal and tetragonal structures, while not being either. In total 14 different structures were generated using this method.

The observed structures of the nanowires were compared to the generated structures and the relative number of each were counted. All of the nanowires of $<$5nm in width and 5 atomic layers thick were well described by the generated structures. Some nanowires exhibited more than one structure across its width; however this is not entirely unexpected as the bundling of nanowires together to form larger wires is well documented [19], and interface steps or variation in thickness introduce extra structures. An example of nanowires bundling is shown in Fig. 5.5. The bundling of nanowires together will be discussed in greater detail in Chapter 6. The number of observed instances of each interface structure are shown in Fig. 5.6. If the strained growth correctly described the initial nucleation mechanism of these structures we would expect to see a preference for the structures highlighted in dashed orange in Fig. 5.6(a) as described by the orientation relationship in Equation (5.2). We observed an overwhelming preference for the group highlighted in blue with an orientation relationship as described by Equation (5.1).

The difference between the two orientation relationships is a rotation of 90 ° of the ErSi_{2-x} crystal with respect to the silicon substrate and therefore the direction of extended growth of the nanowire. The dashed orange group has the c-axis of the hexagonal silicide perpendicular to the extended growth direction, which is predicted by the strained growth

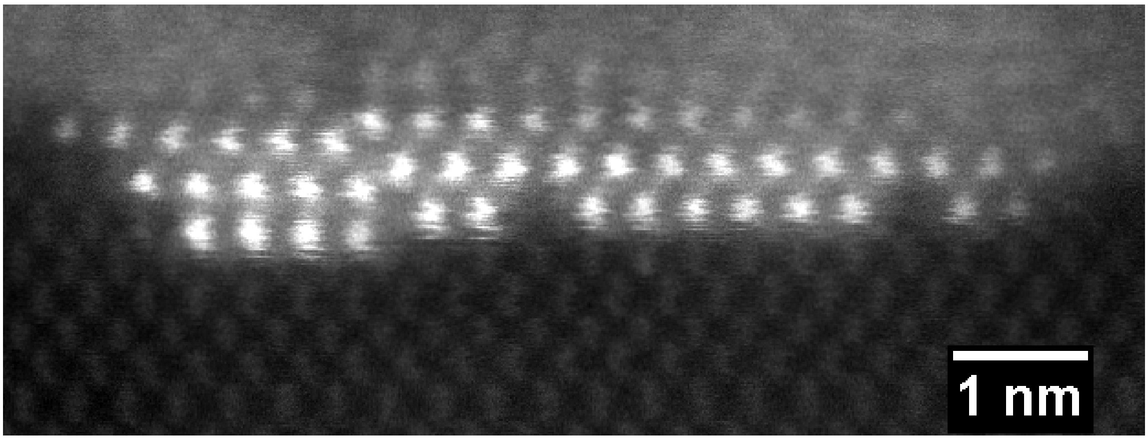

Figure 5.5: An example of nanowire bundling where two different structures are observed within one nanowire. In this case we have 'tetragonal like' structure on the left and 'parallel' structure on the right

model, whereas the blue group has the c-axis parallel to the growth direction. For future reference we shall use the relative orientation of the growth direction and the c-axis to distinguish the two hexagonal structures, the dashed orange group shall be referred to as 'perpendicular' and structures in the blue group shall be referred to as 'parallel'. We have included the 'rectangular' 2-atom group in 'perpendicular' and 'triangular' in 'parallel' as they are precursor phases of the respective groups.

5.3 Discussion

The analysis of the nanowires that were $\leq$ 5nm in width, showed a preference for the hexagonal structure over all other types with 60% of the structures that were three or more layers thick being hexagonal, 27% showing tetragonal structure and the remaining 13% falling into the hybrid group. The preference for hexagonal is predicted by the strained growth model, however of the 77 separate structures that were analysed only one nanowire showed the hexagonal structure with the expected perpendicular orentation relationship (Equation (5.2)), and 57 nanowires (74%) exhibited the unexpected parallel orientation relationship (Equation (5.1)).

As the size of the nanostructure increases the number of structures that have the unexpected parallel structure decreases rapidly. This implies that although strain is not the dominant factor describing the nucleation of the ultra-small nanowires it begins to dominate as the nanostructures increase in size. As the strain energy increases the nanostruc-

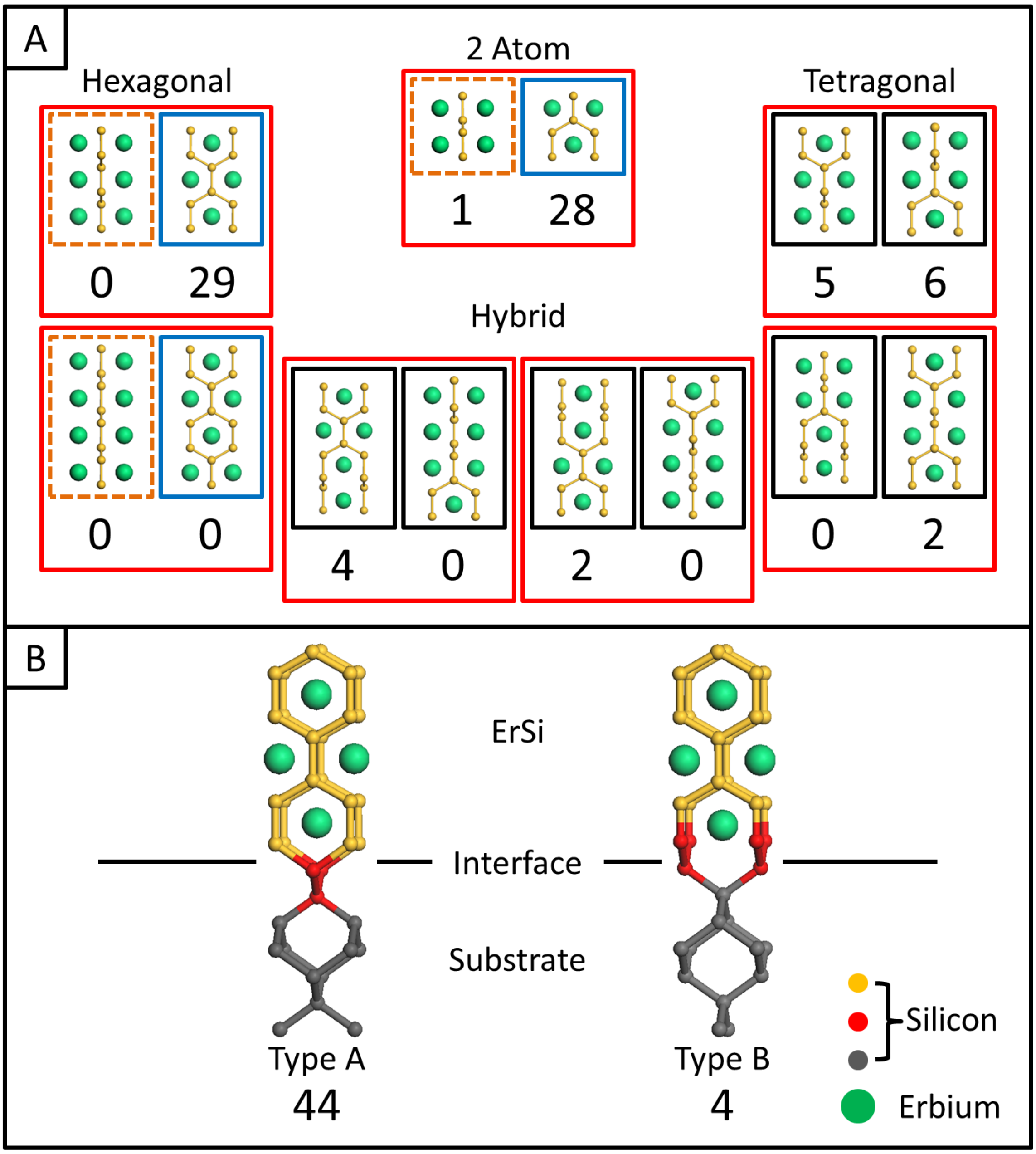

Figure 5.6: (A) The possible nanowire morphologies generated using the triangular subunit and the 90° rotational freedom associated with it. The different possibilities are grouped into 4 distinct groups: 2 atom, Hexagonal, Tetragonal and Hybrid. For simplicity only the Er positions are indicated by the green dots. The numbers show the number of observed counts for each interface for nanowires of <5nm in width. The red squares indicate that the pairs are 90 degree rotations of each other. The dashed orange boxes indicate the expected projections assuming the strained growth model. (B) The two possible Si terminations, the numbers indicate the number of observed cases of each. The blue group are discussed in the main text.

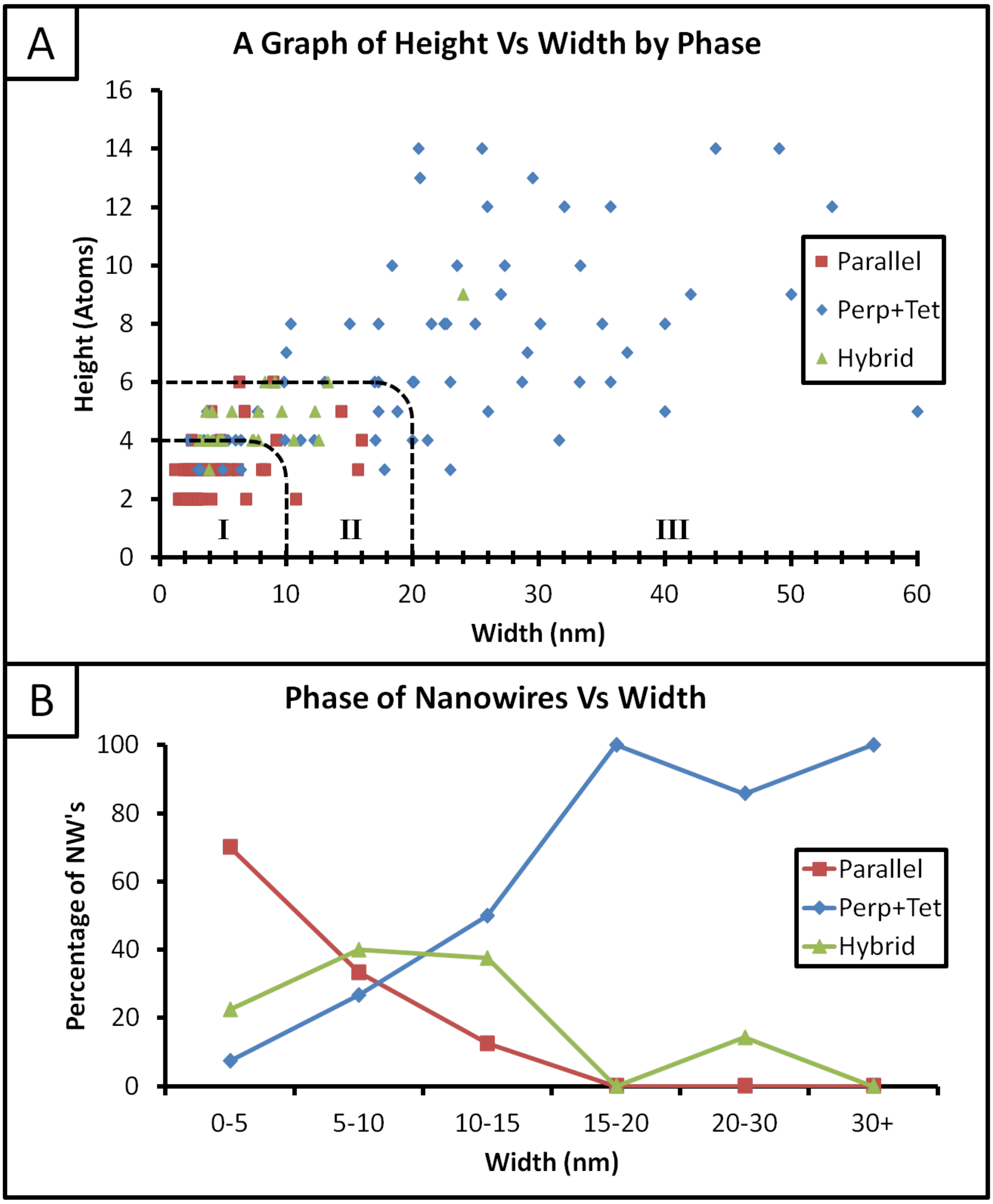

Figure 5.7: Two graphs that show how the phase of the nanowires changes with size. The 'Parallel' groups contains both the two atom triangular projection and the hexagonal silicides with their c-axis parallel to the direction of extended growth. The hybrid groups contains the nanowires that are defected or faulted making them impossible to classify into the bulk phases. Perp+Tet include hexagonal silicides with their c-axis perpendicular to the direction of extended growth, the 2 atom square projection and the tetragonal nanowires. Region III in (A) indicates where most experimental data has been published, II shows the limit of the experimental data, and in region I no experimental data to date has been published. (B) shows an alternate representation of (A) showing how the relative numbers of each type changes with width.

tures undergo a phase transformation to relieve this strain. Fig. 5.7 shows how the width of the nanowire affects the observed phase. As the size of the nanowire increases the ‘perpendicular’ structures quickly dominate, however at the 0-5nm range less than 10% (1 count) of the observed nanowires can be explained by the strained growth model. We can explain why this orientation relationship has so far gone unobserved, through analysis of Fig. 5.7(A). Region III from Fig. 5.7(A) gives an indication of where the majority of the experimental data so far has been obtained. In this region the vast majority of the nanowires are well explained by the conventional hexagonal orientation relationship and the bulk tetragonal phase. Region II indicates the limit of the data as obtained by He at. al. [26], here there is a large mix of ‘confused’ structures that are not well explained by the bulk hexagonal or tetragonal phases. As of yet no data has been presented from region I and it is within this region that the new orientation relationship dominates.

We were also able to look at the termination of the Si at the Si/ErSi$_{2-x}$ boundary. There are two possible terminations, the final Si dumbbell can either be directly underneath the interfacial Er column (as viewed along the direction of extended growth) or in between the Er columns, the two possible terminations are shown in Fig. 5.6(B). This analysis excludes all nanowires that had both terminations at their interfaces (10 counts), caused by steps at the interface or single steps. Fig. 5.2(A) gives an example of the preferred nanowire structure and ‘type a’ silicon termination. Even though our measurements are not sensitive to the silicon positions within the nanowire we are able to infer their most likely positions within the nanowire and have a reasonable estimate at their positions at the surface, even without DFT modeling. Fig. 5.8 shows a schematic of the preferred ultra-small nanowire structure (A) along the growth direction (B) perpendicular to the growth direction. (C) & (D) show how the more common c(2×2) surface reconstruction could form from this structure model. This c(2×2) surface reconstruction model is consistent with the work by Eames et. al. [16].

Previous models that have been proposed from STM measurements have all assumed strain induced growth and have enforced the orientation relationship as given by Equation (5.2). This then means that the c-axis of the hexagonal nanowire is perpendicular to the direction of extended growth, so in that respect our model is inconsistent with the previous models. However our model does allow us to explain some features observed in other STM work and does not seem to produce any features that are inconsistent with previous work. For example Liu and Nogami show STM images of dysprosium silicide nanowires

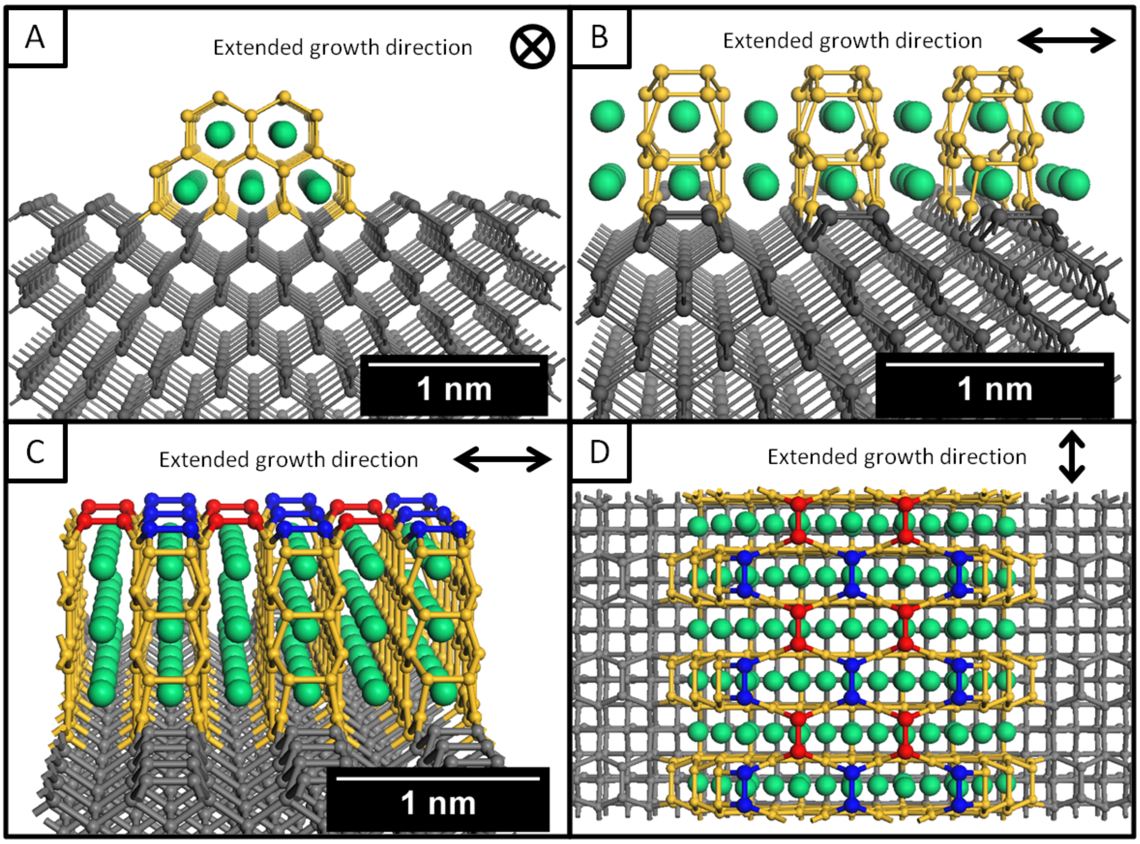

Figure 5.8: A schematic of a nanowire with the proposed orientation relationship. (A) & (B) show the same nanowire from two orthogonal directions. (C) & (D) show a larger nanowire highlighting how the common c(2 × 2) surface reconstruction could form, (C) showing a side view of the nanowire and (D) a top down view. In (A), (B), (C) & (D) gray indicates silicon in the substrate, yellow indicates silicon in the nanowire and green the erbium positions, where in (C) & (D) red and blue highlight the c(2 × 2) surface reconstruction.

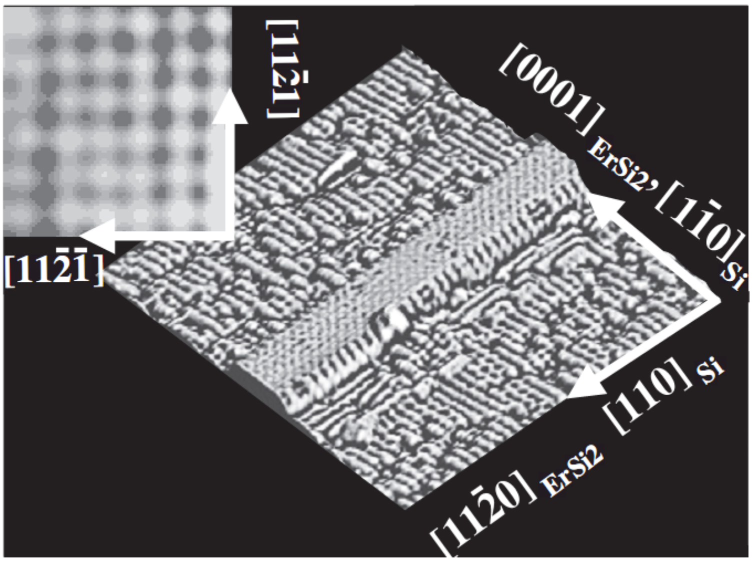

Figure 5.9: A high resolution STM image (25 nm×25 nm) from Chen et. al.'s paper [27], showing a nanowire with a c(2×2) surface reconstruction (inset (3 nm×3 nm)) and an edge reconstruction with periodicity 2a$_{Si}$.

in Fig. 7b of their paper [19], that show a surface modulation of length $2a_{Si}$ from region (II) and $1a_{Si}$ from region (III). These modulations can be explained easily in terms of the graphene like silicon layer separation within the ErSi$_{2-x}$ structure. At the nanowire surface the topmost silicon atoms would be free to dimerize as shown in Fig. 5.8(B), which would give the $2a_{Si}$ spacing observed by Liu and Nogami. If the dimerization did not occur the spacing would halve, which explains the $1a_{Si}$ periodicity. Our model is also able to adopt the more common c(2×2) surface reconstruction as shown in Fig. 5.8(C) which is also observed by Liu and Nogami in Fig. 7 (D), (E) and (F) of their paper.

We are also able to propose explanations for features that are not at the top surface of the nanowire. Chen et. al. [27] published an image of a nanowire, which has a periodic structure apparent on the side wall of the nanowire with a periodicity of $2a_{Si}$. Fig. 5.9 shows the image. This periodicity can be explained in terms of a dimer row forming up the side of the nanowire as shown in Fig. 5.8(B).

The stability of this new orientation relationship does pose some interesting questions. According to conventional epitaxial growth theory it should not exist, the nanowire is existing in a highly strained configuration. We are unlikely to be able to explain the orientation in terms of compressibility as preliminary structurally optimized CASTEP calculations on the hexagonal ErSi$_2$ unit cell show that the change in energy of the unit cell resulting in a compression of the c-axis to 3.84Å results in an energy increase of 0.04951eV, where an expansion of the a-axis to 3.48Å results in an energy increase of 0.00604eV. More detailed calculations on a $ErSi_{2-x}$ $2\times2\times2$ supercell with a vacancy ordering of 2C were attempted but did not complete within time constraints.

There have been previous DFT calculations that have suggested that the accepted 'strained growth' orientation relationship is not the lowest in energy configuration for rare earth silicide nanowires on the Si(001) surface. Eames et. al. found that the lowest energy configuration was a 'tetragonal' nanowire parallel with the Si dimer rows [16]. In this paper Eames et. al. have differentiated hexagonal and tetragonal at the 1 RE atom level by using the surface reconstruction of the silicon at the top of the nanowire. Their tetragonal model could equally be considered to be a hexagonal nanowire with its orientation relationship as described by Equation (5.1), the parallel orientation, which only differs from what we observe at the nanowire / silicon interface, in that their model has a b-type interface rather than the a-type that was observed to be preferred.

If we assume that all nanowires nucleate with this unexpected orientation relationship as described by Equation (5.1) there must be some mechanism to transform from the 'parallel' hexagonal orientation relationship to the 'perpendicular' and tetragonal phases. A possible mechanism for transforming the nanowire between phases is shown in Fig. 5.10. The image shows a vacancy defect that could progress across the width of the nanowire allowing the nanowire to transform from the edge across. This transformation would require the erbium atom to move both along the width of the nanowire and along the length of the nanowire. The silicon network would also require rearrangement however this would be made easier by the large number of vacancies within the silicon network.

He et. al. in their paper [26], indicate that the morphology that they observe for $DySi_2$ nanowires is hexagonal in the expected orientation (Equation (5.2)) at the interface with a 'faulted' tetragonal like layer on top. In the '$\sim$10' nanowires that they analyse not one nanowire exhibited the opposite. The growth method that they used was different from ours in that it was hotter and shorter. However if their result is reproducible it implies that different growth conditions or different rare earth metals will produce different nanowire structures. This has many different implications for this field. Firstly DFT work in this area has generally used Y as a substitute for the rare earth metal as it is less computationally expensive. If it can be shown that the choice of rare earth metal is affecting the structure rather than the growth conditions, this substitution may not be valid. Secondly if different ultra-small nanowire structures are obtainable through different growth conditions or rare

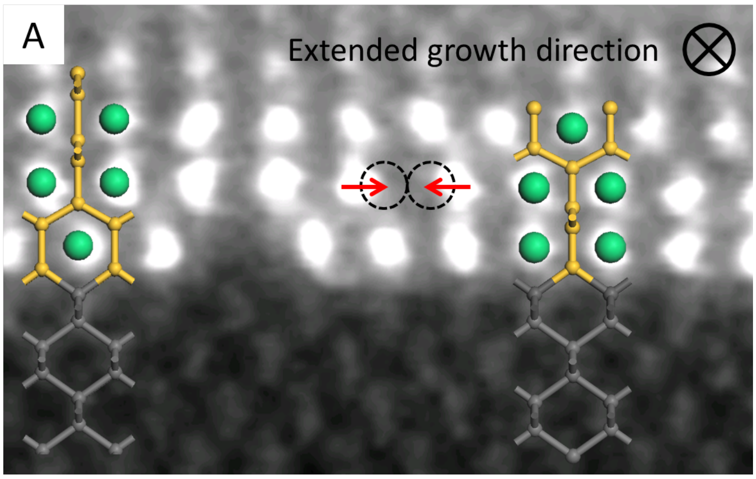

Figure 5.10: An image of a larger nanowire displaying a defect that could be an indication that the nanowire is undergoing a transformation of phases. The black circle and red arrow indicate the possible movement of erbium atoms

earth metals this opens up the possibility of tuning the structural and electronic properties through the use of different rare earth metals or even intermixing of different metals.

5.4 Conclusions

We have shown that the preferred ErSi_{2-x} morphology for nanowires less than 5nm in width is hexagonal with the c-axis aligned along the direction of extended growth. On the vicinial Si(001) surface the preferred silicon interface termination for nanowires $\leq$ 5nm in width is ‘a-type’ as defined if Fig. 5.6. A possible structure model for the observed morphologies of the nanowires is shown in Fig. 5.8.

We have shown that the accepted growth model fails to explain the structure of the ultra-small ErSi_{2-x}. The preferred structure of the ErSi_{2-x} is hexagonal with the c-axis aligned along the direction of extended growth with a preference for the final Si dumbbell to be directly underneath the interfacial Er column. The results imply that strain is not the dominant factor in the formation of the ultra-small nanowires. The existence of larger islands on the same sample with the expected orientation shows that as the nanowires evolve into islands, strain becomes the dominant factor and the islands reorganize their structure to compensate the strain build up. The reason that this structure has not been previously observed is attributed to the fact that previous studies have not analysed structures in this size range and that the new orientation does not survive as the nanowire size increases.

Our structure model is able to describe some of the periodic features from previous work that have so far been unexplained in terms of the atomic structure and known dimerization mechanisms, and is fully consistent with previous work.

Our results also show that there is a critical width for the unexpected ‘parallel’ structure, as no nanowires of widths $<$15nm were observed with the parallel structure, suggesting that there is a cutoff in the 10-15nm region, which is quite probably due to increasing strain in the nanowire. We have observed nanowires that have defects within their crystal structure hinting at a method for the transformation of one phase into another, Fig. 5.10 shows such a nanowire. This suggests that the transformation occurs from the edge and progresses across the nanowire laterally.

The work of Eames et. al. [16] provides a possible explanation for the observed orientation relationship of the ultra-small nanowires. In their work they found that on the clean dimerized Si(001) surface the ‘tetragonal’ structure was lower in energy than the ‘hexagonal’ structure, regardless of the dimer row direction. However their ‘tetragonal’ structure can be described in terms of a hexagonal structure with its c-axis parallel to the growth direction, which is what we observe as the preferred structure for ultra-small nanowires. This implies that the observed orientation relationship is lower in energy than the accepted strained growth orientation relationship. Eames et. al. note in their paper [16] that the surface reconstruction of the hexagonal nanowire does not form the c(2×2) which is more commonly observed in STM, where their ‘tetragonal’ nanowire does, so they conclude that most nanowires are tetragonally capped. However our results indicate that instead of the surface being tetragonally capped the whole nanowire has the parallel structure. The fact that the ‘parallel’ structure is able to access the c(2×2) surface reconstruction and that the ‘perpendicular’ structure was not able to may indicate that the surface reconstruction may be the reason for the preference for the ‘parallel’ structure.

Chapter 6

The Structure and Interface Structure of ErSi$_{2-x}$ Nanostructures on Vicinal Si(001)

6.1 Introduction

This chapter focuses on the structure and interface structure of the larger ErSi$_{2-x}$ nanostructures on vicinal Si(001), focusing on the interface structure. Where possible we shall investigate how the ultra-small nanostructures evolve into larger islands. Although this system has been well studied by high resolution transmission electron microscopy techniques, the interfaces of these systems have not resolved in most of the previous studies [26]. We shall investigate the structure of this critical region using Aberration Corrected Scanning Transmission Electron Microscopy (AC-STEM) and discuss the observations where relevant in terms of the result discussed in Chapter 5. Due to the rather fragmented nature of this chapter the results and discussion will be presented at the same time.

Using AC-STEM will allow us to access detail that was not obtainable with conventional HRTEM, allowing us to directly image the structure of the interface at atomic resolution. We will be able to make direct comparisons between the data and models to give an accurate description of the structure and interface structure.

The interfaces of these systems is of technological importance as the Schottky barrier characteristics of a system can be dominated by the interface structure. In NiSi$_2$ Tung et. al. found that a rotation of the overlayer by 180° alters the Schottky barrier by 0.14eV. The ErSi$_{2-x}$ nanostructures could find potential applications as an interconnect in future electronic devices, due to their extreme aspect ratios and conductivity, or as Schottky contacts for spin injection in spintronic devices due to their unique Schottky characteristics. In order for this to be achieved the Schottky barrier characteristics of the $ErSi_{2-x}$ nanostructures need to be known, and correlated to a structure that can be reliably reproduced. This may allow the tuning of the Schottky barrier, if the interface structure or bulk structure can be controlled through the growth conditions.

Here we start the process by detailing the various interface structures that the $ErSi_{2-x}$ system is observed to adopt, and compare our observations with previous models.

6.1.1 Previous Work

The previous work in this area has already been well covered in chapter 2, so only the directly relevant information shall be presented within each section.

6.1.2 Experimental

The samples used for this investigation were the same used for the analysis of ultra-small nanowires. Thus all experimental set-ups and procedures are identical to those covered in Chapter 5.

6.2 Results and Discussion

6.2.1 Island Growth

STM measurements have observed that around large islands there can be a large depression in the surrounding silicon, suggesting that the nanowire has eaten down into the substrate. An example from Liu et. al.'s paper [28] is shown in Fig. 6.1. This implies that the nanostructures could be growing down into the substrate as well as consuming silicon laterally. Chen et. al. however reported that they did not observe any 'detectable protrusion of the nanowires below the Si(001) surface' [12] from HRTEM data, however no images were published. If the nanowires are growing down into the substrate, rather than sitting on top this should be easy to spot from our high resolution cross sectional images.

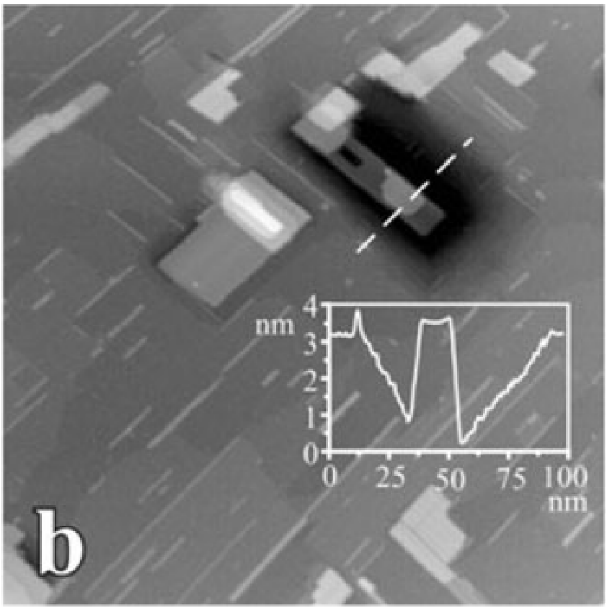

Figure 6.1: An image from Liu et. al.'s paper [28] showing the depression in the silicon around a large island. The dotted line indicates the location for the line scan. The image is 300nm × 300nm.

Islands and nanowires were grouped into three categories, proud, indent and rectangular depending if the nanostructures appeared to be growing on top of the silicon surface, into the silicon surface or neither, a combination of both. The different criteria used are displayed in Fig. 6.2(b). The number of nanowires displaying each growth mode was counted as a function of width. The percentage results are shown in Fig. 6.2

We observed that as the width of the nanostructures increased the number that showed no level of growing down into the substrate decreased. The number of nanowires that were completely submerged stayed constant at $\sim$10%. This implies that the nanostructures do grow down into the substrate, although slowly. If there was no transport of erbium down into the silicide we would expect to find that the relative numbers of the 'indent', 'proud' and 'both' would stay relatively constant as width increases. We would expect some counts in 'indent' and 'both' as STM measurements have shown the nanowires grow into terrace edges and burrow into them [19, 27, 147].

6.2.2 Interface Layer Brightness

It was noticed that often the erbium columns at the top and bottom of the nanostructure are dimmer than the columns within the bulk. This is shown in Fig 6.3, a line scan across a nanoisland shows decreased intensity for the Er columns at the interface and the surface

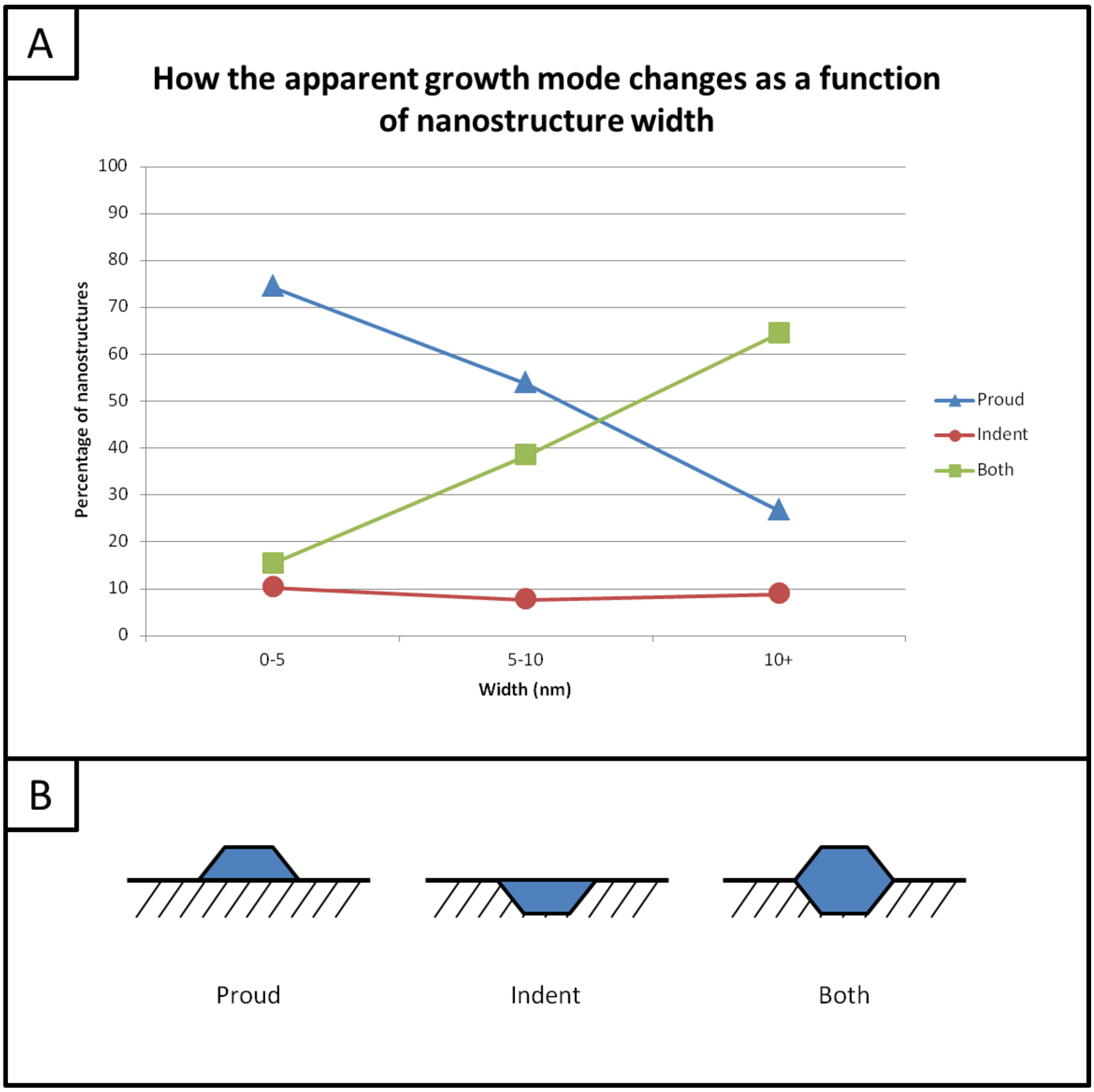

Figure 6.2: (A) How the apparent growth mode of the nanostructures changes with width. Blue triangles - proud, green squares - indent, red circles - both. (B) the criteria used to determine if the nanowire was ‘proud’ ‘indent’ or ‘both’.

of the nanowire.

A loss of intensity for columns at the top of the nanowire are easy to explain in terms of oxidation or incomplete columns, which are often observed in STM as top layer patches on the surfaces of the nanostructures. An example image from Wanke et. al.'s paper [29] is shown in Fig. 6.4(A), showing second layer growth (highlighted by the red oval) of a dysprosium silicide nanowire which was grown at similar temperatures to our samples.

The loss of intensity at the interfacial columns is more difficult to explain from only one projection. By looking at images perpendicular to the direction of extended growth we are able to attribute the dimming of the interfacial layer to defects in the interface layer along the growth direction. Fig. 6.4(B)&(C) show two cross sectional STEM images obtained during this work showing the observed defects, Fig. 6.4(B) shows two defects where the Er column has been shifted from its bulk position, and a vacancy at the interfacial layer. These vacancies could be enough to break the electron channeling condition and reduce the brightness of the interfacial layer. Fig. 6.4(C) shows where the bottom most Er layer is incomplete. A reduction in the number of atoms in the column will definitely give a reduced signal.

6.2.3 Nanowire Bundling

As mentioned in Chapter 5 we have observed nanowires that appear to show the effects of bundling. The growth of large islands is thought to begin with the bundling of smaller nanowires into one larger structure [28, 148], and bundles of nanowires are often observed in STM measurements, an example of which from Liu et. al's [19] paper is shown in Fig. 6.5, Fig. 6.4(A) also shows bundled nanowires.

We have observed features in some small to medium sized nanowires that exhibit defects in the structure which we attribute to the fusing of bundled nanowires beginning to join. Two examples of this are shown in Fig. 6.6(A) & (B).

Fig. 6.6 shows two nanowires that have defects along their length, Fig. 6.6(A) shows a defect that appears to have formed when two nanowires from different terraces joined, resulting in a different height either side of the defect. Fig. 6.6(B) shows three instances of this within one nanostructure where it appears as if four nanowires fused together.

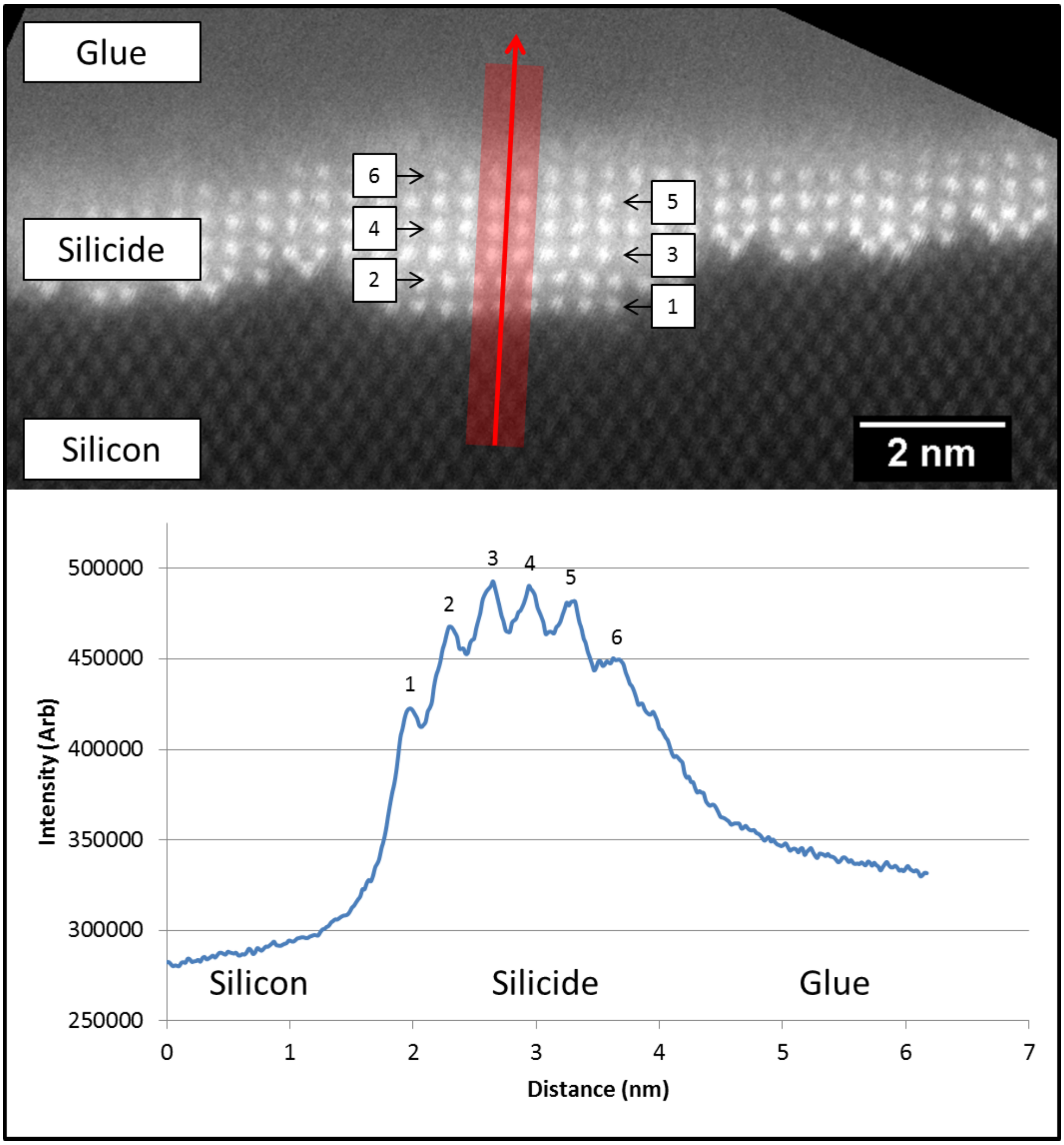

Figure 6.3: An image of a nanowire showing the reduction in intensity at the interface and top of the nanowire. The red line indicates the position of the intensity line scan, where the shaded area around the line indicates the area of influence. There is a decrease in intensity of ∼14% between layer 3 and 1.

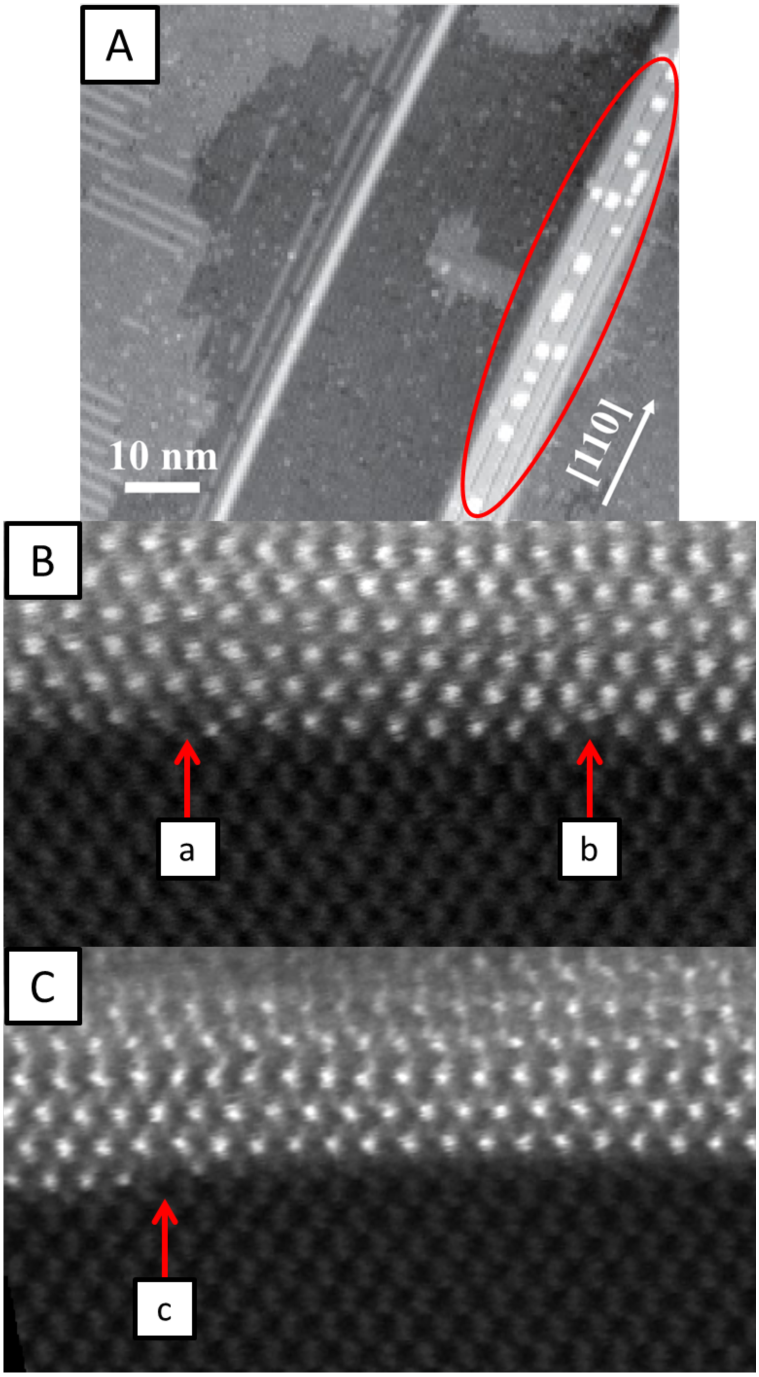

Figure 6.4: (A) An STM image from Wanke et. al.'s [29] paper showing second layer growth (highlighted by the red oval) on a dysprosium silicide nanowire, grown by post anneal at 600° C of 1Å of dysprosium. (B) & (C) Two cross sectional STEM images, not from Wanke et. al.'s paper, taken with the direction of extended growth perpendicular to the viewing direction. (B) shows two defects at the interface layer, (a) a vacant column, with the two erbium columns to the right of the vacancy shifted from their bulk positions (b) an Er column that has been shifted up into the silicide away from its bulk position. (C)(c) shows where the bottom-most Er layer finishes, leaving an incomplete column in the perpendicular direction.

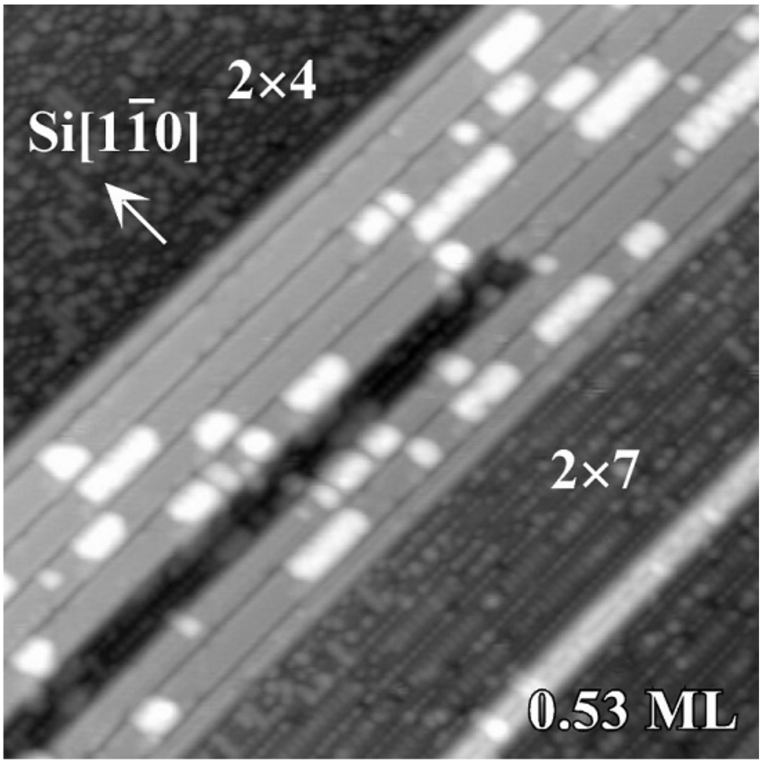

Figure 6.5: An example of smaller nanowires bundling to form larger structures for dysprosium silicide nanowires published by Liu et. al. [19]. The sample was grown by a hot deposit and post anneal method to a thickness of 0.53ML. The image was obtained at -1.2V over an area of 50nm × 50nm.

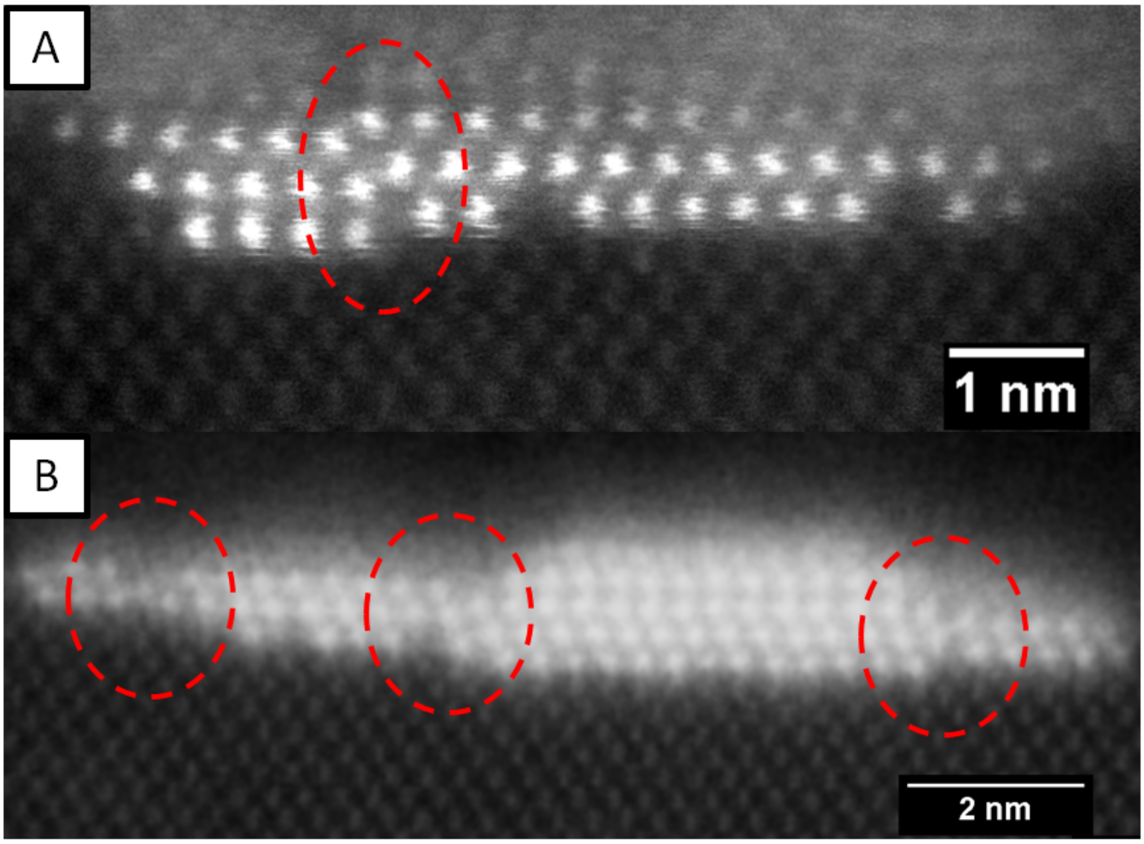

Figure 6.6: Two nanostructures that appear to show the effects of nanowire bundling. Both nanostructures show defects where it appears that nanowires have joined to form a larger structure. The defects are marked by red dashed ovals

The observation of the formation of bundles had previously caused some questions to be asked about the growth mechanism. The formation of bundles is not expected if the lattice match is so poor perpendicular to the growth direction [16], rather it would be expected that the strain associated with the poor lattice match would discourage nanowires from bundling together. This effect has been observed and well documented in other systems. The effect is strong enough to encourage self organization of quantum dots when grown on semiconductor surfaces [149, 150]. This dilemma can be solved using the observation of the new orientation relationship for ultra-small nanowires discussed in Chapter 5. As the c-axis of the nanowires has been shown to lie parallel to the direction of extended growth meaning that the low strain direction is perpendicular to the direction of extended growth and at a growth temperature of 600°C the lattice mismatch between the hexagonal silicide a-axis and the silicon substrate is -0.39%, meaning that there will be almost no strain field around the nanowires.

6.2.4 Strain Relaxation

The rare earth silicide nanostructures have previously been shown to be almost completely relaxed [26], here we detail the observed mechanisms through which this is achieved.

Double Stepped Interfaces

The stepped interface is not new, as it has been observed and described in terms of a strain reducing mechanism by Qiu et al [18]. This structure shall be referred to as a double step reconstruction as it requires the silicon substrate to form a double step underneath the nanostructure. This was originally encouraged by using a vicinal surface, so the steps are already there to be used by the nanowire. The optimal step width for strain reduction depends on the silicide mismatch and can be estimated by examining the bulk lattice parameters for the silicide and the silicon substrate. For Er the optimal periodicity was calculated to be $\sim$8 atoms (7.68 atoms) as the difference between the constrained silicide and the relaxed silicide is 0.25Å and the extra space introduced by the double step is 1.92Å. The 4° vicinal surface with double steps has an average step width of 7 atoms, which matches well with the erbium silicide optimal spacing. An example of this structure is shown alongside a graphical representation in Fig. 6.7.

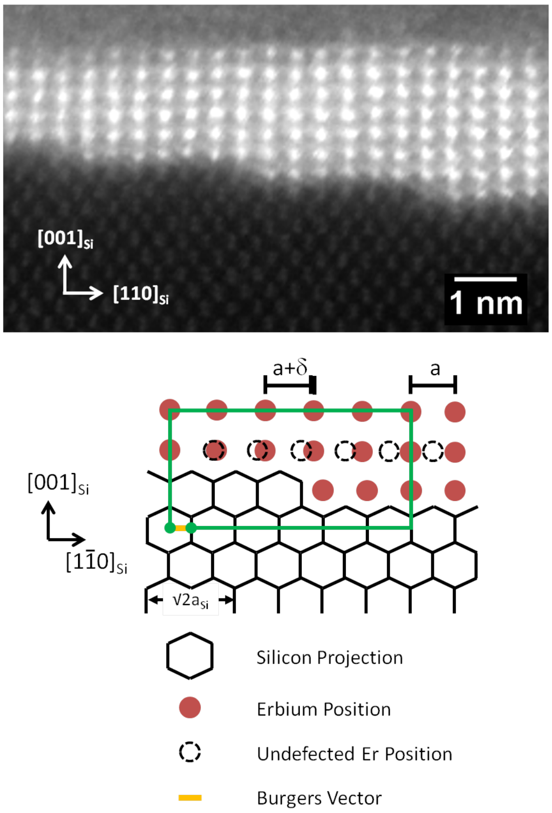

Figure 6.7: (Top) A large hexagonal silicide nanowire with its c-axis perpendicular to the direction of extended growth showing a step width of 7 atoms at the interface. (Bottom) A graphical representation of the step showing how it allows the silicide to relax.

Single Stepped Interfaces

This reconstruction has not been previously observed or predicted. This reconstruction occurs when the silicon substrate forms a single step underneath the nanowire, and is much less common than the double step alternative. An example of this interface is shown in Fig. 6.8. This could be due to the fact that large terraces are required in order not to encounter a double step at the edge of the terrace. As we are growing on vicinal surfaces these large flat areas are not common. Not only are these large flat terraces rare, this interface is higher in energy than the double step alternative, which is shown from the Burgers vector analysis of the two defects shown in Fig. 6.7 & 6.8. The single step structure has a larger Burgers vector of length $\frac{\sqrt{22}}{12}a_{Si}$ ($0.39a_{Si}$) in the $[3\bar{3}2]$ direction, compared to the shorter Burgers vector associated with the double step alternative of $\frac{\sqrt{2}}{4}a_{Si}$ ($0.35a_{Si}$) in the $[1\bar{1}0]_{Si}$ direction.

In the example in Fig. 6.8(a) the erbium silicide is almost completely relaxed with a lattice spacing of ~4.04±0.1Å as measured over 10 atomic columns, which is within experimental error of the bulk lattice parameter of 4.09Å. As the single stepped interface gives exactly the same extra space to relax into as the double step ($\frac{1}{2}$ silicon dumbbell spacing (1.92Å)), we expect the average step spacing to be the same in both the single step and double step cases. For the single step case, as the nanowire is dropping one Si atom down every 10 dumbbells (on average) we would expect to see a relative rotation of the silicide island of 2° toward the Si[$1\bar{1}0$] for a system that adopts this defect structure.

If we look at the single step defect in greater detail we note that the structure will only repeat every four steps. Fig. 6.9 shows a structure model of this system, the blue atoms are silicon that are in plane with the erbiums and red are silicon atoms that are out of plane with the erbiums. As the structure progresses down the second step the silicons are now directly beneath the erbium atom, which would be a highly strained arrangement. Either these steps are much shorter than the previous, or the single step could be followed by a double step to avoid the in plane silicon atoms. This double step immediately after the single step was observed and is shown at the top of Fig. 6.9.

In Fig. 6.9(A) we cannot say with any certainty that the silicon columns that have been highlighted in blue and red are definitely in and out of plane with the erbium atoms, as we do not have a 3D image of this structure. However the model proposed in Fig. 6.9(B)&(C) shows that any other arrangement will result in erbium and silicon atoms ending up unrealistically close together.

6.2.5 Triangular ErSi$_{2-x}$ Interface Projection

We also observe a tendency for nanostructures to have a triangular projection of the Er columns at the interface with the silicon substrate. The ‘triangular’ structure is described in Fig. 2.2 in Chapter 2. This was shown in the example of the single stepped interface in Fig. 6.8. This feature was observed in all sizes of nanowires, but as the size of the nanowire increases, the percentage of the nanowires exhibiting the triangular interface projection decreases. This trend is shown in the bar chart in Fig. 6.10. This indicates as the nanowires get larger the strain associated with the increasing size is having an effect on the interface structure, possibly by the introduction of interface steps. Or the nanowires that are larger have had longer to stabilize their interfaces into a lower energy configuration.

This structure has been observed before, where in the thulium silicide system the orthorhombic structure was observed to exist at the interface with the hexagonal silicide on

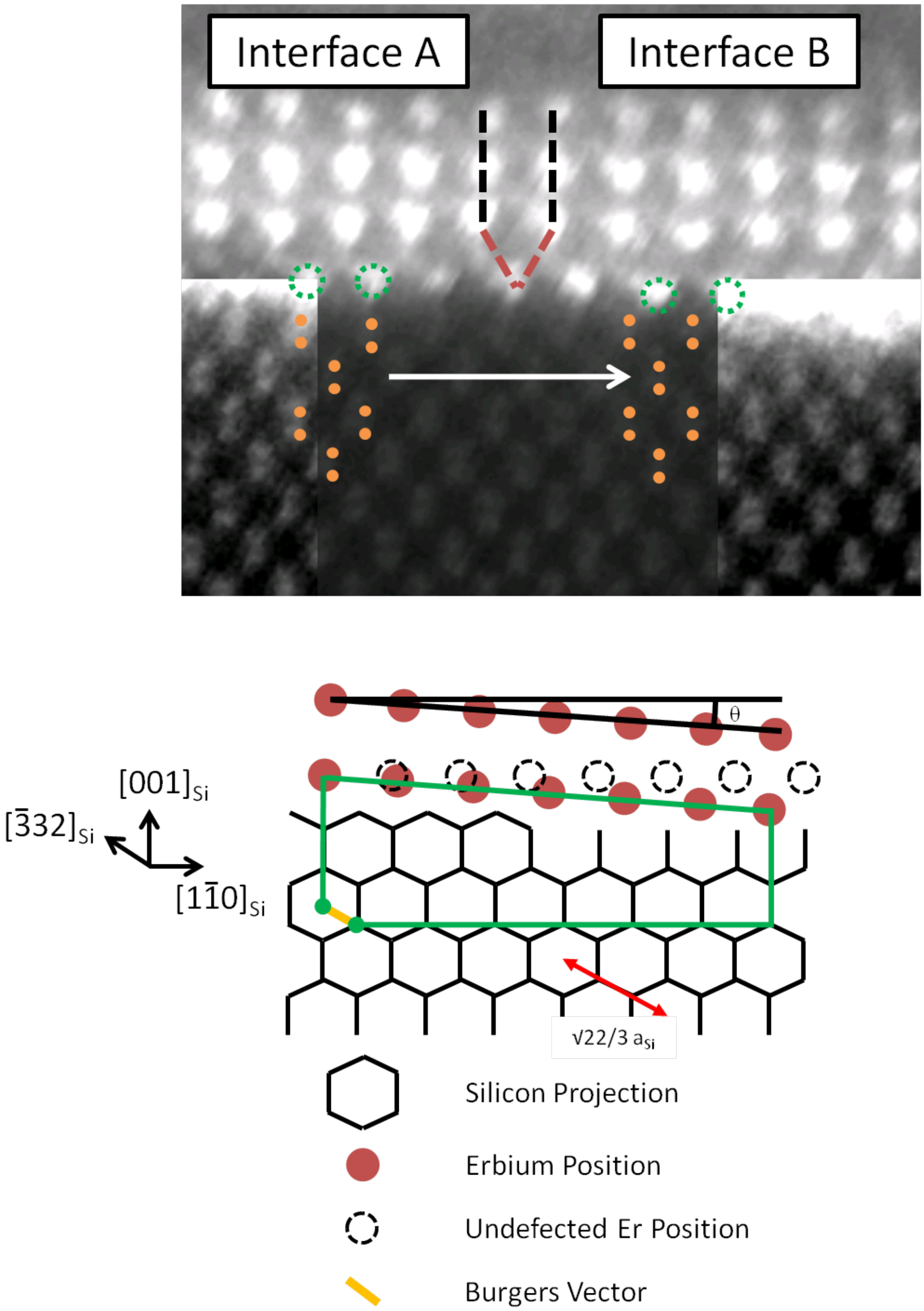

Figure 6.8: (A) A STEM image of an island showing an example of a single step interface allowing strain relaxation within the overlayer. (B) A model showing the structure of the single step and the associated Burgers vector of $\frac{\sqrt{22}}{12}a_{Si}$.

top. The existence of this biphasic silicide was attributed to a mechanism for strain accommodation at the interface with the substrate [97]. We are able to examine this possibility using our data. It was observed that as the nanowire size and therefore strain increases the number of nanowires exhibiting this interface defect decreases. In the simplest case, if this were a strain reduction mechanism we would expect a positive correlation.

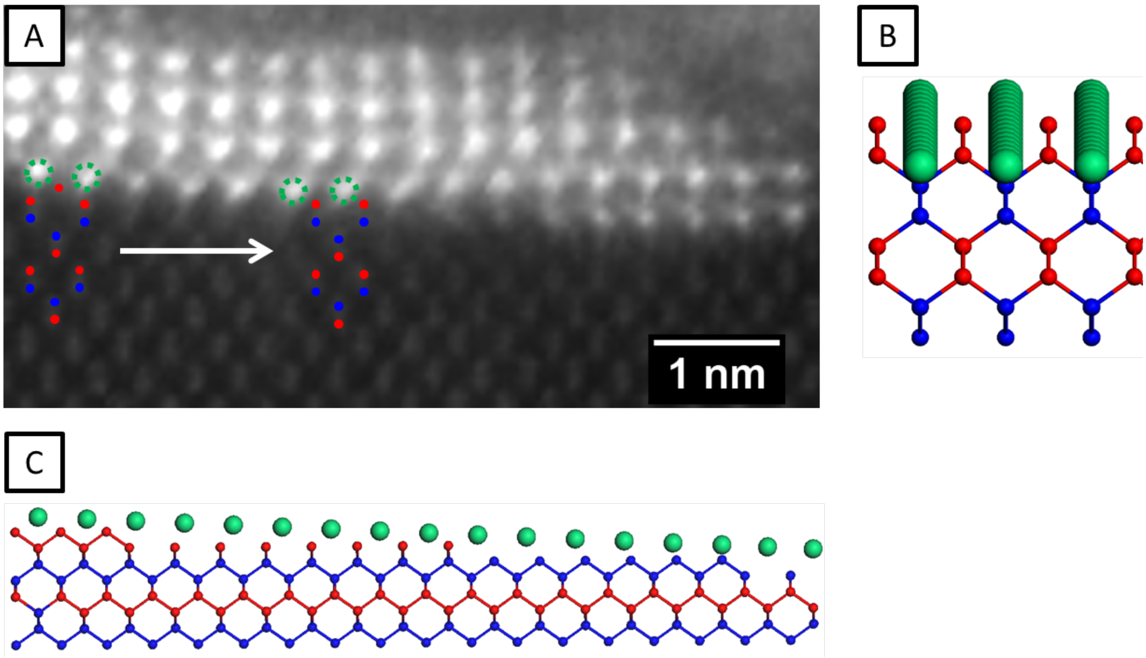

Figure 6.9: (A) The example of the single stepped nanowire showing a double step at the right hand edge immediately after the single step. (B)&(C)Two projections of a structural model of the single step defect. The blue and red indicate silicon atoms, where blue is in plane with the erbium atoms (green), and red is out of plane. From left to right: After a single step it is unlikely that another will directly follow as this would bring the erbium atoms unrealistically close to the silicon atoms that are in plane. It seems more likely that a double step would form after the single step to avoid this.

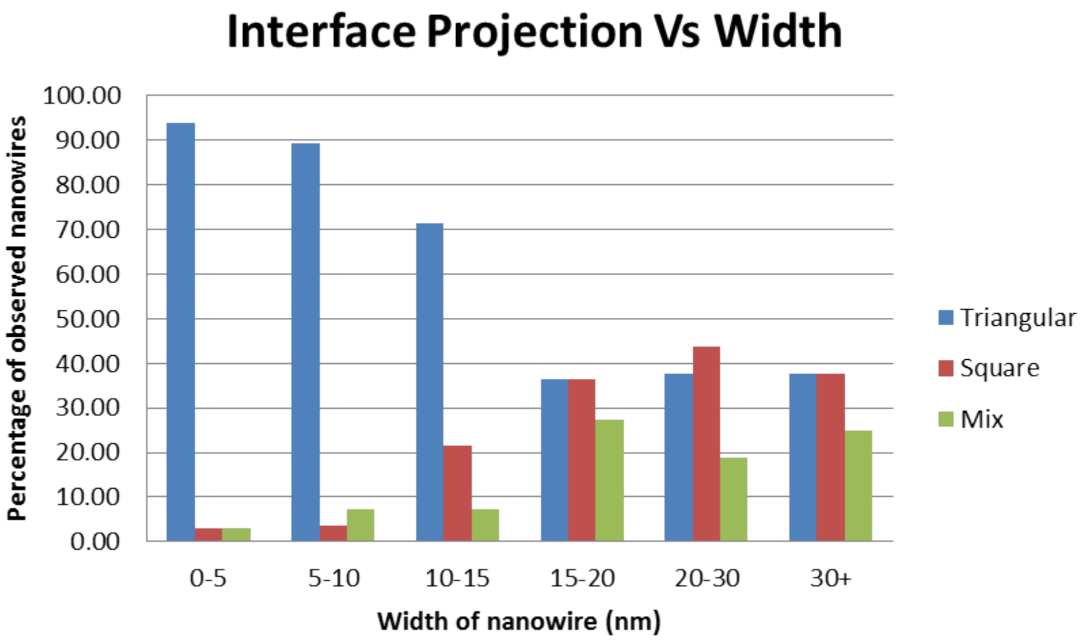

Figure 6.10: A chart showing how the number of nanostructures that exhibit the defected interface varies with width. Blue indicates interfaces that are completely defected, red interfaces that show no defect and green indicates that both areas of defect and no defect are present.

We can also examine this structure in terms of the new orientation relationship for ultra-small nanowires. Using the new orientation relationship we can explain the preference for ultra-small nanowires to have a triangular projection at the interface as this results from the parallel structure. However the existence of the triangular projection in larger islands cannot be explained this way. This structure is unlikely to be a leftover unreconstructed remnant of the parallel structure as the larger structures only exhibit one layer of the triangular projection, indicating that the layers above this have already been reconstructed. In some cases of tetragonal nanoislands there have been extra planes inserted in order to bring the triangular projection to the interface as shown in Fig. 6.11. This implies that the triangular projection at the interface is energetically favorable, the negative correlation between size and structure size can be explained if the triangular projection is a competing strain reduction mechanism with the double stepped interface. As the nanostructure becomes larger it is more likely to encounter a double step on the Si(001) surface, increasing the number of islands that have double steps at their interface.

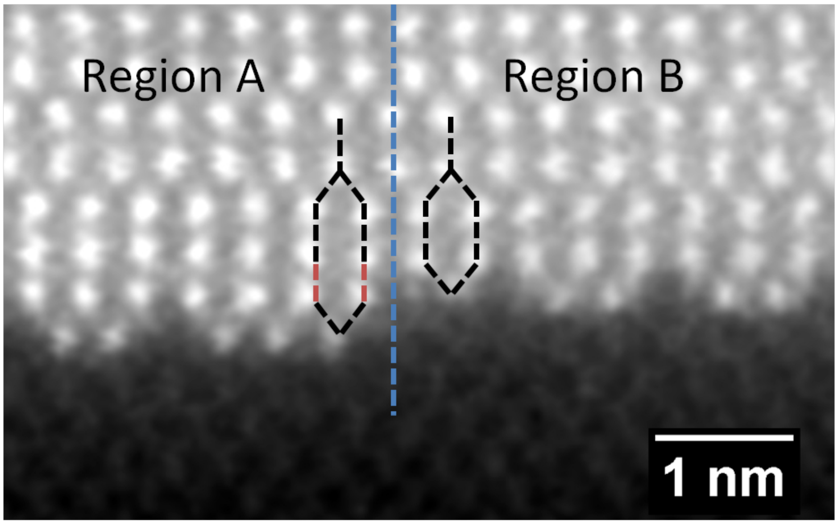

Figure 6.11: A HAADF-STEM image of a tetragonal nanoisland that shows an insertion of an extra plane in order to bring the triangular projection to the interface with the silicon substrate. The tetragonal structure is highlighted by the dashed lines, however in Region A there is an extra plane inserted, highlighted by the red extensions to the dashed lines.

6.2.6 Interface Vacancies

Many of the interfaces we observed showed vacancies. This is attributed to growth of the rare earth silicide into the silicon, which is known to be slow [82], forming a deficiency of erbium at the growth front. As the presence of the extra erbium atom at the interface will result in a distortion of the silicon substrate, it is not unfeasible that this would make it preferential for the erbiums to align into a column rather than randomly position themselves at the interface. An example of this in a nanowire and an island is shown if Fig. 6.12.

6.2.7 Indented Er Columns at the ErSi$_{2-x}$ / Si Interface

Fig. 6.12(B) shows a large islands displaying vacancies along its interface, however upon closer inspection we can observe that some of the Er columns do not sit in the expected positions. Some have been shifted upwards towards the silicide layer. This has been observed in a number of systems as it is also observed in 6.12(A), however it has only been observed at interfaces that have a triangular projection. We observe that the Er plane separation is $\frac{15}{22}\%$ (0.68%) less than in the bulk silicide. This puts the Er column very close to the silicon within the silicide as shown in Fig. 6.13. Here the Er-Si separation between the indented Er and the silicon highlighted in red is 2.2Å where usually in this

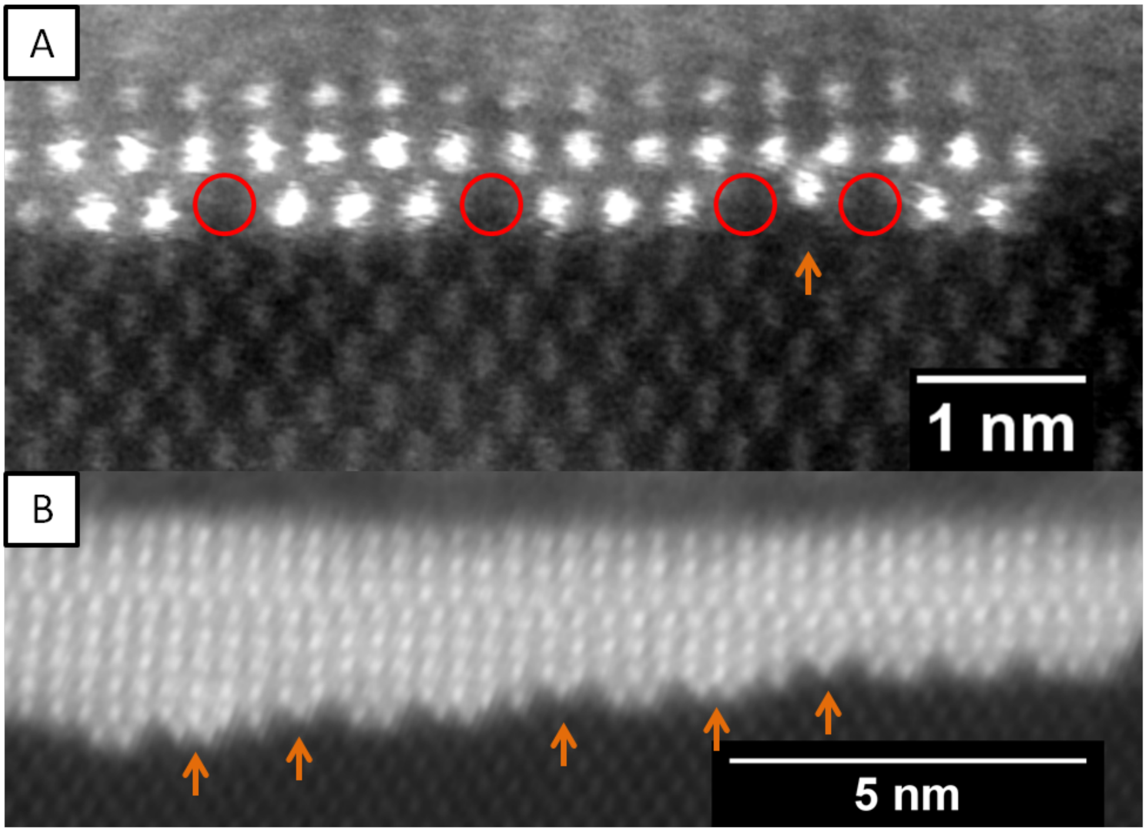

Figure 6.12: (a)An image of a nanowire showing a nanowire displaying interface vacancies, the vacant columns are highlighted by the red circles. (b) A larger island also showing interface vacancies, the arrows highlight Er columns whose positions are shifted up, towards the silicide layer.

interface the shortest Er-Si distance is 2.8Å. When compared to what we would expect the bond length to be from a simple covalent radii estimation of 3Å (198pm + 111pm), we would expect the measured separation of 2.2Å to be highly strained. However it has been observed that the vacancies within the silicon matrix in the RESi$_{2-x}$ is more highly ordered than in bulk, to the point where 2C ordering has been observed. If these silicon vacancies were to order along the highlighted column this would allow the Er atoms to relax into those vacancies reducing the strain of this configuration. These defects have only been observed at interfaces that have the triangular projection.

6.3 Conclusions

The interfaces of the ErSi$_{2-x}$ nanostructures have been found to be extremely varied, showing variation in structure and strain reduction mechanisms. Sometimes even a single nanostructure can exhibit a variety of different interface morphologies. All of the features

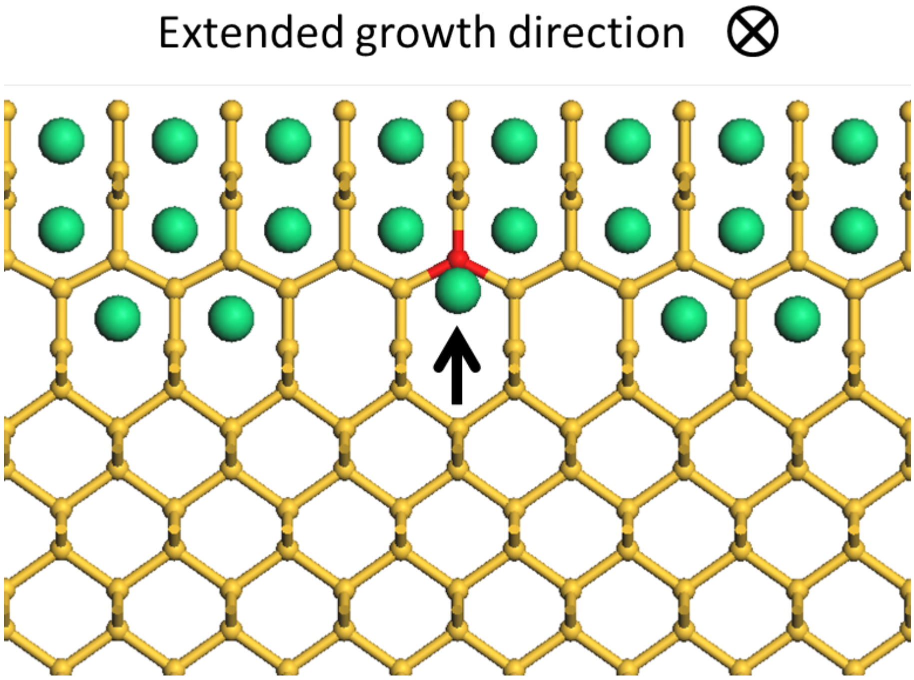

Figure 6.13: The proposed structure for the indented interface. The atom highlighted in red is a Si atom that would be very close to the indented Er atom. The highlighted Si atom is not in plane with the Er atom, it sits between the Er planes formed by the triangular projection.

in the $ErSi_{2-x}$ can be described in terms of the triangular subunit common to the hexagonal and tetragonal $ErSi_{2-x}$ phases with the one exception of the ‘indented interface’ structure. The subunit is able to form triangular and square projections due to the 90° rotation it is capable of, however the indented interface can be understood as a relaxation of an Er column due to ordered silicon vacancies at the interface. If each of the different interface structures presented here exhibit measurable different Schottky barrier characteristics, and the preferred interface type can be controlled through the growth conditions there is huge potential for Schottky barrier engineering in this system.

The various structures detailed include: The growth mechanics of the $ErSi_{2-x}$ nanoislands. A dimming of the upper and lower Er columns within the $ErSi_{2-x}$ nanostructure. The effect of bundling on the nanostructure interface. A previously unobserved single step interface relaxation mechanism. A preference for the nanostructures to form a triangular projection at their interface along the direction of extended growth. Interface vacancies and the previously mentioned indented interface structure.

The nanoislands were found to grow down into the silicon substrate slowly, contrary to previous measurements by examining the interfaces of structures as a function of width and observing if the nanostructure interface extended below the silicon substrate surface.

The dimming of the Er column at the interface and the top of the nanostructure were attributed to incomplete and defected columns which were observed from STM measurements and cross sectional TEM samples perpendicular to the growth direction of the nanowires.

The bundling of nanowires into larger structures cannot be explained in terms of the strained growth model, as in similar strained growth systems, the strain causes the nanostructures to repel one another. However by reexamining this phenomenon in terms of the new orientation relationship found to exist in the ultra-small nanowires, this can be explained as the strain field perpendicular to the nanowires will be small due to the small missmatch between the nanowire and the substrate.

We have observed a new strain reduction mechanism where the ErSi$_{2-x}$ nanoisland drops down a single step on the silicon surface from cross sectional STEM images. This strain reduction mechanism is much rarer than the better studied double step alternative, and was shown to be higher in energy than the double step by Burgers vector analysis.

The observation of the preference for the triangular projection at the interface cannot be easily explained in terms of either the strained growth model or the new orientation relationship. However it can be explained in terms of a strain reduction mechanism that competes with the double stepped interface.

The vacancies that are observed at the ErSi$_{2-x}$ interface are attributed to a deficiency of erbium at a growth front of the nanostructure as it grows down into the substrate. As the movement of erbium atoms has been shown to be very much slower than the movement of silicon atoms [82].

The indented interface as previously mentioned cannot be explained with the simple triangular subunit common to both the hexagonal and tetragonal silicides, as the interfaces generated bring Er atoms unrealistically close to Si atoms. The structure is thought to be the result of a relaxation of the Er column due to an ordered Si vacancy at the ErSi$_{2-x}$ interface.

Chapter 7

Conclusions and Further Work

7.1 Conclusions

We have shown the erbium silicide nanostructures on Si(001) system to be more complex than previously thought. The interfaces of the nanostructures were analysed in Chapter 6 and were shown to exhibit many different morphologies that are not predicted or even explainable in terms of the currently accepted growth model. In chapter 5 we show that the structure of the ultra-small nanowires is hexagonal with its c-axis parallel to the extended growth direction.

Our results suggest that assumptions that result from the stained growth model, namely the orientation relationship, that have been used in all DFT calculations and STM simulations to date is not valid.

7.1.1 Capping

We have shown that titanium or silicon capping does not seem to affect the morphology of ErSi$_{2-x}$ nanostructures, as similar features were observed in titanium capped, silicon capped and non-capped samples. Smaller nanowires appear to be more susceptible to oxidation than larger islands as they were observed to still show an oxide region even when the islands were well protected.

Silicon capping is technically easier to achieve than titanium capping with the equipment that we had available and seems to provide better protection. Silicon capping was also shown to greatly reduce the beam sensitivity of the nanowires allowing repeated scans of the same structure without losing information, where as with titanium capping the nanowire was amorphized from the top down. This indicates that the electron beam was driving a reaction between the nanowire and the oxygen or titanium, rather than simply causing beam knock on damage to the nanowire.

7.1.2 Ultra-Small ErSi$_{2-x}$ Nanowire Structure

We have shown that the preferred ErSi$_{2-x}$ morphology for nanowires less than 5nm in width is hexagonal with the c-axis aligned along the direction of extended growth. On the vicinial Si(001) surface the preferred silicon interface termination for nanowires $\leq$ 5nm in width is ‘a-type’. A possible structure model for the observed morphologies of the nanowires is shown in Fig. 5.8.

We have shown that the accepted growth model fails to explain the structure of the ultra-small ErSi$_{2-x}$ nanowires. The preferred structure of the ErSi$_{2-x}$ is hexagonal with the c-axis aligned along the direction of extended growth with a preference for the final Si dumbbell to be directly underneath the interfacial Er column. The results imply that strain is not the dominant factor in the formation of the ultra-small nanowires. The existence of larger islands on the same sample with the expected orientation shows that as the nanowires evolve into islands, strain becomes the dominant factor and the islands reorganize their structure to compensate for the strain build up. The reason that the unexpected ultra-small ErSi$_{2-x}$ nanowire structure has not been previously observed is attributed to the fact that previous studies have not analysed small enough structures, as the new orientation does not survive when the nanowire size increases.

Our structure model is able to describe some of the periodic features from previous work that have so far been unexplained in terms of the atomic structure and known dimerization mechanisms, and is fully consistent with previous work.

Our results also show that there is a critical width for the unexpected ‘parallel’ structure, as no nanowires of widths $<$15nm were observed with the parallel structure, suggesting that there is a cutoff in the 10-15nm region, which is quite probably due to increasing strain in the nanowire. We have observed nanowires that have defects within their crystal structure hinting at a method for the transformation of one phase into another. Fig. 5.10 shows such a nanowire. This suggests that the transformation occurs from the edge and progresses across the nanowire laterally.

The work of Eames et. al. [16] provides a possible explanation for the observed orientation relationship of the ultra-small nanowires. In their work they found that on the clean dimerized Si(001) surface the ‘tetragonal’ structure was lower in energy than the ‘hexagonal’ structure, regardless of the dimer row direction. However their ‘tetragonal’ structure can be described in terms of a hexagonal structure with its c-axis parallel to the growth direction, which is what we observe as the preferred structure for ultra-small nanowires. This implies that the observed orientation relationship is lower in energy than the accepted strained growth orientation relationship. Eames et. al. note in their paper [16] that the surface reconstruction of the hexagonal nanowire does not form the c(2×2) which is more commonly observed in STM, where their ‘tetragonal’ nanowire does, so they conclude that most nanowires are tetragonally capped. However our results indicate that instead of the surface being tetragonally capped the whole nanowire has the parallel structure. The fact that the ‘parallel’ structure is able to access the c(2×2) surface reconstruction and that the ‘perpendicular’ structure was not able to may indicate that the surface reconstruction may be the reason for the preference for the ‘parallel’ structure.

7.1.3 Interface Structures of ErSi$_{2-x}$ Nanostructures

The interfaces of the ErSi$_{2-x}$ nanostructures have been found to be extremely varied, showing variation in structure and strain reduction mechanisms. Sometimes a even single nanostructure can exhibit a variety of different interface morphologies. All of the features in the ErSi$_{2-x}$ can be described in terms of the triangular subunit common to the hexagonal and tetragonal ErSi$_{2-x}$ phases with the one exception of the ‘indented interface’ structure. The subunit is able to form triangular and square projections due to the 90° rotation it is capable of, however the indented interface can be understood as a relaxation of an Er column due to ordered vacancies at the interface. If each of the different interface structures presented here exhibit measurably different Schottky barrier characteristics, and the preferred interface type can be controlled through the growth conditions, there is huge potential for Schottky barrier engineering in this system.

The various structures detailed include: The growth mechanics of the ErSi$_{2-x}$ nanoislands. A dimming of the top and bottom Er columns within the ErSi$_{2-x}$ nanostructure. The effect of bundling on the nanostructure interface. A previously unobserved single step interface relaxation mechanism. A preference for the nanostructures to form a triangular projection at their interface along the direction of extended growth. Interface vacancies and the previously mentioned indented interface structure.

By examining the interfaces of structures as a function of width and observing if the nanostructure interface extended below the silicon substrate surface, it was found that the nanoislands grow slowly down into the silicon substrate, contrary to previous measurements which suggest that this did not occur [12].

The dimming of the Er column at the interface and the top of the nanostructure in STEM images, was attributed to incomplete and defected columns which were observed from STM measurements and cross sectional TEM samples perpendicular to the growth direction of the nanowires.

The bundling of nanowires into larger structures cannot be explained in terms of the strained growth model, as in similar strained growth systems, the strain causes the nanostructures to repel one another. However by re-examining this phenomenon in terms of the new orientation relationship found to exist in the ultra-small nanowires, this can be explained by the strain field perpendicular to the nanowires being small, due to the small mismatch between the nanowire and the substrate.

We have observed a new strain reduction mechanism where the ErSi_{2-x} nanoisland drops down a single step on the silicon surface from cross sectional STEM images. This strain reduction mechanism is much rarer than the better studied double step alternative, and was shown by Burgers vector analysis to be higher in energy than the double step.

The observation of the preference for the triangular projection at the interface cannot be easily explained in terms of either the strained growth model or the new orientation relationship. However it can be explained in terms of a strain reduction mechanism that competes with the double stepped interface.

The vacancies that are observed at the ErSi_{2-x} interface are attributed to a deficiency of erbium at a growth front of the nanostructure as it grows down into the substrate; as the movement of erbium atoms has been shown to be much slower than the movement of silicon atoms [82].

The indented interface as previously mentioned cannot be explained with the simple triangular subunit common to both the hexagonal and tetragonal silicides, as the interfaces generated bring Er atoms unrealistically close to Si atoms. The structure is thought to be the result of a relaxation of the Er column due to an ordered Si vacancy at the ErSi_{2-x}

interface.

7.2 Further Work

Further work is necessary in order to better characterize the unexpected orientation relationship and its associated properties. Calculations or measurements will be necessary to obtain its electrical characteristics as these are the most important for potential applications.

Work to see if the other rare earth metals behave in a similar way to erbium is also necessary. If it is found that yttrium behaves in a different way to erbium, calculations that substitute yttrium for the lanthanide metal will not be valid, making many of the calculations performed to date invalid.

If it is found that erbium is unique in forming the unexpected orientation relationship during the initial stages of nanowire formation, it would be interesting to investigate whether this structure has any unique properties that could be harnessed as compared to the rest of the rare earth series.

The Schottky barrier of this system would also be a profitable area of continued research as some of the potential applications of this system rely on its unique Schottky barrier characteristics. If the different observed interface structures produce measurably different Schottky barriers and the structure of the interface can be controlled via the growth conditions, there is the possibility of further tuning the Schottky barrier through selection of the desired interface type as well as the rare earth metal.

As the accepted growth model is clearly fails to describe the nucleation and initial growth of erbium silicide nanowires, further calculations should be conducted to determine the driving force behind the growth. Eames et. al. have begun this process by showing that the observed ultra-small nanowire structure is potentially lower in energy than the currently accepted structure.

One area that was not covered in this work was the Si vacancy ordering within the nanowires. If time on a more stable microscope could be procured, trying to directly image the vacancy ordering would allow the structure to be incorporated into simulations and calculations. If it is found that the vacancy structure is dependent on the the growth or size of the nanowire, this would allow another dimension for engineering the nanowire properties for applications.

Appendix A

Appendix - Sample Preparation

A.1 TEM Sample Preparation

Throughout this study the tripod method of cross sectional sample preparation was used, therefore this method will be covered in greatest detail, however other methods are used in the field and shall be discussed briefly

A.1.1 Materials Required

1. Equipment
    (a) SiC p1200 grit self adhesive polishing pads
    (b) Diamond lapping pads 6μ-0.5μ
    (c) Gatan rotary polisher
    (d) Glass plate with metallic backing
    (e) Metallic plate
    (f) Precision circular saw
    (g) Hot plate
    (h) Petri Dishes × 3
    (i) Tripod Polisher with glass stub
    (j) Glass leveling plate
2. Tools and Consumables

(a) Tweezers

(b) Scissors

(c) Vacuum tweezer

(d) TEM sample rings (Mo or Cu)

(e) Epoxy glue (Gatan G1)

(f) Toothpicks

(g) Circular filter paper

(h) Diamond scribe

(i) Membrane boxes

(j) Glass slides

(k) Hand blower

(l) Bulldog clip

(m) Crystal bond wax

(n) Solvents - Acetone, Ethanol, Isopropanol

(o) Microfiber cloth

A.1.2 Tripod Polishing

The tripod polishing technique is suitable for thin films or nanostructures grown on a bulk substrate. However it could be extended to free nanostructures that could be embedded in a glue layer.

This procedure assumes that the sample of interest is a small silicon chip of approximate dimensions 10×3mm with a film grown in a system similar to the one used in this thesis, however extending the procedure to samples of different sizes is straight forward.

1. Cut two (method 1) or one (method 2) silicon chips to the same size as the sample with film by measuring the sample against some scrap silicon and cleaving.
2. Mix some Gatan G1 epoxy and test it prior to use to ensure that the mix is good on a glass slide.

   (a) Method 2: Glue the two pieces scrap Si to the sample, one to act as a mechanical support and the other to act as a covering layer. Glue the scrap silicon so that the shiny side of the scrap silicon faces the shiny side of the sample and rough side to rough side, so that by inspecting the surfaces it will be obvious which glue line has the interface of interest. When curing the epoxy use a bulldog clip to apply constant pressure to the 'sandwich' to press out the glue.
   (b) Method 1: Glue the piece of scarp Si to the sample, to act as a covering layer. Glue the scrap silicon so that the shiny side of the rough side of the scrap silicon faces the shiny side of the sample, so the interface silicon can be identified. When curing the epoxy use a bulldog clip to apply constant pressure to the 'sandwich' to press out the glue.

3. Fix the sample onto a glass slide using the wax and saw the sandwich into smaller pieces using a diamond saw. Producing pieces 2.5-3mm wide by 0.5-1mm in thickness and the three silicon layers in thickness.

4. Before starting to polish the sample level the glass stub by inserting into the tripod, leveling on the glass plate and polishing the glass. If the polishing lines appear everywhere on the glass evenly it is level, if the lines appear at one edge or corner first keep polishing until the whole stub is level.

5. Fix a sample piece to a glass stub from a tripod polisher using crystal bond wax with the covering Si upwards (shiny side down).

6. Level the tripod polisher and begin to polish the covering Si so that it is thin, checking the sample under a stereoscope regularly to ensure that you don't accidentally remove the interface. Be sure to check the leveling of the sample regularly as this step removes a lot of material. When using the diamond lapping pads use a piece of microfiber cloth to catch the material that is removed from the sample.

7. Once the covering silicon is as thin as is reasonable (it does not have to be extremely thin although too thick can be a problem for later steps), remove the glass stub from the tripod and place onto the hotplate to melt the wax

8. Turn the sample so that one of the sawn edges is now facing up, pressing firmly down with a toothpick making a circular motion to ensure that the wax layer underneath the sample is as thin as possible and to remove any bubbles. Once you are happy that the wax layer underneath the sample is thin and there are no bubbles position

the sample close to the edge of the glass stub with the interface of interest next to the glass edge.

9. Polish the sawn face to a mirror shine (0.5 or 1μ), without removing too much material, checking the surface under a stereoscope to check for scratches, cracks or other defects. If such a defect exists go back to a coarser grinding pad and remove the defect, and then re polish to a mirror finish.

10. Once the surface is flat and free of defects reheat the tripod stub to melt the wax. If there is any silicon debris in the wax remove the sample from the stub remove the wax and reapply some fresh wax. Fix the sample to the glass stub with the just polished face down and the interface as close as you can get it to the glass edge without having an ‘overhang’.

11. Coarse polish the sample until it no longer feels thick when running a finger over the top of it, this is usually around 60 μ m or so, remembering to level the tripod regularly, especially when the sample is thin. At this point apply a slight wedge with the tripod and start polishing with less coarse pads, keeping a very close eye on the wax layer around the sample and the interface.

12. Slowly polish the sample keeping an eye on the wax and interface under the stereoscope. If the wax starts to vanish that area getting very thin, if the colour of the silicon starts to change that indicates that that area is getting thin. You are looking to have the silicon around the interface turn an orange-yellow colour.

13. Once the sample is as thin as you want it heat some acetone to 40°s in a petri dish with a filter paper at the bottom. Place the tripod stub into the acetone so that the sample is completely submerged. Then place some tin foil over the petri dish to limit the amount of acetone that evaporates

14. Eventually the sample will fall off the stub, it may require a little ‘help’ if its not coming off after an hour or so, by squirting the sample with some more acetone from the wash bottle. Once it has come off gently lift out the filter paper that should have the sample on it, and transfer to a new petri dish with ethanol and a new filter paper at the bottom. With the sample on the old filter paper run some ethanol down the filter paper to wash the sample into the new petri dish. Repeat the process with IPA. Once the sample has been cleaned in IPA lift out the filter paper and put aside to dry somewhere SAFE.

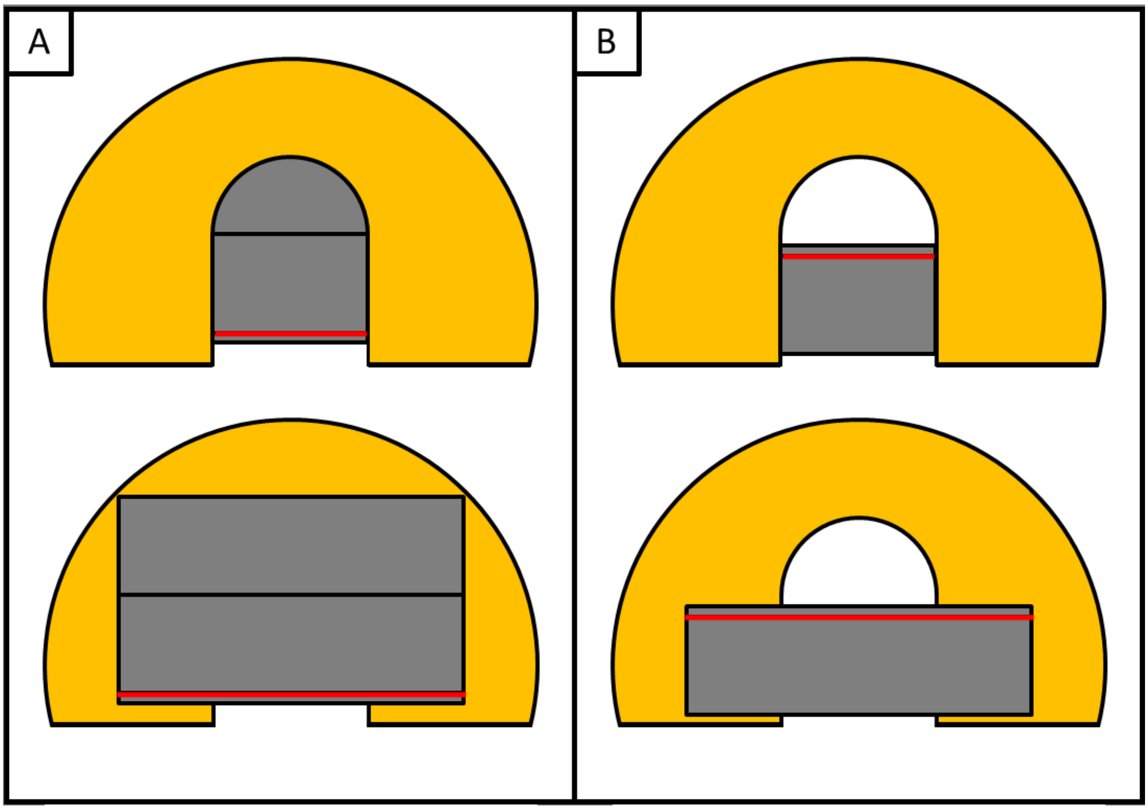

Figure A.1: (A) the arrangement for Method 1 (B) the arrangement for Method 2.

15. Cut a molybdenum TEM sample mounting ring in half. Place onto the now dry filter paper with the sample and carefully coat the rough side in G1 epoxy. Turn the half ring over and wipe off the excess glue by smearing the half ring across the filter paper.
    (a) Method 1: Using the vacuum tweeter place the Mo half ring so that the interface faces away from the ring and is just behind the 'arms' of the half ring so that it does not protrude past them. See Fig A.1(A)
    (b) Method 2: Using the vacuum tweeter place the Mo half ring so that the interface faces towards the center of the ring. See Fig A.1(B)
16. Store the sample in a memberane box between two pieces of microfiber cloth or lens tissue.
17. PIPS to electron transparency as described below
18. Optically bake or plasma clean the sample prior to examination in the microscope as described below

A.1.3 Precision Ion Polishing

The final stage of the sample preparation was precision ion polishing in the Gatan precision ion polishing system (PIPS). The sample was milled at low angle (5°) at 3kV until interference fringes were visible along the interface with a light microscope. This typically took 30-60min. Some samples were milled at lower energies which increased the milling time accordingly, some taking hours to complete.

A.2 TEM Sample Cleaning

The tripod polishing method is known for introducing contamination to the sample system and will often require additional cleaning steps to make the sample suitable for high resolution transmission electron microscopy. The effect of contamination is especially noticeable when in STEM or EELS mode as the focused electron beam has a much higher intensity than the parallel illumination in HRTEM. Two main methods were used to clean the sample prior to examination, Vacuum baking and plasma cleaning. These two techniques will be detailed below.

A.2.1 Vacuum Baking

Baking TEM samples in vacuum is a tried and tested method to reduce contamination, however at York there were no such facilities so I built a system capable of optically baking TEM samples on the JEOL TEM holder at temperatures of 60°C. The system comprised of a 6-way junction which housed an electrical feed through to which a quartz halogen lamp bulb was attached, a pump outlet, a viewing port and an entry dock for the JEOL TEM sample holder. A schematic of the rig is shown in Fig A.2. The two other ports were designed to be used as storage for TEM sample holders, however they were never used.

A.2.2 Plasma Cleaning

Plasma cleaning is another industry standard measure to clean samples prior to examination, and a plasma cleaner was purchased towards the end of my PhD which greatly improved the quality of the data at later stages. The cross sectional sample was loaded

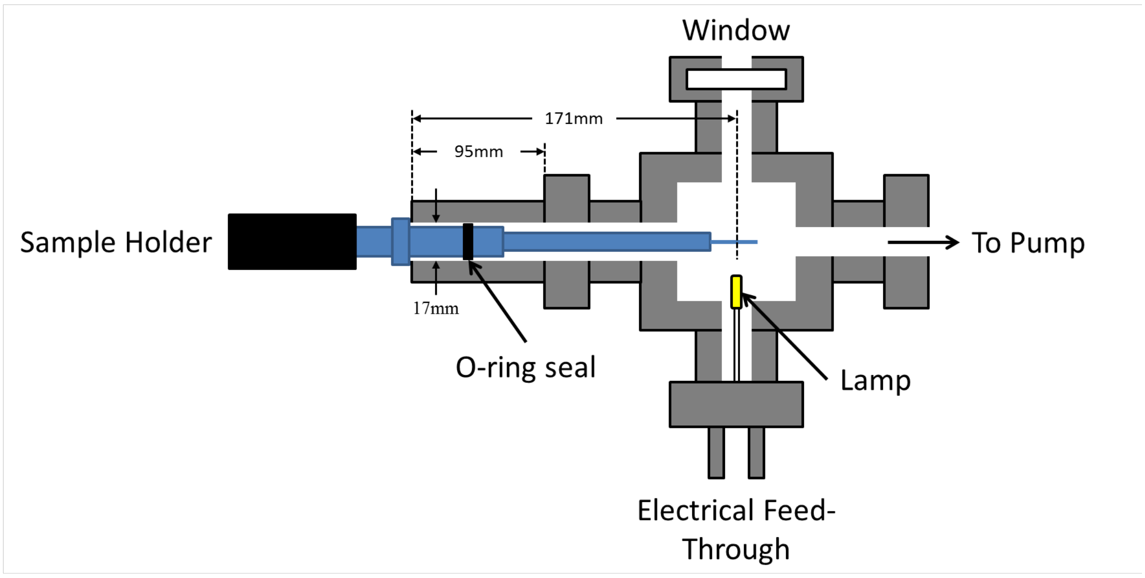

Figure A.2: A schematic of the baking rig that was used to optically bake samples prior to STEM examination.

onto the JEOL sample holder and inserted into the plasma cleaner. The cleaner was run just using air at 15% power for 15 min. This was found to be adequate to limit the contamination while leaving some of the glue layer which is extremely useful for the alignment of the microscope.

Appendix B

Appendix - Theory

Here some of the basic theory that is used in this thesis is described.

B.1 Crystals

B.1.1 Crystal Structure

Charles Kittel defines a perfect crystal as an "infinite repetition of identical groups of atoms". This repeating unit is known as the basis. The points at which the basis is repeated is known as the lattice, which can be defined in three dimensions by three translation vectors $\mathbf{a}_1\mathbf{a}_2\mathbf{a}_3$. The translation vectors move from one point within the crystal **r** to another where the arrangement of atoms is identical **r**'. This can be further generalized so that any integral multiple of the translation vectors takes you to a similar point, i.e.

$$\mathbf{r}' = \mathbf{r} + h\mathbf{a}_1 + k\mathbf{a}_2 + l\mathbf{a}_3 \tag{B.1}$$

Where h, k, l are arbitrary integers. The 'grid' of all **r**' defined by all h, k, l in (B.1) is the lattice. We can define a translation vector **T** that will take us from one lattice point to any other point within the lattice as:

$$\mathbf{T} = h\mathbf{a}_1 + k\mathbf{a}_2 + l\mathbf{a}_3 \tag{B.2}$$

By combining the basis and the lattice it is possible to construct the entire crystal. A primitive lattice has the property that if "any two points from which the atomic arrangement looks the same always satisfy (B.1) with a suitable choice of the integers u_i". A set of primitive translation vectors define the smallest volume that can be used as a building block for the crystal structure, this volume is called the primitive unit cell.

In three dimensions there are 14 spatial lattice types or Bravis lattices, as shown in Table B.1.

System	Number of lattices	Restrictions on conventional cell axes and angles
Triclinic	1	$a_1 \neq a_2 \neq a3$ $\alpha \neq \beta \neq \gamma$
Monoclinic	2	$a_1 \neq a_2 \neq a3$ $\alpha = \gamma = 90° \neq \beta$
Orthorhombic	4	$a_1 \neq a_2 \neq a3$ $\alpha = \beta = \gamma = 90°$
Tetragonal	2	$a_1 = a_2 \neq a3$ $\alpha = \beta = \gamma = 90°$
Cubic	3	$a_1 = a_2 = a3$ $\alpha = \beta = \gamma = 90°$
Trigonal	1	$a_1 = a_2 = a3$ $\alpha = \beta = \gamma =< 120°, \neq 90°$
Hexagonal	1	$a_1 = a_2 \neq a3$ $\alpha \neq \beta \neq \gamma$

Table B.1: The 14 different lattice types in three dimensions [5]

B.1.2 Space Groups

As well as the lattice and basis the last piece of information that is necessary to building a crystal, the space group. The space group combines the Bravis lattice and symmetry operations to be performed on the basis. The symmetry operations take the form of translations, rotations and reflections. There are 230 separate space groups that we can use to describe a crystal. To construct any crystal we need the basis and space group.

The possible symmetry operations that can be performed are:
Reflection about a plane
Rotation about an axis (1,2,3,4 or 6-fold)
Inversion through a point (180°rotation + reflection normal to rotation)
Glide (reflection+translation)
Screw (rotation+translation)
The last three that require a combination of two actions are known as compound opera-

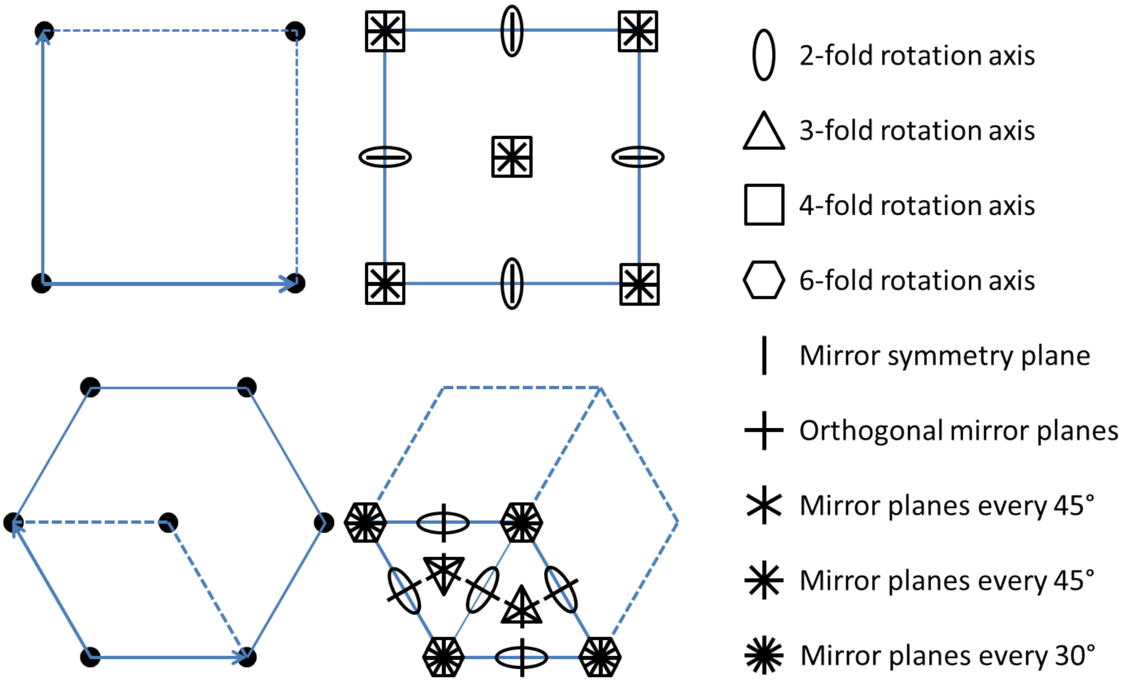

Figure B.1: The various symmetries that apply to a simple square and simple hexagonal lattice

tions.

A graphical representation of the symmetry operations for a simple square and hexagonal lattice are shown in Fig B.1.

B.1.3 Planes

The translation vectors for the unit cell of a crystal are often used to describe different directions or planes. Fig B.2 shows how the directions and planes are referenced using the axes of the unit cell. The unit cell chosen does not have to be the primitive unit cell of the bravis lattice and for hexagonal systems a non primitive cell is often used to better show symmetries of the system. Planes are defined by the direction that is orthogonal to the plane surface. This can be found in square systems by inspecting where the plane cuts the unit cell and taking the reciprocal of the points in terms of the lattice vectors. An example is given in Fig B.2 a plane cuts the unit cell at $1/2, 1/2, 1$. The inverse of this is 2,2,1 so the plane is the (221) plane.

There is a convention regarding the brackets that hold the miller indices;

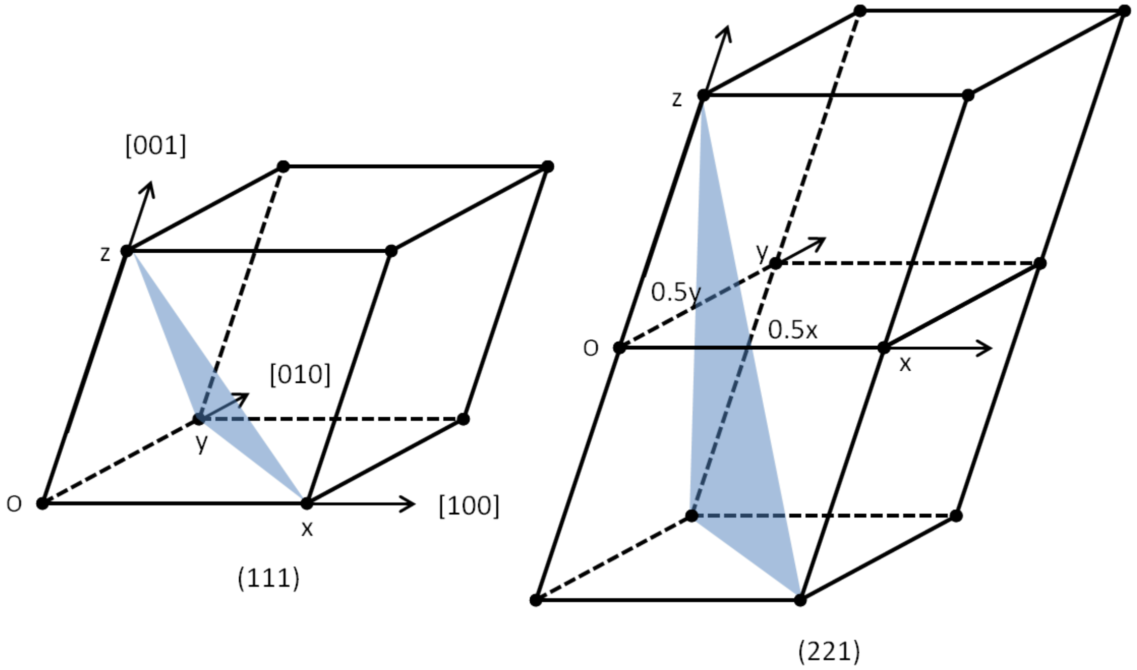

Figure B.2: Left: The plane (111) cutting the unit cell at $x = y = z = 1$. Right: The plane (221) cutting the unit cell at $x = y = 0.5, z = 1$, a second unit cell has been added for ease of viewing.

(abc) - specific plane
{abc} - equivalent planes
[abc] - specific direction
⟨abc⟩ - equivalent directions

In order to describe a face of a cleaved or cut crystal, the plane that lies over the face is used.

B.1.4 Hexagonal Crystals

The indexing of hexagonal systems is not trivial as the Miller index system fails to clearly show the symmetry of the hexagonal system. In hexagonal systems the Bravais-Miller convention is more commonly used, where directions are defined using a four vector notation where there is a third vector in the basal plane of the hexagonal unit cell. The Bravais-Miller directions and planes for a 2D system are shown in Fig B.3. In 3D the c-axis of the hexagonal system is represented as a fourth index, i.e. the direction [0001] is directly along the c-axis. The four figure convention labels the ‘redundant’ index as ‘d’ i.e. [abdc]. The method for calculating the Bravais-Miller indicies is given by the equations (B.3)[151].

To convert between the miller indicies (hkl) and the Bravais-Miller indicies (abdc):

$$\begin{aligned} a =& \frac{1}{3}(2h - k) \\ b =& \frac{1}{3}(2k - l) \\ d =& -(a + b) \\ c =& l \end{aligned} \tag{B.3}$$

B.2 Fourier Transforms

Fourier transforms are an extremely useful and powerful tool that will be used often in the following text. A Fourier transform expresses a function in terms of the component frequencies that compose it. Or more generally it expresses a function in reciprocal units. A function that is defined in terms of time and amplitude e.g. a sine wave will be expressed in terms of inverse time, $\frac{1}{t}$, or frequency. A pure sine wave consists of only one frequency so will have a single point in its Fourier transform that has an amplitude that corresponds to the amplitude of the original sine wave. The transforms are expressed mathematically in 1D as:

$$F(\xi) = \int_{-\infty}^{\infty} f(x) exp(-2\pi i x \xi) dx \tag{B.4}$$

Where ξ is the inverse of x

$$f(x) = \int_{-\infty}^{\infty} F(x) exp(2\pi i x \xi) d\xi \tag{B.5}$$

These transforms can be applied to images to express the image in terms of the frequencies that compose them.

B.2.1 Fourier Transforms in 2D

The fourier transform can be applied in two dimensions, allowing us to decompose an image into the frequencies that make up that image. Any frequencies that are strongly represented in that image will appear as a bright spot in the 2D Fourier transform, in the direction of the periodicity.

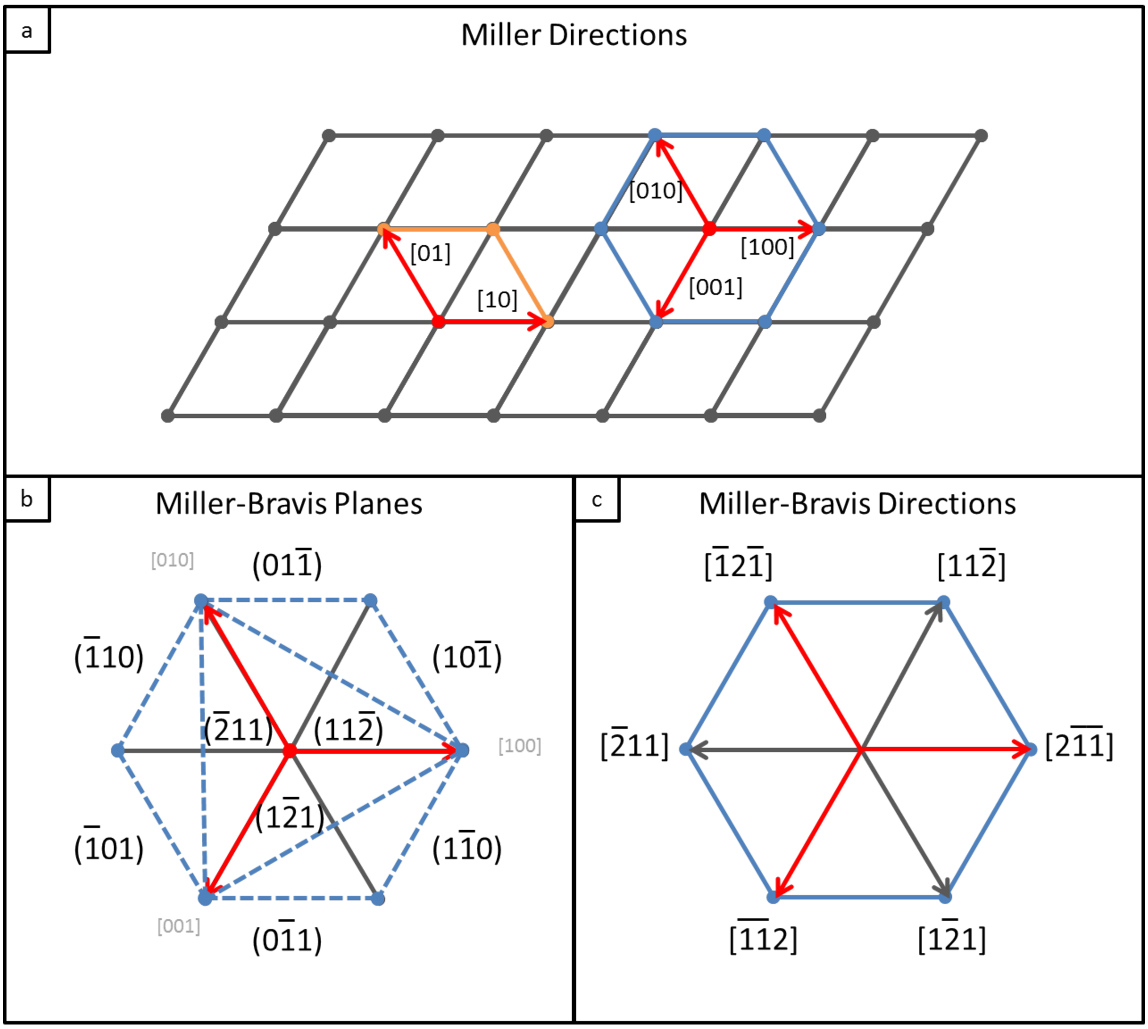

Figure B.3: A graphical representation of the Bravais-Miller system for hexagonal systems. (a) on the left the primitive unit cell for the hexagonal system shown in the orange outline and red translation vectors, on the right the conventional unit cell showing the hexagonal structure more clearly in a blue outline and red translation vectors. The third vector [001] is strictly not necessary however it is useful for symmetry purposes in the hexagonal system. (b) Determining the planes indicated by the dotted lines, using the conventional lattice vectors. (c) The lattice vectors as defined by the Bravais-Miller convention.

We can define a translation vector $\mathbf{G}$ in reciprocal space which is analogous to the translation vector defined for the real lattice in Equation (B.2) using the defined lattice vectors $\mathbf{b}_1, \mathbf{b}_2, \mathbf{b}_3$ that will take us to any reciprocal lattice point

$$\mathbf{G}_{hkl} = h\mathbf{b}_1 + k\mathbf{b}_2 + l\mathbf{b}_3 \tag{B.6}$$

Appendix C

Appendix - Matlab Codes

C.1 Matlab Codes

C.1.1 Imtilt

```
function [ output_image ] = imtilt( input_image,tilt_deg,output_name )
%IMTILT Tilts the input image by the specified amount
%   Used to straighten STEM images that have a constant mechanical drift
%   associated with the image. Reads in the image "input_image" and tilts
%   by the angle "tilt_deg" specified in degrees and then outputs an image
%   as named by "output_name"

imagen = imread(input_image);

%convert the image to double precision
imagen = double(imagen);

%Get the size of the image
[x,y] = size(imagen);
intermediate_image = double(zeros(x,y));

%we assume that the first line is correct
intermediate_image(1,:) = imagen (1,:);

for i = 2 : x
    %extract the row to be shifted
    extracted_row = imagen(i,:);

    %find the required shift
    tilt_rad = tilt_deg * (2*pi/360);
    shift = i*tan(tilt_rad);

    %shift the extracted row by the required amount as set by the angle
    shifted_row = subpxshift(extracted_row,shift);

    %write the shifted row to the output image
```

```
    intermediate_image(i,:) = shifted_row;
end
output_image = uint8(intermediate_image);
imtool(output_image);
imwrite(output_image,output_name);
end
```

C.1.2 Subpxshift

```
function [ shifted_data ] = subpxshift( data,shift )
%UNTITLED2 Summary of this function goes here
%   Detailed explanation goes here
a = round(shift);

%subpx represents the sub pixel shift required.  If the shift rounded up it
%will be a negative value, showing that a backwards step is required
subpx = shift - round(shift);

%Collect the size information about the vector to be shifted)
[x,y] = size(data);

%Create an array to contain the shifted data
shifted_data = zeros(x,y);
%

%Now need to perfrom the shift for the whole data set - again need to split
%into a forwards shift and a backwards shift

if shift>0 %forward shift

    if subpx > 0
        for i = 1:y-(a+1)
        %find dy/dx  (dx=1)
        dy = data(1,i+a+1)-data(1,i+a);

        %New data = value at a + dy/dx*sub_pixel_shift
        shifted_data(1,i) = data(1,i+a) + subpx*dy;
        end

    else %subpx < 0
        for i = 1:y-(a+1)
        %find dy/dx  (dx=1)
        dy = data(1,i+a)-data(1,i+(a-1));

        %New data = value at a + dy/dx*sub_pixel_shift
        shifted_data(1,i) = data(1,i+a) + subpx*dy;
        end

    end

elseif shift<0  %backwards shift
    if subpx < 0
        for i = abs(a)+2:y
        %find dy/dx  (dx=1)
```

```
        dy = data(1,i+(a))-data(1,i+(a-1));

        %New data = value at a + dy/dx*sub_pixel_shift
        shifted_data(1,i) = data(1,i+a) + subpx*dy;
        end

    else %subpx > 0 (i.e. shift = -0.8)
        for i = abs(a)+2:y
        %find dy/dx  (dx=1)
        dy = data(1,i+(a+1))-data(1,i+(a));

        %New data = value at a + dy/dx*sub_pixel_shift
        shifted_data(1,i) = data(1,i+(a)) + subpx*dy;
        end
    end

elseif shift == 0
    shifted_data = data;
end

end
```

C.1.3 Imcorr

```
function [ image2,corr_coeffs,corr2 ] = imcorr(imagen,n )
%IMCORR Summary of this function goes here
%   Detailed explanation goes here
image = imread(imagen);
%image = double(image); %convert the image to double precision

%Get the size of the image
[x,y] = size(image);
image2 = uint8(zeros(x,y));

%we assume that the first line is correct
image2(1,:) = image (1,:);

%create a table of correction coefficients
corr_coeffs = zeros(x,1);
corr2 = zeros(x,2*y-1);

%need to perform the correlation shift for all values of x
for i = 1:(x-1)
    %the -1 is so that we dont try to correlate a line below the image
    %extract line i
    a = image2(i,:);
    %extract the line below
    b = image(i+1,:);
    %perform the correlation getting the shifted line 'b2'
    %and the correlation shift number 's'
    [b2,s,corr] = correlate(a,b,n);
    %write the shifted line 'b2' to image2
    image2(i+1,:) = b2;
    %write each s value to its corresponding location in corr_coeffs
    corr_coeffs(i+1,1) = s;
```

```
    corr2(i,:) = corr;
end
imtool(image2)
imwrite(image2,'output.tif');
end
```

Bibliography

[1] S. P. Luzan, V. E. Listovnichii, Y. I. Buyanov, and P. S. Martsenyuk, “Phase diagram of the binary erbium-silicon system and physical properties of erbium silicides up to 1050 degrees C,” *Journal of Alloys and Compounds*, vol. 239, no. 1, pp. 77–82, 1996.

[2] N. Frangis, “Two-phases epitaxial growth of erbium silicide on Si (100),” *Physica E: Low-dimensional Systems and Nanostructures*, vol. 43, pp. 176–181, Nov. 2010.

[3] K. Maex and M. Van Rossum, *Properties of Metal Silicides*. INSPEC, 1995.

[4] T. Ding, “Rare-Earth Metal Silicide Nanostructures on Si(001) Surface,” *International Journal of Modern Physics B*, vol. 21, no. 11, pp. 1799–1815, 2007.

[5] C. Kittel, *Introduction to Solid State Physics*. Wiley, 8th editio ed., 2005.

[6] Y. Cheng, Z. Gang, L. Dae-Young, L. Hua-Min, L. Young-Dae, Y. W. Jong, P. Young-Jun, and K. Jong-Min, “Self-Assembled Wire Arrays and ITO Contacts for Silicon Nanowire Solar Cell Applications,” *Chinese Physics Letters*, vol. 28, p. 035202, Mar. 2011.

[7] “http://versatile.mdm.imm.cnr.it/,” 2012.

[8] P. Brown, “Antiferromagnetism in Mn5Si3: the magnetic structure of the AF2 phase at 70 K,” *Journal of Physics: Condensed Matter*, vol. 7, pp. 7619–7628, 1995.

[9] A. V. Morozkin, V. K. Portnoy, A. V. Leonov, and I. A. Sviridov, “Crystallographic data of new ternary Sm5Ge4 - type R2Ti3Ge3 compounds (R=Gd-Er),” *Journal of Alloys and Compounds*, vol. 278, pp. L8–L9, 1998.

[10] “http://phycomp.technion.ac.il/˜ira/types.html,” 2012.

[11] “http://cst-www.nrl.navy.mil/lattice/struk.xmol/b27.pos,” 2012.

[12] Y. Chen, D. A. A. Ohlberg, G. Medeiros-Ribeiro, Y. A. Chang, and R. S. Williams, "Self-assembled growth of epitaxial erbium disilicide nanowires on silicon (001)," *Applied Physics Letters*, vol. 76, no. 26, pp. 4004–4006, 2000.

[13] C. G. Zeng, P. R. C. Kent, T. H. Kim, A. P. Li, and H. H. Weitering, "Charge-order fluctuations in one-dimensional silicides," *Nature Materials*, vol. 7, no. 7, pp. 539–542, 2008.

[14] V. Iancu, P. R. C. Kent, C. G. Zeng, and H. H. Weitering, "Structure of YSi2 nanowires from scanning tunneling spectroscopy and first principles," *Applied Physics Letters*, vol. 95, p. 3, Sept. 2009.

[15] A. Shinde, R. Wu, and R. Ragan, "Thermodynamic driving forces governing assembly of disilicide nanowires," *Surface Science*, vol. 604, no. 17-18, pp. 1481–1486, 2010.

[16] C. Eames, M. I. J. Probert, and S. P. Tear, "The structure and growth direction of rare earth silicide nanowires on Si(100)," *Applied Physics Letters*, vol. 96, no. 24, p. 241903, 2010.

[17] G. F. Ye, J. Nogami, and M. A. Crimp, "Dysprosium disilicide nanostructures on silicon(001) studied by scanning tunneling microscopy and transmission electron microscopy," *Thin Solid Films*, vol. 497, no. 1-2, pp. 48–52, 2006.

[18] D. Qiu, P. M. Kelly, and M.-X. Zhang, "The interfacial structure of self-assembled DySi2 nanostructures grown on Si(001)," *Scripta Materialia*, vol. 60, pp. 787–790, May 2009.

[19] B. Z. Liu and J. Nogami, "A scanning tunneling microscopy study of dysprosium silicide nanowire growth on Si(001)," *Journal of Applied Physics*, vol. 93, no. 1, p. 593, 2003.

[20] Y. Zhu, W. Zhou, S. H. Wang, T. Ji, X. Y. Hou, and Q. Cai, "From nanowires to nanoislands: Morphological evolutions of erbium silicide nanostructures formed on the vicinal Si(001) surface," *Journal of Applied Physics*, vol. 100, p. 114312, 2006.

[21] B. C. Harrison, P. Ryan, and J. J. Boland, "STM and DFT study of the Gd wetting layer reconstructions on the Si(001)-2 x 1 surface," *Surface Science*, vol. 582, no. 1-3, pp. 79–89, 2005.

[22] J. Yang, C. Rawn, C.-X. Ji, Y. Chang, Y. Chen, R. Ragan, D. Ohlberg, and R. Williams, “Thermal expansion coefficients of rare earth metal disilicides and their influence on the growth of disilicide nanowires,” *Applied Physics A*, vol. 82, pp. 39–42, Nov. 2005.

[23] H. Rose, “Outline of a spherically corrected semiaplanatic medium-voltage transmission electron-microscope,” *Optik*, vol. 85, no. 1, pp. 19–24, 1990.

[24] FEI, S. Kujawa, B. Freitag, and D. Hubert, “An Aberration Corrected (S)TEM Microscope for Nanoresearch,” 2006.

[25] M. Wanatabe, D. W. Ackland, C. J. Kiely, D. B. Williams, M. Kanno, R. Hynes, and H. Sawada, “The Aberration Corre3cted JEOL JEM-2200FS FEG-STEM/TEM Fitted with an Electron Energy-Filter : Performance Characterization and Selected Applications,” *JEOL news*, vol. 41, no. 1, pp. 2–7, 2006.

[26] Z. He, D. Smith, and P. Bennett, “Faulted surface layers in dysprosium silicide nanowires,” *Physical Review B*, vol. 70, pp. 2–5, Dec. 2004.

[27] Y. Chen, D. Ohlberg, G. Medeiros-Ribeiro, Y. Chang, and R. Williams, “Growth and evolution of epitaxial erbium disilicide nanowires on Si(001),” *Applied Physics A: Materials Science & Processing*, vol. 75, pp. 353–361, Sept. 2002.

[28] B. Z. Liu and J. Nogami, “Growth of parallel rare-earth silicide nanowire arrays on vicinal Si(001),” *Nanotechnology*, vol. 14, no. 8, pp. 873–877, 2003.

[29] M. Wanke, K. Löser, G. Pruskil, D. Vyalikh, S. Molodtsov, S. Danzenbächer, C. Laubschat, and M. Dähne, “Electronic properties of self-assembled rare-earth silicide nanowires on Si(001),” *Physical Review B*, vol. 83, pp. 1–11, May 2011.

[30] J. H. G. Owen, K. Miki, and D. R. Bowler, “Self-assembled nanowires on semiconductor surfaces,” *Journal of Materials Science*, vol. 41, no. 14, pp. 4568–4603, 2006.

[31] C. Preinesberger, S. Vandre, and T. Kalka, “Formation of dysprosium silicide wires on Si (001),” *Journal of Physics D:*, vol. 31, no. 12, pp. L43–L45, 1998.

[32] W. Küchle, M. Dolg, and H. Stoll, “Ab Initio Study of the Lanthanide and Actinide Contraction,” *The Journal of Physical Chemistry A*, vol. 101, pp. 7128–7133, Sept. 1997.

[33] L. Pan, X. Huang, J. Li, Y. Wu, and N. Zheng, “Novel Single- and Double- Layer and Three- Dimensional Structures of Rare-Earth Metal Coordination Polymers :

The Effect of Lanthanide Contraction and Acidity Control in," *Angewandte Chemie (International ed.)*, vol. 39, no. 3, pp. 527–530, 2000.

[34] "http://oxforddictionaries.com/," 2012.

[35] J. Ratajczak, A. Laszcz, A. Czerwinski, J. Katcki, F. Phillipp, P. A. Van Aken, N. Reckinger, and E. Dubois, "Transmission electron microscopy study of erbium silicide formation from Ti/Er stack for Schottky contact applications," *Journal of Microscopy-Oxford*, vol. 237, no. 3, pp. 379–383, 2010.

[36] C. S. Park, B. J. Cho, and D.-l. Kwong, "Thermally Stable Fully Silicided Hf-Silicide Metal-Gate Electrode," *IEEE Electron Device Letters*, vol. 25, no. 6, pp. 372–374, 2004.

[37] M. Bhaskaran, S. Sriram, K. T. Short, D. R. G. Mitchell, a. S. Holland, and G. K. Reeves, "Characterization of C54 titanium silicide thin films by spectroscopy, microscopy and diffraction," *Journal of Physics D: Applied Physics*, vol. 40, pp. 5213–5219, Sept. 2007.

[38] L. J. Chen, "Metal silicides: An integral part of microelectronics," *JOM*, vol. 57, no. 9, p. 24, 2005.

[39] E. J. Tan, K.-l. Pey, N. Singh, G.-q. Lo, D. Z. Chi, Y. K. Chin, K. M. Hoe, G. Cui, and P. S. Lee, "Demonstration of Schottky Barrier NMOS Transistors With Erbium Silicided Source / Drain and Silicon Nanowire Channel," *IEEE Electron Device Letters*, vol. 29, no. 10, pp. 1167–1170, 2008.

[40] D. R. Bowler, "Atomic-scale nanowires: physical and electronic structure," *Journal of Physics: Condensed Matter*, vol. 16, pp. R721–R754, June 2004.

[41] D. Lee and S. Kim, "Formation of hexagonal Gd disilicide nanowires on Si(100)," *Applied Physics Letters*, vol. 82, no. 16, pp. 2619–2621, 2003.

[42] M. Lohmeier, W. Huisman, ter Horst G, P. Zagwijn, E. Vlieg, C. Nicklin, and T. Turner, "Atomic structure and thermal stability of two-dimensional Er silicide on Si(111).," *Physical review. B, Condensed matter*, vol. 54, pp. 2004–2009, July 1996.

[43] J. Y. Duboz, P. a. Badoz, F. A. DAvitaya, and J. a. Chroboczek, "Electronic transport properties of epitaxial erbium silicide/silicon heterostructures," *Applied Physics Letters*, vol. 55, no. 1, p. 84, 1989.

[44] H. Yeom and E. al., “Robust One-Dimensional Metallic Band Structure of Silicide Nanowires,” *Physical Review Letters*, vol. 95, no. 20, p. 205504, 2005.

[45] E. P. Rugeramigabo, C. Tegenkamp, Pfn, Uuml, H. R, T. Inaoka, and T. Nagao, “One-dimensional plasmons in ultrathin metallic silicide wires of finite width,” *Physical Review B*, vol. 81, no. 16, p. 165407, 2010.

[46] C. Piermarocchi, P. Chen, Y. S. Dale, and L. J. Sham, “Theory of fast quantum control of exciton dynamics in semiconductor quantum dots,” *Physical Review B*, vol. 65, no. 7, p. 075307, 2002.

[47] Y. Xia, P. Yang, Y. Sun, Y. Wu, B. Mayers, B. Gates, Y. Yin, F. Kim, and H. Yan, “One-Dimensional Nanostructures: Synthesis, Characterization, and Applications,” *Advanced Materials*, vol. 15, pp. 353–389, Mar. 2003.

[48] H. Li, W. Lu, J. Li, X. Bai, and C. Gu, “Multichannel Ballistic Transport in Multiwall Carbon Nanotubes,” *Physical Review Letters*, vol. 95, pp. 1–4, Aug. 2005.

[49] J.-y. Shiu, C.-w. Kuo, P. Chen, and C.-Y. Mou, “Fabrication of Tunable Superhydrophobic Surfaces by Nanosphere Lithography,” *Chemistry of Materials*, vol. 16, no. 4, pp. 561–564, 2004.

[50] P. Romero-go, J. Toudert, J. R. Sa, A. Borra, A. Barranco, and R. Gonzalez-Elipe, “Tunable Nanostructure and Photoluminescence of Columnar ZnO Films Grown by Plasma Deposition,” *Journal of Physical Chemistry C*, vol. 114, no. 49, pp. 20932–20940, 2010.

[51] J. Cui, “Defect Control and Its Influence on the Exciton Emission of Electrodeposited ZnO Nanorods,” *Journal of Physical Chemistry C*, vol. 112, pp. 10385–10388, July 2008.

[52] Y. Arakawa and H. Sakaki, “Multidimensional quantum well laser and temperature dependence of its threshold current,” *Applied Physics Letters*, vol. 40, no. 11, pp. 939–941, 1982.

[53] J. Faist, F. Capasso, D. L. Sivco, C. Sirtori, A. L. Hutchinson, and A. Y. Cho, “Quantum Cascade Laser,” *Science*, vol. 264, no. 5158, pp. 553–556, 1994.

[54] M. a. Haase, J. Qiu, J. M. DePuydt, and H. Cheng, “Blue-green laser diodes,” *Applied Physics Letters*, vol. 59, no. 11, p. 1272, 1991.

[55] A. D. Yoffe, “Advances in Physics Semiconductor quantum dots and related systems: Electronic, optical, luminescence and related properties of low dimensional systems,” *Advances in Physics*, vol. 50, no. 1, pp. 1–208, 2001.

[56] Y. Lou, M. M. Maye, L. Han, J. Luo, and C.-J. Zhong, “Goldplatinum alloy nanoparticle assembly as catalyst for methanol electrooxidation,” *Chemical Communications*, no. 5, pp. 473–474, 2001.

[57] L. Eastman, R. Stall, D. Woodard, C. Wood, N. Dandekar, M. Shur, and K. Board, “Ballistic Electron Transport in Thin Layers of GaAs,” *IEEE Transactions on Electron Devices*, vol. 27, no. 11, p. 2197, 1980.

[58] O. Kubo, Y. Shingaya, M. Aono, and T. Nakayama, “One-dimensional Schottky contact between ErSi[sub 2] nanowire and Si(001),” *Applied Physics Letters*, vol. 88, no. 23, p. 233117, 2006.

[59] Q. Zhang, M. Tian, Y. Wu, G. Lin, and L. Zhang, “Effect of particle size on the properties of Mg(OH)2-filled rubber composites,” *Journal of Applied Polymer Science*, vol. 94, pp. 2341–2346, Dec. 2004.

[60] C. K. Chan, H. Peng, G. Liu, K. McIlwrath, X. F. Zhang, R. A. Huggins, and Y. Cui, “High-performance lithium battery anodes using silicon nanowires,” *Nature nanotechnology*, vol. 3, pp. 31–5, Jan. 2008.

[61] A. Hand, “High-Index Lenses Push Immersion Beyond 32 nm,” *Semiconductor International*, p. 24, 2006.

[62] R. S. Wagner and W. C. Ellis, “Vapor-Liquid-Solid Mechanism of Single Crystal Growth,” *Applied Physics Letters*, vol. 4, no. 5, pp. 89–90, 1964.

[63] A. L. Schmitt, J. M. Higgins, J. R. Szczech, and S. Jin, “Synthesis and applications of metal silicide nanowires,” *Journal of Materials Chemistry*, vol. 20, no. 2, pp. 223–235, 2010.

[64] P. Krogstrup, J. Yamasaki, C. B. Sorensen, E. Johnson, J. B. Wagner, R. Pennington, M. Aagesen, N. Tanaka, and J. Nygard, “Junctions in Axial III-V Heterostructure Nanowires Obtained via an Interchange of Group III Elements,” *Nano Letters*, vol. 9, no. 11, pp. 3689–3693, 2009.

[65] M. J. Tambe, S. K. Lim, M. J. Smith, L. F. Allard, and S. Gradecak, “Realization of defect-free epitaxial core-shell GaAs/AlGaAs nanowire heterostructures,” *Applied Physics Letters*, vol. 93, no. 15, p. 3, 2008.

[66] R. R. King, D. C. Law, K. M. Edmondson, C. M. Fetzer, G. S. Kinsey, H. Yoon, R. a. Sherif, and N. H. Karam, “40% efficient metamorphic GaInPGaInAsGe multijunction solar cells,” *Applied Physics Letters*, vol. 90, no. 18, p. 183516, 2007.

[67] J. R. Heath, “A Defect-Tolerant Computer Architecture: Opportunities for Nanotechnology,” *Science*, vol. 280, pp. 1716–1721, June 1998.

[68] M. M. Zieglert and M. R. Stan, “Design and Analysis of Crossbar Circuits for Molecular Nanoelectronics,” *IEEE Conference on Nanotechnology (NANO)*, pp. 323–327, 2002.

[69] N. Frangis, G. VanTendeloo, J. VanLanduyt, P. Muret, and T. T. A. Nguyen, “Electron microscopy characterisation of erbium silicide thin films grown on a Si(111) substrate,” *Applied Surface Science*, vol. 102, pp. 163–168, 1996.

[70] N. Frangis, J. VanLanduyt, G. Kaltsas, A. Travlos, and A. G. Nassiopoulos, “Growth of erbium-silicide films on (100) silicon as characterised by electron microscopy and diffraction,” *Journal of Crystal Growth*, vol. 172, no. 1-2, pp. 175–182, 1997.

[71] M. Lohmeier, W. J. Huisman, E. Vlieg, A. Nishiyama, C. L. Nicklin, and T. S. Turner, “Interface structure of Si (111)-(root(3)xroot(3))R30 - ErSi_2-x,” *Condensed Matter Physics*, vol. 345, pp. 247–260, 1996.

[72] W. Tsai, H. Hsu, H. Hsu, and L. Chen, “Vacancy ordering in self-assembled erbium silicide nanowires on atomically clean Si(001),” *Applied Surface Science*, vol. 244, pp. 115–119, May 2005.

[73] J. A. Knapp and S. T. Picraux, “Epitaxial growth of rare-earth silicides on (111),” *Applied Physics Letters*, vol. 48, no. 7, p. 466, 1986.

[74] J. E. Baglin, F. M. DHeurle, and C. S. Petersson, “The formation of silicides from thin films of some rare-earth metals,” *Applied Physics Letters*, vol. 36, no. 7, p. 594, 1980.

[75] R. D. Thompson, "Contact reaction between Si and rare earth metals," *Applied Physics Letters*, vol. 38, no. 7, p. 535, 1981.

[76] S. S. Lau, C. S. Pai, C. S. Wu, T. F. Kuech, and B. X. Liu, "Surface-Morphology of Erbium Silicide," *Applied Physics Letters*, vol. 41, no. 1, pp. 77–80, 1982.

[77] F. Arnaud D'Avitaya, A. Perio, J. C. Oberlin, Y. Campidelli, J. A. Chroboczek, and F. A. Davitaya, "Fabrication and Structure of Epitaxial Er Silicide Films on (111)Si," *Applied Physics Letters*, vol. 54, no. 22, pp. 2198–2200, 1989.

[78] M. P. Siegal, F. H. Kaatz, W. R. Graham, J. J. Santiago, and J. V. A. N. D. E. R. Spiegel, "Formation of Epitaxial Yttrium and Erbium Silicide on Si(111) in Ultra-High Vacuum," *Applied Surface Science*, vol. 38, pp. 162–170, 1989.

[79] R. T. Tung, J. M. Gibson, and J. M. Poate, "Formation of Ultrathin Single-Crystal Silicide Films on Si: Surface and Interfacial Stabilization of Si-NiSi2 Epitaxial Structures," *Physical Review Letters*, vol. 50, no. 6, 1983.

[80] R. T. Tung, J. M. Gibson, and J. M. Poate, "Growth of single crystal epitaxial silicides on silicon by the use of template layers," *Applied Physics Letters*, vol. 42, no. 10, p. 888, 1983.

[81] P. Paki, U. Kafader, P. Wetzel, C. Pirri, J. Peruchetti, D. Bolmont, and G. Gewinner, "Growth of a two-dimensional Er silicide on Si(111)," *Physical Review B*, vol. 45, pp. 8490–8493, Apr. 1992.

[82] J. E. E. Baglin, "Diffusion marker experiments with rare-earth silicides and germanides: Relative mobilities of the two atom species," *Journal of Applied Physics*, vol. 52, no. 4, p. 2841, 1981.

[83] A. Travlos, N. Salamouras, and E. Flouda, "Epitaxial erbium silicide films on (100) silicon: growth, structure and electrical properties," *Applied Surface Science*, vol. 120, no. 3-4, pp. 355–364, 1997.

[84] P. M. Petroff and S. P. DenBarrs, "MBE and MOCVD growth and properties of self-assembling quantum dot arrays in III-V semiconductor structures," *Superlattices and Microstructures*, vol. 15, no. 1, pp. 15–21, 1994.

[85] J. H. V. D. Merwe, "Misfit dislocation generation in epitaxial layers Misfit Dislocation Generation in Epitaxial Layers," *Critical Reviews in Solid State and Materials Sciences*, vol. 17, no. 3, pp. 187–209, 1991.

[86] R. Baptist, S. Ferrer, G. Grenet, and H. Poon, "Surface crystallography of YSi_{2-x} films epitaxially grown on Si(111): An x-ray photoelectron diffraction study," *Physical Review Letters*, vol. 64, pp. 311–314, Jan. 1990.

[87] G. Peng, Y. Feng, a. Huan, M. Bouville, D. Chi, and D. Srolovitz, "Mechanisms of silicon diffusion in erbium silicide," *Physical Review B*, vol. 75, pp. 3–7, Mar. 2007.

[88] L. Stauffer, A. Mharchi, S. Saintenoy, C. Pirri, P. Wetzel, D. Bolmont, and G. Gewinner, "Vacancy-Induced Electronic States in ErSi_1.7(0001)," *Science*, vol. 3697, no. 4, pp. 567–572, 1997.

[89] G. W. Peng, Y. P. Feng, M. Bouville, D. Z. Chi, A. C. H. Huan, and D. J. Srolovitz, "First-principles simulations of Si vacancy diffusion in erbium silicide," *Phys. Rev. B*, vol. 76, p. 33303, July 2007.

[90] H. Shuji and E. al., "Resistance measurements of metallic silicide nanowires on a Si substrate with a four-tip scanning tunneling microscope," *e-Journal of Surface Science and Nanotechnology*, vol. 3, p. 362, 2005.

[91] C. Preinesberger, G. Pruskil, S. K. Becker, M. Dahne, D. V. Vyalikh, S. L. Molodtsov, C. Laubschat, and F. Schiller, "Structure and electronic properties of dysprosium-silicide nanowires on vicinal Si(001)," *Applied Physics Letters*, vol. 87, no. 8, p. 3, 2005.

[92] N. G. Szwacki and I. Y. Boris, "Energy decomposition analysis of metal silicide nanowires from first principles," *Physical Review B*, vol. 75, no. 3, p. 35406, 2007.

[93] T. Ji, J. Song, W. Zhou, and Q. Cai, "Si growth effects on the formation of Er silicide nanostructures," *Applied Surface Science*, vol. 253, pp. 3184–3189, Jan. 2007.

[94] G. Chen, J. Wan, J. S. Yang, X. M. Ding, L. Ye, and X. Wang, "Surface structures of erbium silicide ultra-thin films formed by solid phase epitaxy on Si(100)," *Surface Science*, vol. 513, no. 1, pp. 203–210, 2002.

[95] C. Ohbuchi and J. Nogami, "Holmium growth on Si(001): Surface reconstructions and nanowire formation," *Physical Review B*, vol. 66, no. 16, p. 165323, 2002.

[96] C. L. Ma, S. Picozzi, X. Wang, and Z. Q. Yang, "First principles study of the electronic structures of erbium silicides with non-frozen 4f treatment," *The European Physical Journal B*, vol. 59, pp. 297–303, Nov. 2007.

[97] J. Zhang, M. A. Crimp, Y. Cui, and J. Nogami, "Self-assembled thulium silicide nanostructures on silicon(001) studied by scanning tunneling microscopy and transmission electron microscopy," *Journal of Applied Physics*, vol. 103, no. 6, p. 64308, 2008.

[98] G. F. Ye, M. A. Crimp, and J. Nogami, "Self-assembled Gd silicide nanostructures grown on Si(001)," *Journal of Applied Physics*, vol. 105, no. 10, p. 104304, 2009.

[99] Ye and E. al., "Crystallographic study of self-assembled dysprosium silicide nanostructures on Si(001)," *Physical Review B*, vol. 74, no. 3, p. 303104, 2006.

[100] D. Qiu, M.-X. Zhang, and P. M. Kelly, "Crystallography of self-assembled DySi[sub 2] nanowires on a Si substrate," *Applied Physics Letters*, vol. 94, no. 8, p. 083105, 2009.

[101] D. W. Pashley, M. J. Stowell, M. H. Jacobs, and T. J. Law, "The growth and structure of gold and silver deposits formed by evaporation inside an electron microscope," *Philosophical Magazine*, vol. 10, no. 103, pp. 127–158, 1964.

[102] T. Ide, A. Sakai, and K. Shimizu, "Nanometer-scale imaging of strain in Ge island on Si(001) surface," *Thin Solid Films*, vol. 357, pp. 22–25, Dec. 1999.

[103] J. W. Matthews, "Accommodation of misfit across the interface between single-crystal films of various face-centred cubic metals," *Philosophical Magazine*, vol. 13, no. 126, pp. 1207–1221, 1966.

[104] B. Elman, E. S. Koteles, P. Melman, C. Jagannath, J. Lee, and D. Dugger, "In situ measurements of critical layer thickness and optical studies of InGaAs quantum wells grown on GaAs substrates," *Applied Physics Letters*, vol. 55, no. 16, p. 1659, 1989.

[105] P. W. Voorhees, "The Theory of Ostwald Ripening," *Journal of Statistical Physics*, vol. 38, no. 1/2, pp. 231–252, 1985.

[106] A. Oriani, "Ostwald ripening of precipitates in solid matrices," *Acta Metallurgica*, vol. 12, pp. 1399–1409, 1964.

[107] H. G. Yang and H. C. Zeng, "Preparation of Hollow Anatase TiO 2 Nanospheres via Ostwald Ripening," *Journal of Physical Chemistry. B*, vol. 108, no. 11, pp. 3492–3495, 2004.

[108] J. Yang, Q. Cai, X.-D. Wang, and R. Koch, "Initial stages of erbium disilicide formation on Si()," *Surface Science*, vol. 526, pp. 291–296, Mar. 2003.

[109] Y. Chen, D. A. A. Ohlberg, and R. S. Williams, "Nanowires of four epitaxial hexagonal silicides grown on Si(001)," *Journal of Applied Physics*, vol. 91, no. 5, pp. 3213–3218, 2002.

[110] J. S. Yang, Q. Cai, X. D. Wang, and R. Koch, "Morphological evolution of erbium disilicide nanowires on Si(001)," *Surface and Interface Analysis*, vol. 36, no. 2, pp. 104–108, 2004.

[111] M. Naitoh, H. Shimaya, S. Nishigaki, N. Oishi, and F. Shoji, "Scanning tunneling microscopy observation of bismuth growth on Si(100) surfaces," *Surface Science*, vol. 377-379, pp. 899–903, Apr. 1997.

[112] J. F. Chen, Y. C. Lin, C. H. Chiang, R. C. C. Chen, Y. F. Chen, Y. H. Wu, and L. Chang, "How do InAs quantum dots relax when the InAs growth thickness exceeds the dislocation-induced critical thickness?," *Journal of Applied Physics*, vol. 111, no. 1, p. 013709, 2012.

[113] E. Fitzgerald, "Dislocations in strained-layer epitaxy: theory, experiment, and applications," *Materials science reports*, 1991.

[114] R. E. Perala, M. Kuzmin, P. Laukkanen, M. Ahola-Tuomi, M. P. J. Punkkinen, I. J. Vayrynen, R. Perälä, and I. Väyrynen, "Ytterbium on vicinal Si(100): Growth and properties of the 2D wetting layer and the Yb silicide phase," *Surface Science*, vol. 603, pp. 102–108, Jan. 2009.

[115] A. Ramírez, G. H. Cocoletzi, G. Canto, and N. Takeuchi, "First principles calculations of the adsorption and diffusion of Y on the Si(001)-c(42) surface," *Surface Science*, vol. 603, pp. 3414–3419, Dec. 2009.

[116] R. Ragan, "Ordered arrays of rare-earth silicide nanowires on Si(001)," *Journal of Crystal Growth*, vol. 251, pp. 657–661, Apr. 2003.

[117] B. S. Swartzentruber, N. Kitamura, M. G. Lagally, and M. B. Webb, "Behaviour of steps on Si(001) as a function of vicinality," *Phys. Rev. B*, vol. 47, no. 20, pp. 432–441, 1993.

[118] Z. He, M. Stevens, D. J. Smith, and P. a. Bennett, "Dysprosium silicide nanowires on Si(110)," *Applied Physics Letters*, vol. 83, no. 25, p. 5292, 2003.

[119] Y. Katayama, R. Watanabe, T. Kobayashi, T. Meguro, and X. Zhao, "Structure analysis of self-assembled ErSi 2 nanowires formed on Si (110) substrates," *Electrical Engineering in Japan*, vol. 167, pp. 58–62, May 2009.

[120] I.-H. Hong, Y.-F. Tsai, and T.-M. Chen, "Self-organization of mesoscopically ordered parallel Gd-silicide nanowire arrays on a Si(110)-162 surface: A massively parallel active architecture," *Applied Physics Letters*, vol. 98, no. 19, p. 193118, 2011.

[121] J. L. McChesney and E. al., "Gd disilicide nanowires attached to Si(111) steps," *Nanotechnology*, vol. 13, no. 4, p. 545, 2002.

[122] M. Jaochowski and R. Zdyb, "Gold-induced one-dimensional ordering on vicinal Si (111)," *Vacuum*, vol. 48, no. 96, pp. 273–275, 1997.

[123] M. Wanke, K. Löser, G. Pruskil, and M. Dähne, "Structural and electronic properties of rare earth silicide nanowires on Si(557)," *Physical Review B*, vol. 79, pp. 1–11, Apr. 2009.

[124] K. N. Tu, R. D. Thompson, and B. Y. Tsaur, "Low Schottky-Barrier of Rare-Earth Silicide on n-Si," *Applied Physics Letters*, vol. 38, no. 8, pp. 626–628, 1981.

[125] M. Y. Jang, Y. Y. Kim, J. H. Shin, and S. J. Lee, "Formation of erbium-silicide as source and drain for decanometer-scale Schottky barrier metal-oxide-semiconductor field-effect transistors," *Materials Science and Engineering B-Solid State Materials for Advanced Technology*, vol. 114, pp. 51–55, 2004.

[126] R. T. Tung, "Schottky-Barrier Formation at Single-Crystal Metal-Semiconductor Interfaces," *Physical Review Letters*, vol. 52, no. 6, p. 461, 1984.

[127] M. H. Tuilier, C. Pirri, P. Wetzel, G. Gewinner, J. Y. Veuillen, T. A. N. Tan, and T. T. A. Nguyen, "Atomic-Structure of Epitaxial Er Siliides Grown on Si(111) Studied by Surface Extended X-Ray Absorption Fine-Structure," *Surface Science*, vol. 307, pp. 710–715, 1994.

[128] T. Isogai, H. Tanaka, T. Goto, A. Teramoto, S. Sugawa, and T. Ohmi, "Impact of Tungsten Capping Layer on Yttrium Silicide for Low-Resistance n(+)-Source/Drain Contacts," *Japanese Journal of Applied Physics*, vol. 48, p. 04C046, Apr. 2009.

[129] P. Voyles, "Imaging individual atoms inside crystals with ADF-STEM," *Ultramicroscopy*, vol. 96, pp. 251–273, Sept. 2003.

[130] G. Binnig and H. Rohrer, “Scanning tunneling microscopy,” *Helvetica Physica Acta*, vol. 55, pp. 726–735, 1982.

[131] G. Binnig and H. Rohrer, “Scanning Tunneling Microscopy,” *IBM Journal of Research and Development*, vol. 44, no. 1-2, pp. 279–293, 2000.

[132] G. Binnig, H. Fuchs, C. Gerber, H. Pohrer, E. Stoll, and E. Tosatti, “Energy-Dependent State-Density Corrugation of a Graphite Surface as Seen by Scanning Tunneling Microscopy .,” *Europhysics letters*, vol. 1, no. 1, p. 31, 1986.

[133] M. A. Van Hove, “Surface crystallography with low-energy electron diffraction,” *Proceedings: Mathematical and Physical Sciences*, vol. 442, no. 1914, pp. 61–72, 1993.

[134] O. Scherzer, “Über einige Fehler von Elektronenlinsen,” *Z. Physik*, vol. 101, pp. 593–603, 1936.

[135] Y. Katayama, S. Harako, T. Kobayashi, T. Meguro, S. Komuro, and X. W. Zhao, “Oxidation and photoluminescence of ErSi2 nanowires formed on Si substrates,” *Microelectronic Engineering*, vol. 86, pp. 1155–1158, Apr. 2009.

[136] P. D. Nellist and S. J. Pennycook, “Incoherent imaging using dynamically scattered coherent electrons,” *Ultramicroscopy*, vol. 78, no. 1-4, pp. 111–124, 1999.

[137] P. M. Kelly, A. Jostsons, R. G. Blake, and J. G. Napier, “The determination of foil thickness by scanning transmission electron microscopy,” *Physica Status Solidi (A)*, vol. 31, pp. 771–780, Oct. 1975.

[138] D. Delille, R. Pantel, and E. Van Cappellen, “Crystal thickness and extinction distance determination using energy filtered CBED pattern intensity measurement and dynamical diffraction theory fitting.,” *Ultramicroscopy*, vol. 87, pp. 5–18, Mar. 2001.

[139] K. Z. Botros, “A Method for Determining Foil Thicknesses in TEM by Using Convergent Beam Electron Diffraction Under Weak Beam Conditions,” *Micron*, vol. 26, no. 6, pp. 539–543, 1995.

[140] Q. Liu, “A simple method for determining orientation and misorientation of the cubic crystal specimen,” *Journal of Applied Crystallography*, vol. 27, pp. 755–761, Oct. 1994.

[141] A. V. Crewe, “High-Resolution Scanning Transmission Electron Microscopy,” *Science*, vol. 221, no. 4608, pp. 325–330, 1983.

[142] D. C. Joy and D. M. Maher, “Inner-shell electron spectroscopy for microanalysis.,” *Science*, vol. 206, pp. 162–168, Oct. 1979.

[143] L. A. J. Garvie and P. R. Buseck, “Bonding in silicates: Investigation of the Si L 2,3 edge by parallel electron energy-loss spectroscopy,” *Americal Mineralogist*, vol. 84, pp. 946–964, 1999.

[144] C. C. Ahn, O. L. Krivanek, R. P. Burgner, M. M. Disko, and P. R. Swann, *EELS atlas: A reference guide of electron energy loss spectra covering all stable elements*. Gatan, 1983.

[145] A. Shinde, J. X. Cao, W. J. Ouyang, R. Q. Wu, and R. Ragan, “Determination of preferential rare earth adatom adsorption geometries on Si(001),” *Physics Letters A*, vol. 373, no. 38, pp. 3459–3463, 2009.

[146] H. Yasunaga and A. Natori, “Electromigration on semiconductor surfaces,” *Surface Science Reports*, vol. 15, pp. 205–280, Jan. 1992.

[147] J. Nogami, B. Liu, M. Katkov, C. Ohbuchi, and N. Birge, “Self-assembled rare-earth silicide nanowires on Si(001),” *Physical Review B*, vol. 63, pp. 1–4, May 2001.

[148] M. Kuzmin, “Formation of ytterbium silicide nanowires on Si(0 0 1),” *Applied Surface Science*, vol. 222, pp. 394–398, Jan. 2004.

[149] V. Shchukin and D. Bimberg, “Strain-driven self-organization of nanostructures on semiconductor surfaces,” *Applied Physics A: Materials Science & Processing*, vol. 67, pp. 687–700, Dec. 1998.

[150] J. Tersoff, C. Teichert, and M. Lagally, “Self-organization in growth of quantum dot superlattices.,” *Physical review letters*, vol. 76, pp. 1675–1678, Mar. 1996.

[151] F. C. Frank, “On MillerBravais indices and four-dimensional vectors,” *Acta Crystallographica*, vol. 18, pp. 862–866, May 1965.